Conductivity and Defects in Al-doped $Li_7La_3Zr_2O_{12}$

A solid-state Li-ion conductor

Jonas Kolding

Master Thesis in Materials, Energy and Nanotechnology

60 ECTS credits

Department of Chemistry

Faculty of Mathematics and Natural Sciences

UNIVERSITY OF OSLO

June 2019

Master thesis

UNIVERSITY OF OSLO

Spring 2019

Conductivity and Defects in Al-doped $Li_7La_3Zr_2O_{12}$ – A solid-state Li-ion conductor

A small step towards a solid battery future!

2019

Conductivity and Defects in Al-doped $Li_7La_3Zr_2O_{12}$ – A solid-state Li-ion conductor

Jonas Kolding

http://www.duo.uio.no/

Printed at Reprosentralen, University of Oslo

Abstract

Solid-state batteries are considered to be the next big leap for battery technology. The first step to reach this is to make the transition from the potentially hazardous liquid organic electrolyte of today's batteries to a solid-state electrolyte. A promising candidate for such an electrolyte in Li-ion batteries is the material $Li_7La_3Zr_2O_{12}$, showing high conductivity, 3×10^{-4} S/cm at room temperature. The goal of this project has been to synthesize pellets through various synthesis routes and to investigate the defect chemistry, conductivity and structural composition of these samples.

Samples were synthesized through different solid-state synthesis routes; with and without Al dopant, grinding by hand and by ball milling and with sintering temperatures of 1150°C – 1200°C. Powders were grinded by ball milling giving the densest samples.

XRD was used to investigate the atomic structure of the pellets and determine which of the two phases of LLZO, cubic or tetragonal, had formed, as well as identifying secondary phases. Furthermore, SEM was used to study the microstructure and morphology of both the surface and interior of the samples. Lastly, XRD and SEM were used to look for changes in atomic structure and morphology in the ball milled samples after exposure to moisture.

Impedance spectroscopy was used to investigate the electrical properties of the samples. Through this, conductivity and its dependency on pO_2 and pH_2O, activation energy and the pre-exponential factor was found. The impedance plots were deconvoluted and fitted to equivalent circuits.

Al-doping and ball milling has been shown to increase density and promote the formation of the cubic phase of LLZO, with secondary phases only seen in the samples grinded by hand. Furthermore, samples of LLZO have been observed to reach conductivities and activation energies comparable to literature. The conductivity of the samples shows no pO_2 or pH_2O dependencies, and there are no indications of damages to the samples due to water vapor from the measurements.

$Li_7La_3Zr_2O_{12}$ show promising conductivities, and is a good candidate for a solid-state electrolyte. With literature showing good stability towards Li-metal, high performance all

solid-state batteries can be made using this material. Further work should be conducted, however, to find better synthesis routes, providing more consistent and solid samples.

Acknowledgements

The work for this thesis was carried out at the Electrochemistry research group (formerly known as FASE) at the Department of Chemistry, Faculty of Mathematics and Natural Sciences at the University of Oslo. This was conducted from August of 2017 to June of 2019.

Firstly, I must acknowledge the work and help of those who has made additions to this thesis. Astrid Guérin, who had an internship at the research group in August of 2018, made the sample LAL25, used in this work. Also Lars Henriksen, at the Electrochemistry group, and the program he made, automating the measurements on my last sample. This saved me a lot of time, when time was precious.

My supervisors deserve a lot of credit for helping me through this, especially towards the end. My main supervisor, Truls Norby, and my co-supervisors Sabrina Sartori and Yngve Larring (SINTEF) have helped me throughout, and I should probably have used your expertise even more. I would also give a big thanks to Yang Hu, who has been my buddy here at Electrochemistry, for all the help I have received for everything, from the impedance measurements and SEM pictures to painting with expensive metals.

Furthermore, a big shout-out to those who have made it possible to make it through these 5 year; my friends, for cheering me on, my fellow students at MENA and all the people at the Electrochemistry group, the ultimate Frisbee team of OSI, giving me something to do outside of studies, and an extra big thank you to Anders Brennhagen. Even though we may have spent a lot of time doing and discussing really meaningless things, we have learned a lot from each other and kept the spirit up through all this time.

Finally I would like to thank my family for all the love and support you give, and for helping and motivating me to work hard towards my goals. Lastly, to my dear Gerdi, for all your unconditional support and keeping up me and all my complaining about everything and nothing.

Jonas Kolding
June 7th, 2019
University of Oslo

Abbreviations and Acronyms

BSE	Back scattered electron
c-LLZO	Cubic phase of LLZO
CPE	Constant Phase Element
EV	Electric Vehicle
LIB	Lithium-ion Battery
LLZO	$Li_7La_3Zr_2O_{12}$
RT	Room Temperature
SSB	Solid-State Battery
SE	Secondary Electron
SEI	Solid Electrolyte Interphase
SEM	Scanning Electron Microscope
t-LLZO	Tetragonal phase of LLZO
XRD	X-ray Diffraction

Contents

Abstract VI
Acknowledgements VIII
Abbreviations and Acronyms X
1 Introduction 1
1.1 Background 1
1.2 Batteries 3
1.2.1 Li-ion Conductors 5
1.2.2 Electrolytes 5
1.2.3 Garnets 7
1.3 Goal of the Project 8
2 Theory 9
2.1 Electrical Conductivity 9
2.1.1 Types of Conductivity 10
2.1.2 Activation Energy 11
2.2 Defect Chemistry 12
2.2.1 Kröger-Vink Notation 14
2.2.2 Defects in LLZO 14
2.3 Impedance Spectrsoscopy 15
2.3.1 Impedance from Alternating Current 16
2.3.2 Circuit Elements 17
Constant Phase Element 19
2.3.3 Impedance Sweeps 19
2.3.4 Capacitance 20
2.4 Characterization Techniques 21
2.4.1 XRD 21
2.4.2 SEM 22
3 Literature 24
3.1 Background 24
3.2 Synthesis 25
3.3 Doping 26
3.4 Conductivity Measurements 29

3.5 Defect Chemistry of LLZO 30
3.6 Effects of Moisture 31
4 Experimental 33
4.1 Preparation 33
4.2 Characterization 37
4.2.1 XRD 37
4.2.2 SEM 38
4.3 Impedance Measurements 38
4.3.1 Dry Air Measurements 40
4.3.2 pO_2 Dependency Measurements 43
4.3.3 pH_2O Dependency Measurements 44
4.3.4 Impedance Data 46
4.4 Sources of Error 46
4.4.1 Solartron 1260 47
5 Results 48
5.1 Phase Analysis 48
5.1.1 BAL20 after Measurements 49
5.2 Microstructure and Morphology 50
5.2.1 Density 50
5.2.2 Surfaces 51
5.2.3 Internal Microstructure 53
5.3 Conductivity 56
5.3.1 Impedance Spectroscopy and Capacitances 57
5.3.2 Activation Energy 60
5.3.3 pO_2 Dependency 62
5.3.4 pH_2O Dependency 63
6 Discussion 65
6.1 Comparison of Synthesis Routes 65
6.1.1 Phase Composition 65
6.1.2 Microstructure 66
6.1.3 Activation Energy 68
6.2 Defects of LLZO 69
6.2.1 pO_2 and pH_2O Dependencies 70

6.3 Impedance 71
6.4 Corrosion of Pt-wire 71
6.5 Further Work 72
7 Conclusion 74
List of References 76
Appendix 80
A.1 Impedance Plots 80
A.2 Electrode/Pellet Interface 82
A.3 EDS of BAL20 84
A.4 Early Samples 87

1 Introduction

1.1 Background

Modern society is totally dependent on energy. The world consumes more energy than ever, and the demand will be increasing. The International Energy Outlook from 2018 prospects an increase of energy consumption of 25% from 2017 to 2040. [1]. This energy must be produced somehow, and today, the most used source of energy is fossil fuels. There is a consensus among scientists that climate change is real, and that human activities are the leading cause of it, through releasing and thereby increasing the CO_2 levels in the atmosphere (figure 1.1). We, as an international community, must collaborate to implement various measures to reduce the emissions of greenhouse gases, with the Paris agreement being a good example of things moving in the right direction.

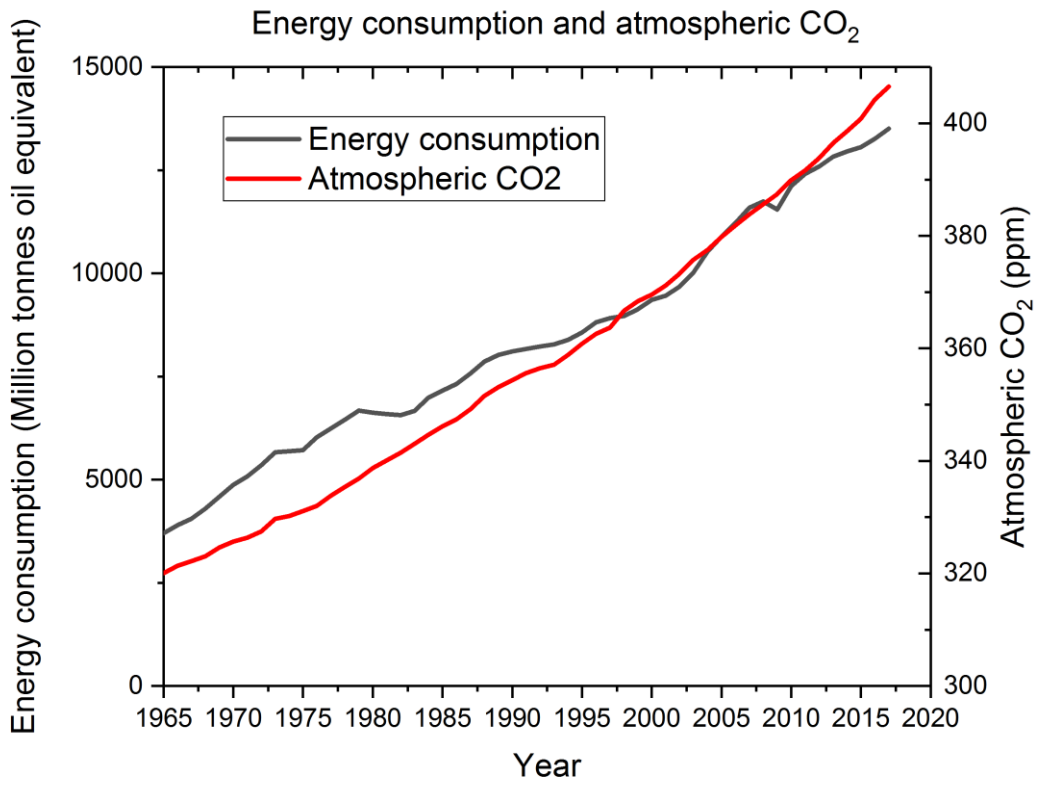

Figure 1.1: The graph shows a clear correlation between our increased energy consumption and the atmospheric CO_2 levels for the last 50 years. Data from [2] and [3].

One part of the problem is emissions coming from the transport sector. So it is inevitably a necessity to restrict the use of fossil fuel within this sector, and implement green, non-emitting propulsion. Hybrid cars, using a combined electric and combustion engine, and EV's are already big business, and ever increasing. Countries are planning for a future without combustion engine cars, like in Norway, where the goal is that all new cars sold should be non-emission cars by 2025. [4] Other big car companies are following, like Volvo who aims for 50% of sales to be fully electric by 2025. [5] At the same time, other companies are rapidly increasing their selection of EV's. However, it is not only the car industry that is electrifying as almost every part of the transportation sector is making the transition to green energy. Yara is creating the world's first autonomous, all-electric container ship, named Yara Birkeland, which will operate between Larvik and Herøya in Norway and is scheduled to be ready in 2020. [6] Both Nikola Motor Company and Tesla are planning to make all-electric semi-trucks, electrifying heavy transport on the roads, both with ranges competing with combustion engine trucks. City buses around the world are now running on electricity, with China leading the way with 99% of all electric buses in the world in use in China today. More countries are following in their path, with Paris, Los Angeles, London and other big cities having committed to buying only all-electric buses by 2025. [7] Not even planes are left un-electrified. Here again, Norway is far ahead, having set the goal of substituting all domestic flights by all-electric planes within 2040. [8] Additionally, companies like Boeing and Airbus are working on this technology, focusing firstly on hybrid planes and reaching for all-electric in the future.

As we can see, the transition to a greener society is slowly but surely on its way. However, with all these technologies relying on electricity to power them, the need for sufficient energy storage is substantial. Modern Li-ion batteries have improved vastly since they were introduced in 1991 and are now the type of battery used in most personal equipment, like PC's and phones and as mentioned above, in cars, buses and even container ships. [9] With all the future plans for use of batteries in transportation and also new smart equipment, the technology needs to be improved even further. The energy density of batteries must be improved, to increase the usage time between each charge, without enlarging the size of the battery itself. At the same time, the life time of the battery needs an improvement. Modern Li-ion batteries degrade over time due to effects like dendrite formation in the electrolyte. These dendrites can also pose a safety hazard as they can cause leakage of the liquid electrolyte which could cause a short circuit, or in a worst case scenario, fires or explosions.

1.2 Batteries

Batteries are today the most effective method we have to store electrical energy. In a battery the energy is stored as chemical energy, which can easily be converted into electrical energy through electrochemical reactions. How these reactions work in a battery is the base for one way of grouping them; as primary or secondary batteries. The primary batteries do not have the possibility to be recharged, so once the reaction is completed, the batteries must be discarded. Still they stand for ~90% of the market. As the technology of secondary batteries has improved and the cost reduced, they are taking more of the market share. These cells are rechargeable, meaning they can be used over again, by connecting them to a charger where the chemical reaction inside is reversed. These kinds of batteries are used in personal electronics, like computers, mobile phones and smart watches, as well as larger things, such as EVs. There are several different types of rechargeable batteries, e.g., lead-acid batteries, nickel-metal hydride batteries and lithium-ion batteries (LIB). However, the LIB is, today, the most energy dense of these technologies. Li-metal batteries could be the next step to increase the capacity of batteries.

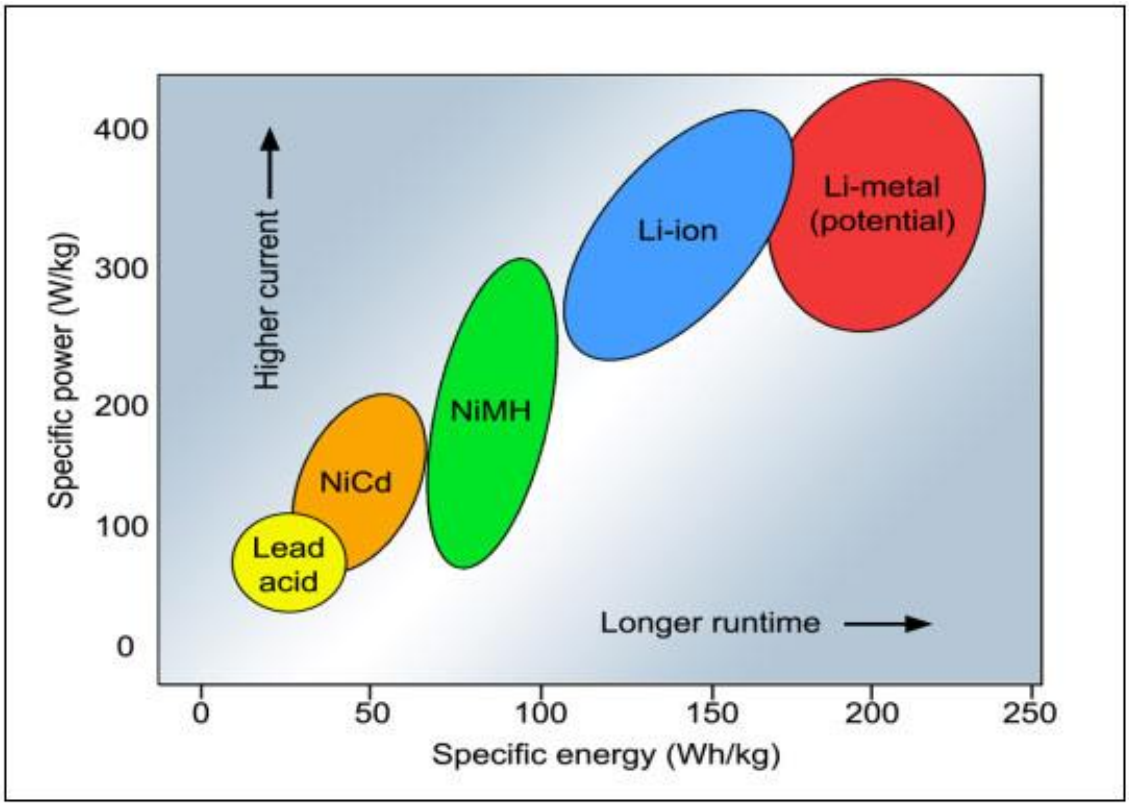

Figure 1.2: Specific power and energy for different types of rechargeable batteries. The Li-ion batteries are currently the best available. Retrieved from [10].

As this thesis is about a material intended as an electrolyte in a LIB, this type of battery will be in focus. A LIB contains three main components: The anode, the cathode and the electrolyte. The Li-ions are intercalated into the anode in the charged state. The ions move to the cathode from the anode through the electrolyte during a discharge of the battery, driven by electrochemical processes. The Li atoms release an electron, before moving through the electrolyte. The electron moves through the circuit to the cathode, where there is a more positive environment, recombining with the positive Li-ions.

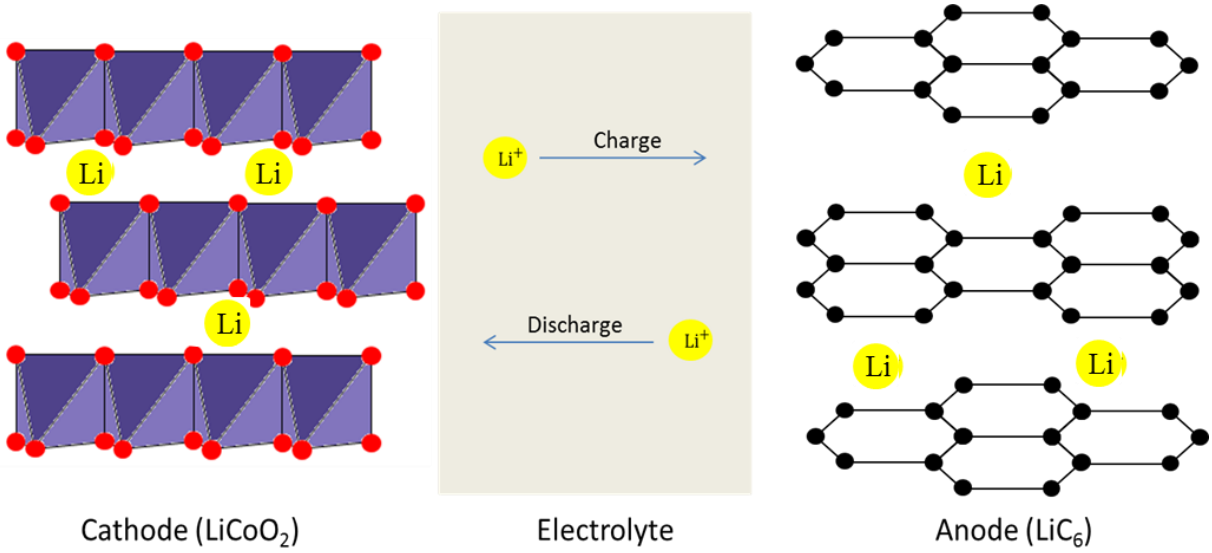

Figure 1.3: Illustration of a Li-ion battery. In the cathode, the red dots are oxygen, while in the anode, the black dots are carbon. Adapted from [11].

The reactions for discharging a Li-ion battery, like the one illustrated above, are:

Anode: $$LiC_6 \rightarrow Li^+ + e^- + C_6 \quad (1)$$

Cathode: $$Li^+ + e^- + 2Li_{0.5}CoO_2 \rightarrow 2LiCoO_2 \quad (2)$$

Total: $$LiC_6 + 2Li_{0.5}CoO_2 \rightarrow 2LiCoO_2 + C_6 \quad (3)$$

There are two types of electrodes, the anode and cathode. For a battery discharging, the conventional current will move from the anode to the cathode and while recharging the battery the flow goes in the opposite way. The conventional current is the flow the positive charge, which makes it the opposite way of the flow of electrons. The polarity of the electrodes will therefore change according to the flow of current. For a battery discharging, the anode is negative and the cathode is positive.

Modern LIBs consist of the materials in the half-reactions mentioned above. Rechargeable Li-ion batteries have an anode of graphite, where the Li-ion is intercalated in between the graphene layers. The cathode consists of CoO_2. This is, like the graphite, a layered material, where Li-ions are intercalated. While $LiCoO_2$ is a material with desirable properties, like stable high capacities and thermal stability, the cobalt industry is causing both environmental and socioeconomic problems in the Democratic Republic of Congo where it is extracted. [12] With problems as striking as these, the battery industry should work on transitioning into other cathode materials for LIBs. Work is being done to improve the cobalt industry; however, new layered materials are being studied and implemented in batteries as well. For instance, MoS_2 is a promising candidate for use as electrode materials in LIBs.

1.2.1 Li-ion Conductors

A Li-ion conductor is a material with a high ionic conductivity towards Li^+-ions. These can be both liquid and solid, with the focus of the scientific community having shifted towards solid ionic conductors, also known as solid electrolytes. The solid electrolytes are used in various applications such as supercapacitors, fuels cells and batteries. As for batteries, the solid electrolyte technology is not yet a viable choice for commercialization, as is discussed further in the next section (1.2.2).

There are big efforts being put into the research of solid electrolytes, mainly focusing on the use in batteries. A big advantage these materials have is their low activation energy, allowing for good conductivity of Li-ions even at room temperature, unlike many solid oxide conductors, which require high temperature. Several different materials already in use as solid Li-ion conductors, such as NASICON (NAtrium Super Ionic CONductor), LISICON (LIthium Super Ionic CONductor) and perovskite- and garnet-type structure materials. All of which have shown conductivities in the order of 10^{-3} S/cm. [13] However, none of these are commercially in use as solid electrolytes in batteries as of yet.

1.2.2 Electrolytes in Batteries

The job of the electrolyte is to move the ions between the electrodes while at the same time prevent electrons from diffusing through. Today the electrolyte of a LIB is an organic ionic liquid. These electrolytes are prone to damage, and could be a potential hazard. In the case of

a damaged battery, leakages in the electrolyte can happen. As a consequence of this, fires and even explosions could occur, as the ionic liquid is flammable and additionally. It is, additionally, toxic, batteries a possible environmental hazard if not handled the right way at disposal. Another issue regarding these liquid electrolytes is the formation of dendrites. At the interface between the anode and the electrolyte, a solid electrolyte interphase (SEI) forms. Through usage of the battery, Li^+-ions start forming dendrites due to potential differences at the surface of the SEI. As a result, the capacity of the battery decrease over time and the dendrites could, in the long run, cause leakages. The SEI, however, is essential for the battery to function properly as it forms as a protective layer between the electrode and the electrolyte, preventing them from reacting further.

One promising solution is the use of ionic liquids instead of the organic liquid used today. Another, which is the one we will be focusing on in this thesis, is the use of solid-state electrolytes. A solid electrolyte will not catch fire as it is not flammable. The battery itself can become thinner, as there will be less excess materials used to produce the battery. This, again, leads to lighter batteries, increasing the overall energy density allowing for more power with smaller batteries. Since everything is now solid, the formation of dendrites is no longer an issue, improving the lifetime of the battery.

There are, however, various issues regarding this technology. The list of suitable materials shrinks considerably as there are very challenging conditions the material must withstand. It must be able to survive the highly oxidizing and reducing conditions at the anode and cathode sites, respectively. Additionally, it must have a good conductance towards Li-ions while having negligible electron conductivity, preventing electrons from going outside the circuit. Another desired ability for the electrolyte material is that it should be stable towards pure Li-metal as an anode. Currently, the biggest challenge for the solid electrolytes is their conductivity. The liquid electrolyte in today's LIBs has a conductivity of about 10^{-2} S/cm at room temperature [14], while we are having problems getting the solid ones to the same values. Promising groups of materials being used in SSBs are approaching the conductivity values of the liquid electrolytes, for instance, some Li-sulfides and Li-garnets are showing conductivities reaching 10^{-2} S/cm [15, 16] and 10^{-3} S/cm [17] at room temperature, respectively. In this work we will investigate the Li-garnet material LLZO.

1.2.3 Garnets

The word garnet means “dark red” and originates from *gernet* in mediaeval Middle English. The mineral, garnet, is, in nature, silica minerals with a general formula of $A_3B_2(SiO_4)_3$, where A and B usually are metals like Mg, Al, Fe or Ca, but it can be found in many different variants.

In the world of battery technology, garnets containing Li have gained increased interest lately, as they are candidates for solid electrolytes. These are based on the garnet structure formula, but without the silicon; $A_3B_2C_3O_{12}$. Here the A-site is 8-coordinated, the B-site is 6-coordinated, sitting in an octahedron of oxygen and the C-site is 4-coordinated, sitting in a tetrahedron of oxygen. Various garnets have been synthesized, e.g. $Li_5La_3M_2O_{12}$ (M=Nb, Ta) and $Li_3Nd_3Te_2O_{12}$, and many others, including doped variant of these, showing a wide range of conductivity values, spanning several orders of magnitude (10^{-8} – 10^{-2} S/cm).

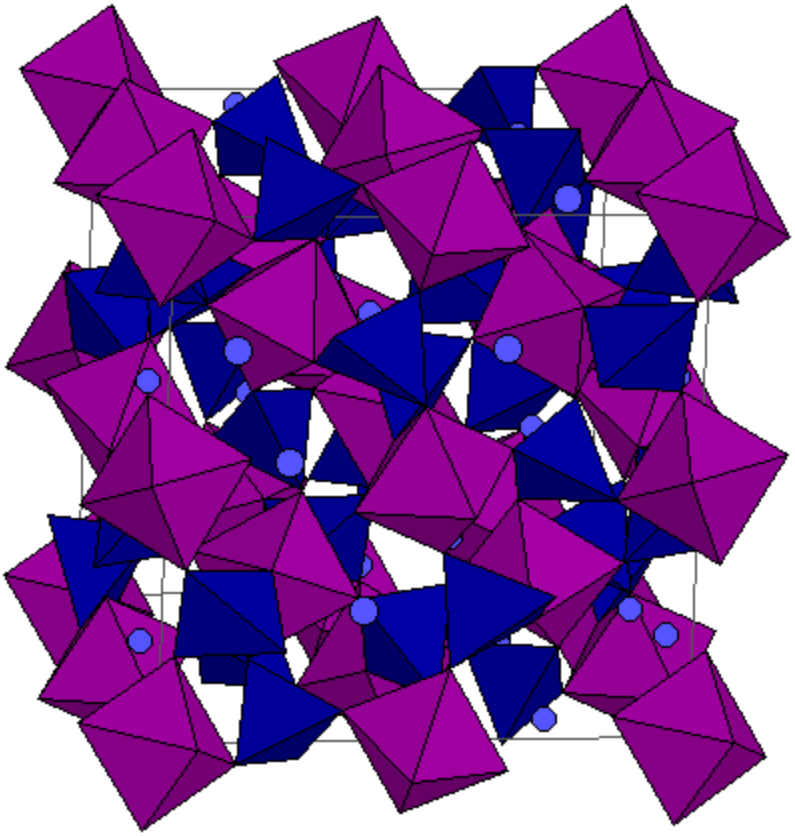

Figure 1.4: An illustration of the garnet structure ($A_3B_2C_3O_{12}$) in the cubic (*Ia-3*) space group. The A site is the light blue dots (8-coordinated), the B-site is the purple octahedrons, the C-site is the dark blue tetrahedrons with the oxygen creating the corners of these polyhedrons. Retrieved from [18].

$Li_7La_3Zr_2O_{12}$ is a relatively newly discovered garnet. Murugan et al. introduced it in 2007, showing its high ionic conductivity, 3.0×10^{-4} S/cm, and stability towards Li-metal. [19] These features make the LLZO a great candidate for a solid-state electrolyte in an SSB. For the LLZO, the Li occupies the C-site, while La and Zr occupies the A and B site, respectively. Looking at the formula unit for LLZO compared to the garnet, it is clear that there is more Li in the structure than there are C-sites. Because of this, the LLZO is a so called stuffed garnet, leading to both a higher Li-ion conductivity and a less stable structure.

1.3 Goal of the Project

The goal of this project is to investigate the Li-garnet LLZO doped by Al as a promising solid-state electrolyte in SSBs. The level of Al-doping will be of interest as it is expected that the conductivity will increase due to this doping. As the material is a candidate for being used as a solid electrolyte in batteries, the main focus will be to investigate the conductivity of the material and how different variables will affect it. Impedance spectroscopy will be conducted at various temperatures to look for changes in charge carriers and contributions from the bulk and grain boundaries. As gas dependencies can reveal a lot about the defect chemistry of a material, the conductivity of LLZO will be measured as a function of both pO_2 and pH_2O. Water is expected to cause alterations to the structure and could weaken the mechanical strength of the pellets. How the pH_2O dependency measurements affect the samples will therefore be of interest. The conductivity will be calculated from the resistance of the samples, measured by impedance spectroscopy. By doing these measurements, the defect chemistry of the material will be investigated in order to provide an in depth understanding of how defects in the structure influences the conductivity.

2 Theory

2.1 Electrical Conductivity

Any species, i, with charge $z_i e$, affected by an electrical field, E, will be subject to a force, F. In a battery charging, this force would pull the negatively and positively charged species to the cathode and anode, respectively. It will be proportional to the charge of the species and the strength of the field, $F = z_i eE$. This will lead to a flux density, j_i, being proportional to the force, the mechanical mobility of the species, B_i[1], and the concentration of the species, c_i:

$$j_i = F c_i B_i \tag{4}$$

By multiplying the flux density by the charge, and introducing the mobility of specie i as $u_i = |z_i| e B_i$ we get a formula for the current density:

$$i_i = z_i e F c_i B_i = F c_i u_i = z_i e E c_i u_i = \sigma_i E \tag{5}$$

Where σ_i is the partial conductivity of specie i:

$$\sigma_i = z_i e c_i u_i \tag{6}$$

The total conductivity in a material is thus the sum of all partial conductivities:

$$\sigma_{tot} = \sum_i \sigma_i \tag{7}$$

These equations are valid for all charged species, including defects in the structure.

In order to understand the conductivity of a species, diffusion theory can be applied to species that follow an activated hopping mechanism. The mobility of the species can be related to the conductivity through the *Nernst-Einstein equation*:

$$D_i = u_i \frac{k_b T}{z_i e} = \sigma_i \frac{k_B T}{c_i z_i^2 e^2} \tag{8}$$

[1] The letter B comes from the German word *Beweglichkeit*, meaning mobility.

Where D_i is the self-diffusion coefficient, k_b is the Boltzmann constant and T is the absolute temperature.

From this it is possible to derive properties such as the activation energy and enthalpy of formation for specie *i*. This is achieved by making an Arrhenius plot of $ln(\sigma_i T)$ vs. $\frac{1}{T}$, from:

$$\sigma_i T = \sigma_0 \cdot \exp(-\frac{\Delta E_a}{k_B T}) \tag{9}$$

Where $E_a = \Delta H_{formation} + \Delta H_{mobility}$ is the activation energy, which is the sum of the enthalpies of formation and mobility of species *i*, though splitting these might not always be possible and σ_0 denotes the pre-exponential factor, which contains entropies of formation and mobility for the charge carrier.

2.1.1 Types of Conductivity

Ionic Conductivity

The ionic conductivity of a material is its ability to conduct ions through its lattice. This is one of the most important abilities of an electrolyte. At the same time they should block other charge carriers moving through. In an aqueous solution, the anions and cations of a compound are moving freely around in the liquid, which is the case for a liquid electrolyte.

In a solid, the ions move through the matter by defects in the lattice of the material. At temperatures above 0K, the lattice will deviate from the perfect form due to entropy, and defects are created. Defects like vacancies and interstitials allow for movement of charged species, such as holes, electrons and ions. For LLZO, Li-vacancies allow for diffusion of Li-ions, leading to Li-ion conductivity in the structure.

In both a solid and a liquid, the movement of ions can be either random or driven. Ions move by random diffusion, or driven towards the electrodes. For an electrolyte in a battery, the ions are moving towards the cathode during discharge, driven by a chemical gradient. Meanwhile they are driven towards the anode by an applied electrical field during charging.

Electronic Conductivity

Electronic conductivity is the movement of electrons in a material and when running through a circuit, powers elements like lightbulbs. Metals are good electronic conductors as the

valence electrons do not bind to single atoms, but instead they are shared among the atoms. Electrolytes should have negligible electronic conductivities as you want the electrons to run through the circuit, powering what the battery is connected to.

Protonic Conductivity

Protonic conductivity is the movement of protons in a material. As a proton is just a positively charged hydrogen ion, they behave in much the same way as ions. The main difference is the size of the ions. This allows for different types of transportation mechanisms, like the *Grotthuß*[2] *mechanism*, also known as proton hopping. This is when a proton diffuses through a collection of H_2O molecules. Additionally, protons can conduct well through water on the surface of materials.

2.1.2 Activation Energy

All chemical reactions have an energy barrier to overcome. In crystalline solids, the mobile species must move through the defective lattice. To start moving, an energy barrier must be overcome. This barrier is described by the activation energy.

To calculate the activation energy of the measured conductivity, the *Arrhenius equation* is used:

$$k = Ae^{-\frac{E_a}{RT}} \tag{10}$$

Where T is the temperature in Kelvin, K, E_a is the activation energy and R is the gas constant. By taking the logarithm of both sides of equation 10, we get:

$$\log(k) = \log(A) - \frac{E_a}{RT} \tag{11}$$

From our measurements, we set k and A as σT and σ_0, respectively. By implementing this we get:

$$\log(\sigma T) = \log(\sigma_0) - \frac{E_a}{RT} \tag{12}$$

This has the form of a linear plot ($x = a + by$), so by plotting $log(\sigma T)$ vs $1000/T$ we can extract the activation energy from the slope:

[2] German way of writing the name. In English, two s'es are used: Grotthuss.

$$E_a = \frac{-2.303R \cdot 1000 \cdot slope}{F} \quad (13)$$

2.2 Defect Chemistry

A solid material can be either amorphous or crystalline. The difference is that an amorphous material lacks the long range periodicity found in a crystalline material, where the atoms sit in specific lattice sites, which repeat indefinitely in all directions of the crystal. However, at all temperatures above 0 K defects will be present in the structure. These defects are essential to the properties of a material, both the mechanical and functional. This is because a perfect crystal has no transport between the lattice sites, as all sites are filled, and no defects are present. With the introduction of defects, atoms, ions electrons are allowed to move in the crystal, opening for diffusion through the structure. So by understanding the defect chemistry of a material it would be possible to predict its properties as well as explaining them.

There are two kinds of defects: structural- and electronic defects. Additionally, there are subclasses of the structural defects. These are classified, depending on their dimensionality.

Zero-dimensional: Imperfections limited to a single lattice site. These defects are called point defects. Point defects can be vacancies, interstitials or substitutionals. In LLZO the expected zero-dimensional defects are mainly Li-vacancies, while oxygen-vacancies and hydroxides are possible, but in a lower concentration.

One-dimensional: Line and plane defects, where the lattice is displaced in one direction. This is called dislocations.

Two-dimensional: Defects affecting the lattice in multiple directions. Often referred to as plane defects. These can be stacking faults, grain boundaries or surfaces. As for LLZO grain boundaries are expected in the samples made.

Three-dimensional: Defects affecting the lattice in all directions. Often called bulk- or volume defects. These can be precipitates, cracks or foreign inclusions. In LLZO these can appear in regions where there is a phase separation between either LLZO and a secondary phase, or between the cubic and the tetragonal phase.

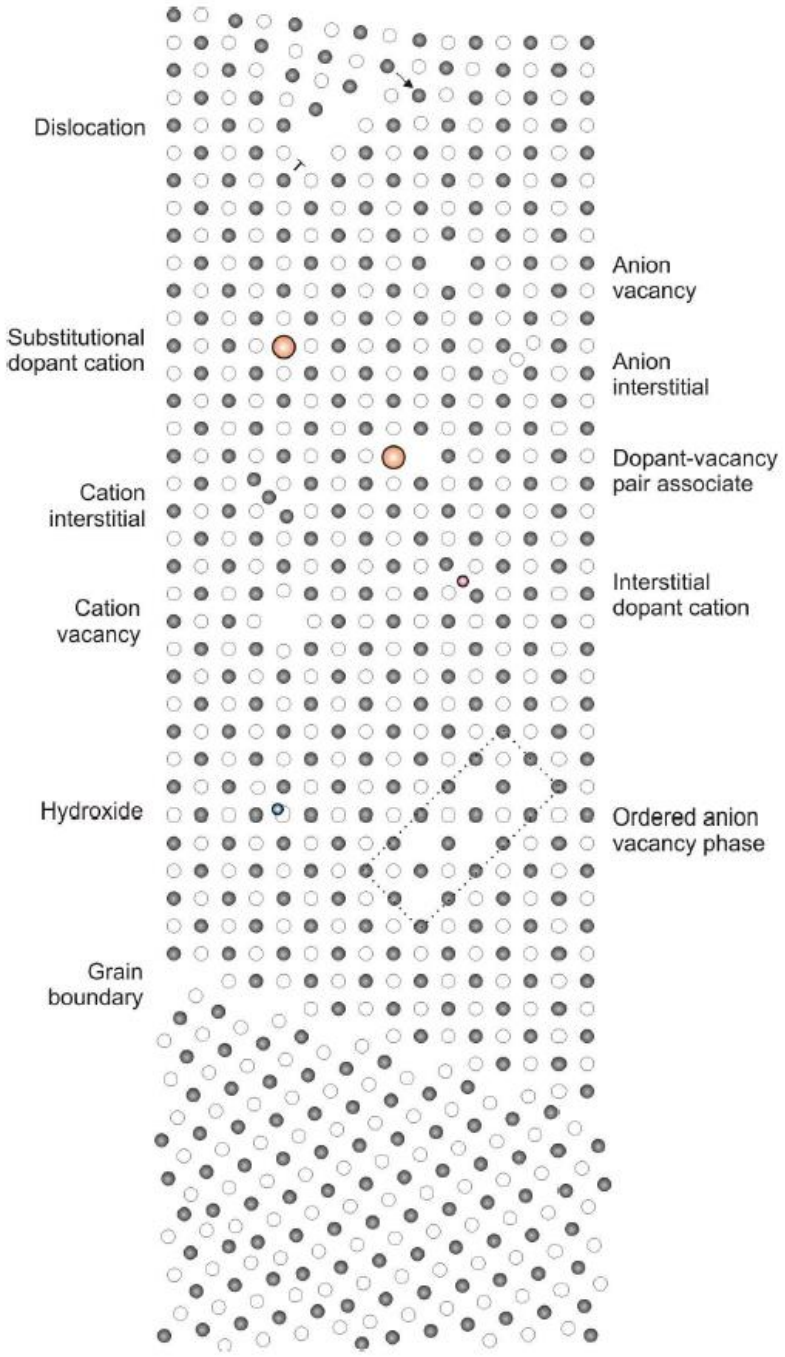

Figure 2.1: Illustration of different types of zero-, one- and two-dimensional defects. Retrieved from [20], page 1-12.

Electronic defects, i.e. free electrons or electron holes are made as a result of internal excitation or through the formation of point defects. They are allowed to move, relatively, freely in the crystal. Should they be constricted to a specific area, they are known as polarons. Electronic defects can also be considered a zero-dimensional defect.

2.2.1 Kröger-Vink Notation

To write defect-chemical reactions for point defects, the *Kröger-Vink notation* is being used. It was developed by F. A. Kröger and H. J. Vink in 1956. [21] It describes what point defect is at which atomic lattice position with what effective charge. The notation is M_S^C, where M is the species, usually atoms (noted with their chemical symbol) or vacancies (v). S is the lattice site the defect occupies, which is interstitials (i) or atoms. And lastly C is the effective charge of the defect, meaning the charge of the new species relative to the charge of the species meant to occupy the site. The charge is noted by "x" for a neutral defect, "•" for a defect with a positive effective charge and "/" for one with a negative effective charge. Should the defect be divalent, relative to the site it occupies, it is noted by two symbols for the charge and so on. An example is a lithium vacancy, which will be denoted: $v_{Li}^{\bullet}$.

An alternative method of using the Kröger-Vink notation has been suggested by Norby. [22] This notation method is used for inherently defective sublattices. As some ionic compounds are good conductors even in nominally undoped form, their conductivity is driven by intrinsic thermal disorder. This can make it hard to write proper defect chemical formulas for these materials. The notation suggested by Norby introduces the use of a partially occupied site as the perfect site. An example for LLZO is suggested in section 6.2.

2.2.2 Defects in LLZO

LLZO is a solid, crystalline material. Its structure is either cubic or tetragonal, but here there cubic phase is of interest, and only zero dimensional defects are considered.

The defect chemistry of LLZO is poorly studied in literature, as most work focus on synthesis routes and conductivity. Still, understanding the defects in the material can help understanding the conductivity and other properties. The Li-ion transport in the LLZO is determined by diffusion of Li-ions in the structure through the Li-sites. For the Li^+-ions to move, there must be vacant Li-sites. These Li-vacancies also help stabilize the cubic phase of LLZO, [23] as discussed in section 3.3. By doping the material, it is possible to force the formation of Li-vacancies.

To stabilize the cubic phase of LLZO at lower temperatures, the material may be doped. As discussed in section 3.3, many different elements have been used for doping this material.

However, in this work, Al is used. The Al^{3+} substitutes the Li^{+}, creating two vacancies. Using the Kröger-Vink notation, the defect reaction becomes:

$$6Li_{Li}^{x} + Al_2O_3(s) = 2Al_{Li}^{\bullet\bullet} + 4v_{Li}^{/} + 3Li_2O(g) \quad (14)$$

Other vacancies that could be expected in LLZO are protons and electrons. As the pH_2O dependency of the conductivity will be investigated, the material will be subject to water vapor. As a result of this, protons can diffuse into the material and react with vacant oxygen sites, forming $OH_O^{\bullet}$ defects through the following reaction:

$$H_2O(g) + v_O^{\bullet\bullet} + O_O^X = 2OH_O^{\bullet} \quad (15)$$

As for electrons, they can form as intrinsic defects during the pO_2 dependency measurements. When the pO_2 increase, the concentration of electrons is expected to decrease as oxygen vacancies disappear. As the concentration of e^- decreases, the concentration of electron holes increase. In a situation near stoichiometric composition, which is the case for LLZO, the concentration of these intrinsic defects is independent of other defects, and only compensates each other, and would therefore have a pO_2 dependency of -¼ for e^- and ¼ for h^+.

2.3 Impedance Spectroscopy

This section is based on [24] and [25].

Impedance spectroscopy is a measurement technique for studying electrical properties in ceramic materials. The technique involves subjecting the sample to an externally applied alternating voltage. This allows us to investigate the physical processes that happen as the system reacts to the applied current, such as mass transport, diffusion and conductivity.

The current will also polarize the transport of the charge carriers of the sample at different frequencies, making it possible to separate where in the sample they move, in the plots. The parts expected to be seen are the bulk at high frequencies, grain boundaries at intermediate frequencies and the electrode at low frequencies. The measurements are conducted at different temperatures. By investigating how the resistances of the samples change with the temperature, it is possible to determine how much energy is needed for the reaction to happen. We call this energy the *activation energy*, which was discussed in section 2.1.2.

2.3.1 Impedance from Alternating Current

For an electrical oscillating voltage (AC), the voltage and the current can be described by sinusoidal functions. The voltage is given as:

$$U = U_0 \sin(\omega t) \tag{16}$$

And has the unit Volt, V. Where U_0 is the amplitude of the voltage and ω is the angular frequency, related to the frequency of the AC voltage through $\omega = 2\pi f$. The phase angle is given as the product ωt. The expression for the current looks fairly similar:

$$I = I_0 \sin(\omega t + \theta) \tag{17}$$

Where I_0 is the amplitude of the current and I having the unit Ampere, A. Just like internal effects, such as induction and capacitances, affect the applied AC voltage, the voltage and the current are out of phase. This phase offset is given as θ.

By controlling the voltage and current, it is possible to measure the impedance of a sample. The impedance can be split into two components, the resistance and the reactance. The resistance, R, is the real part of the impedance, and is in phase with the current. The reactance, X, is the imaginary part, and is 90° out of phase relative to the current. What we call impedance, Z, is the general term resistance, containing both components. In the complex plane, it is represented by

$$Z = Z_{re} + Z_{im} = R + iX \tag{18}$$

Where Z_{re} and Z_{im} are the real and imaginary parts, respectively. The unit of the impedance is Ohm, Ω.

Just like the inverse of the resistivity is conductivity, the inverse of impedance is admittance, Y. The admittance has, just like the impedance, a real and an imaginary part

$$Y = \frac{1}{Z} = G + iB \tag{19}$$

Where G is the real part, called conductance, and B is the imaginary part, called suseptance. The admittance has the unit Siemens, S.

2.3.2 Circuit Elements

There are two types of circuit elements, active and passive. In the deconvolution of the impedance data only passive elements are being used. The passive circuit elements are parts of the circuit that does not generate current or potential. The three main passive elements are the resistor (figure 2.2), capacitor (figure 2.3) and inductor (figure 2.4):

Resistor

Figure 2.2: The symbol of a resistor in a circuit.

The resistor reduces the current flow in electrical circuits. Assuming the resistor is ideal, meaning the current and voltage applied is in phase, the resistance is given by *Ohm's law*;

$$R = \frac{U(t)}{I(t)} \tag{20}$$

And has the unit Ohm, Ω. As the ideal resistor has a resistance independent of ω, it only contributes to the real part of the impedance:

$$Z_{Res} = R = \frac{U}{I} \tag{21}$$

Capacitor

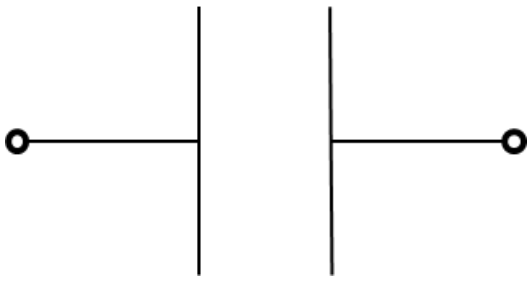

Figure 2.3: The symbol of a capacitor in a circuit.

The capacitor is an element that looks like its symbol (__b). It is an ideal insulator packed between two parallel plate conductors. As the plates are subjected to a current, a net charge,

Q, is produced at the two plates. This causes a voltage, *U*, in the dielectric. The capacitance, *C*, of the capacitor is then defined as the ratio between the charge and the voltage and has the unit Farad, F:

$$C = \frac{Q}{U} \tag{22}$$

The insulator is usually a dielectric material, such as glass, ceramics or oxide layers, which is polarized by applied electric fields. The use of the dielectrics increases the capacitors charge capacity. When this dielectric is polarized it counteracts the applied field from the plate conductors, reducing the voltage. This leads to the general term for the capacitance,

$$C = \epsilon_0 \epsilon_r \frac{\mathrm{A}}{\mathrm{d}} \tag{23}$$

Where ϵ_0 and ϵ_r are the vacuum permittivity and relative permittivity, respectively, A is the area of the plate conductor and d is the distance between them. As the capacitance has a 90° offset to the voltage, it only contributes to the imaginary part of the impedance:

$$Z_{Cap} = \frac{1}{i\omega C} \tag{24}$$

Inductor

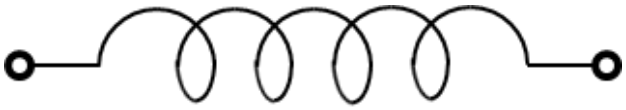

Figure 2.4: The symbol of an inductor in a circuit.

Contrary to the capacitor, which is a perfect insulator, the inductor is a perfect conductor. As current runs through, it produces a magnetic field, according to *Faraday's law* of induction. The magnetic field created applies an AC current back on the conductor, leading to an inductance, *L*, with unit Henry, H. According to *Lenz's law*, this current then has a phase offset of 90° towards the voltage, causing the inductor to only affect the imaginary part of the impedance:

$$Z_{Ind} = i\omega L \tag{25}$$

Constant Phase Element

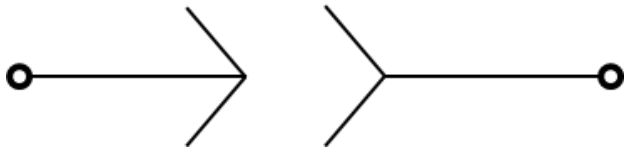

Figure 2.5: The symbol of a CPE in a circuit.

The Constant Phase Element (CPE) is a more complex variant of the capacitor. Measured semicircles have a tendency to become depressed. The reason for this can be grain geometry and orientation relative to the applied field. To make an equivalent circuit fit the depressed semicircle, a CPE is used. The impedance of this element is:

$$Z_{CPE} = \frac{1}{Y_0(i\omega)^n} \tag{26}$$

Where n is the exponent and Y_0 is the admittance constant of a CPE. n has a value between 0 and 1. For n=1, Y_0 becomes the capacitance, and the element becomes a capacitor. While for n<1, it is a CPE (n is determined by the fitting software). For n=0, the impedance of the CPE becomes that of an ideal resistor ($Z = \frac{1}{Y_0}$). This gives the CPE an effective capacitance of

$$C_{eff} = (Y_0 R_s^{-1})^{\frac{1}{n}} \tag{27}$$

Where R_s is the solution resistance estimated value for the capacitance of the CPE, R is the resistance of the resistor in parallel with the CPE, and n is the CPE exponent. [26]

2.3.3 Impedance Sweeps

An impedance sweep is a measure of the complex values of the impedance over a large frequency range, with the instrument used in this work covering a range of 32 MHz to 10 µHz. The real and imaginary parts measured are plotted against each other, with the real values (Z') on the x-axis and the imaginary values (Z'') on the y-axis. This creates a so called *Nyquist plot*, as seen in figure 2.6. Here, several semicircles can be observed, all corresponding to different components of the circuit. By fitting these semicircles to a model of equivalent circuit elements representing reactions, dipole movements and transport in material bulk, grain boundaries or electrode interfaces, it is possible to determine which part contributes to which semicircle. This is due to the fact that the capacitance is affected by the

frequency, through equation 24, as it is related to capacitive reactance. Because of this, a given part of the material (e.g. the bulk) only contributes to the plot in a frequency window. Outside of this window, the contribution is negligible. Using the equivalent circuit, it is possible to assign separate parts of the frequency dispersion to various physical processes in the material. The impedance of these processes can then be used to calculate the ionic or electronic conductivity etc., depending on which part of the impedance is being used.

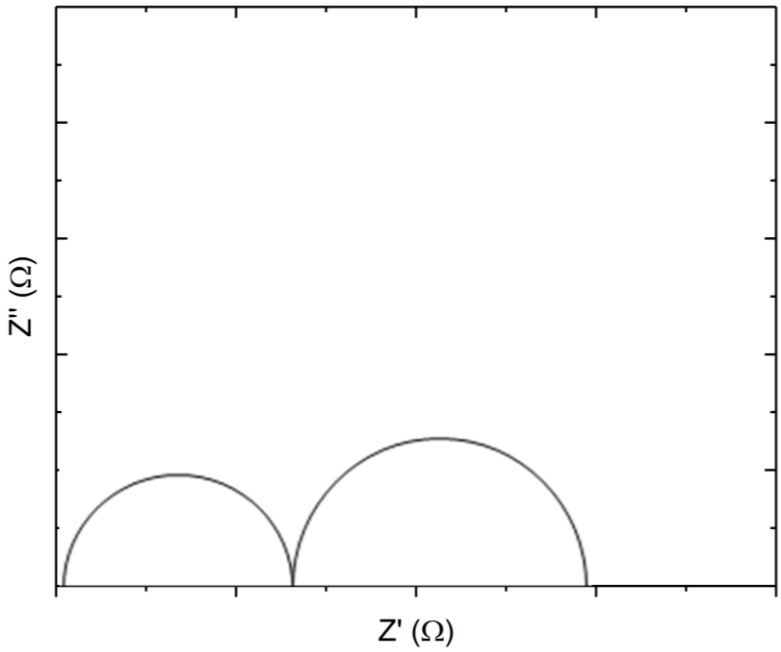

Figure 2.6: Example of a Nyquist plot with two semicircles.

This example provides two perfect semicircles, but the world is not perfect. When a semicircle becomes depressed, the effective capacitance can be found using equation 27.

2.3.4 Capacitance

Capacitance is the ratio between the electric potential and charge in a system, and is calculated by the capacitor circuit element (see section 2.3.2). The value of the capacitance at a given frequency can be found rewriting equation 24:

$$C = \frac{1}{i\omega Z_{Cap}} = \frac{1}{i2\pi f \cdot Z_{Cap}} \tag{28}$$

Here ω is written as $2\pi f$, where f is the frequency of the current. Thus the capacitance is inversely proportional to the frequency, meaning a high frequency gives a low capacitance,

and vice versa. This can be used to determine what part of the sample that generated it. The time dependency of the capacitance is what causes the different parts of a sample to have different responses to the frequency of the applied AC voltage and thus the change in capacitance:

$$\tau = RC = \frac{R}{2\pi f \mathrm{X_C}} \tag{29}$$

Here X_C is the capacitive reactance.

A fast change process leads to a low capacitance and vice versa. The bulk is known to have a low capacitance and is seen in the high frequency part of the spectrum. The reason for this is that the process, for example the flipping of a dipole, is fast, leading to a low capacitance. In the grain boundary, the charging of a space charge region takes more time than the flipping of the dipole in the bulk. Thus, causing a higher capacitance and finding the grain boundary at lower frequencies. Furthermore, the adsorption on a surface is a slow reaction, leading the electrode to have the highest capacitance (of the three regions mentioned).

2.4 Characterization Techniques

2.4.1 XRD

X-ray diffraction is an effective way of characterizing crystalline materials, and does not provide any information for amorphous materials. This technique is used to investigate the crystal structure of a material. A monochromatic x-ray beam is sent onto the sample from a source. This beam is then diffracted by the repeating lattice in the crystal, according to *Bragg's law*:

$$2dsin\theta = n\lambda \tag{30}$$

Where d is the distance between the imaginary atomic planes, θ is the angle between the atomic planes and the x-ray beam, n is a positive integer and λ is the wavelength of the monochromatic beam. As the beam leaves the material, there is a phase shift in the x-rays, as illustrated in figure 2.7. In the diffractogram, peaks are made where this phase shift causes

constructive interference. XRD can provide information about the size of the unit cell, crystal structure and other parameters which can be used to identify any crystalline material.

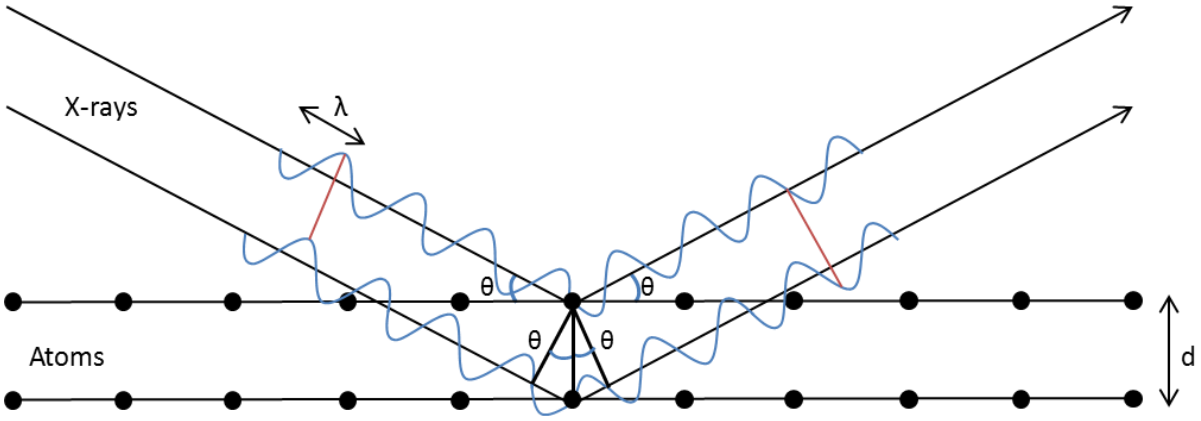

Figure 2.7: Illustration of Bragg's law showing the relation between the distance between the imaginary atomic planes, *d*, the wavelength of the x-rays, λ, and the angle between the x-rays and the atomic planes, θ.

2.4.2 SEM

A scanning electron microscope is used to provide high resolution images of a sample. To produce these images, the instrument fires electrons, from an electron gun, at the sample. These electrons penetrate up to 1 µm into the sample, where they get scattered. These scattered electrons can be either backscattered electrons (BSE) or secondary electrons (SE), which are made from two different processes. BSEs are electrons that are reflected back by the electrostatic forces from the atomic nuclei. Because of this, heavier elements scatter electrons more than lighter elements. Thus, BSEs can provide information not only about the topography, but also the composition of the sample, as the heavier elements become brighter in these images. SEs are valence electrons ejected from atoms in the sample as electrons from the beam hit them. These have less energy than BSEs, so all SEs are made in the top 10 nm of the surface of the sample as they do not have the energy to escape the sample from deeper down. The information provided from SEs are thus of the surface only.

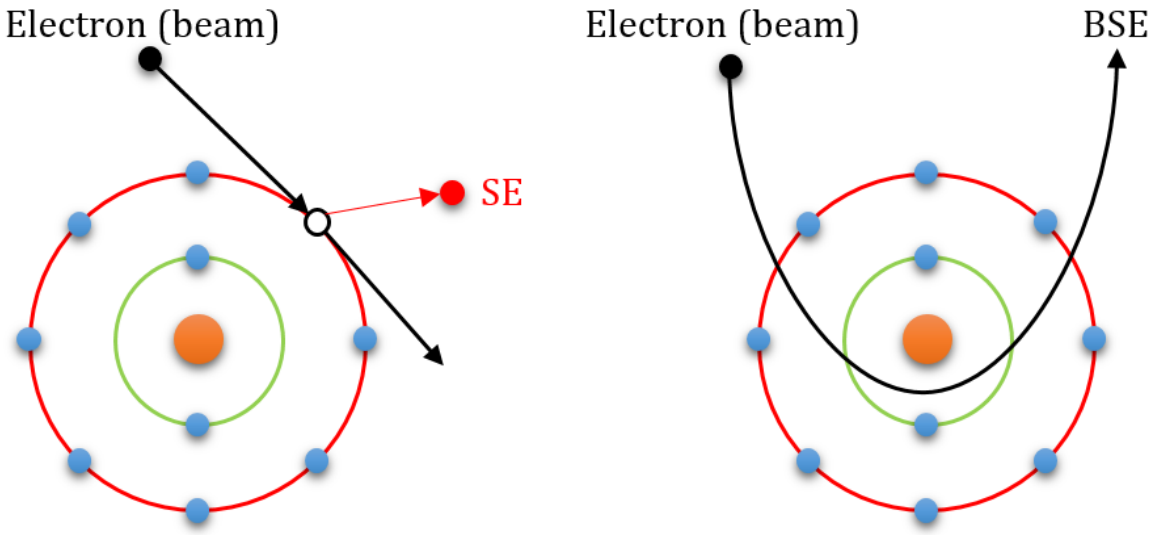

Figure 2.8: Illustration of how the electrons in SEM is scattered. The SEs interact with valence electrons of the atom it hits, causing them to leave the atom. The BSEs only interact electrostatically with the nucleus. Retrieved from [11].

3 Literature

3.1 Background

As the use of batteries has increased there has been a significant rise in the interest of SSBs. The idea is to stop using the liquid electrolyte of modern batteries and implement a solid electrolyte. Until quite recently this has been deemed difficult as most solid-state electrolytes have a rather poor conductivity. When Murugan et al. presented their findings of the LLZO in 2007, [19] the interest in this material exploded. With a reported conductivity of 3.0×10^{-4} S/cm at room temperature and a good chemical stability against Li metal a lot of effort has been put into this group of materials.

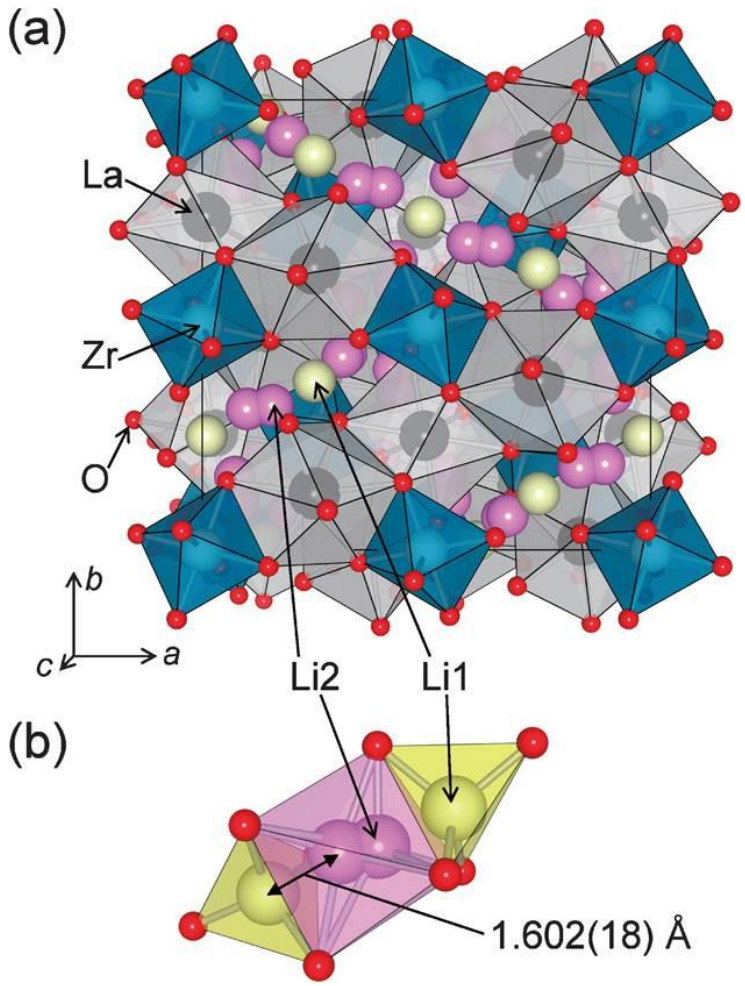

Figure 3.1: a) The crystal structure of cubic LLZO. b) Illustration of the two different Li-sites in the structure. Li1 sits in the tetragonal 24d site, while Li2 sits in the octahedral 96h site. Retrieved from [27].

LLZO exists in two different phases, the tetragonal (*I41/acd*) and the cubic (*Ia-3*), with a theoretical density of 5.108 g/cm^3 for the cubic phase. [27] The cubic phase is the more conducting of the two phases. [23] However, this phase is not stable at room temperature. A phase transition occurs at about 650°C in the undoped LLZO. [28] As the cubic phase of the LLZO is the desired phase, the interest in doping of the material got an upsurge in 2011when Geiger et al. reported increased stability for the cubic phase by doping of Al into the structure. [23] Several other dopants can be used for this, like Ta, Ga and Al. [29] Ta will substitute the B-site ($Li_7La_3Zr_{2-x}Ta_xO_{12}$), making it an acceptor dopant. The relative positive charge of the Ta^{5+} to the Zr^{4+} creates Li-vacancies as charge compensating defects. The creation of vacant Li-sites will stabilize the structure. [23, 30] The Al and Ga on the other hand substitutes the A-sites, creating $Li_{7-3x}M_xLa_3Zr_2O_{12}$ (M=Al, Ga). The trivalent ions creates a surplus of positive charge, causing the creation of Li-vacancies as charge compensating defects which will, like for the B-site doping, help stabilize the cubic structure. The research done into the effects of doping of the material is further looked at in section 3.3.

In recent years, several review papers have been written on the topic, looking at different solid Li-conductors for the use in SSBs. [13, 31-33] Here LLZO is often mentioned as one of the more promising materials.

3.2 Synthesis

In literature there are several synthesis routes described, both by solid-state reaction and by the sol-gel technique. While different routes have been used, it is agreed upon that a temperature of around 1200°C is needed during sintering for the solid-state synthesis to achieve the cubic phase when no dopant is used. [34, 35] Sintering times for the samples varies from article to article. By adding dopants, it is also possible to lower the sintering times and temperatures. Sintering times up to 36 hours is reported for the formation of c-LLZO in the undoped state. Geiger et al. showed in 2010 that it is possible to achieve c-LLZO through sintering times of 12 hours by including Al as a dopant, [23] while Kotobuki et al. showed that Al-doping lowers the temperature needed for the formation of c-LLZO by 230°C. [35] (How the use of dopants affects the sintering and the formation of c-LLZO is discussed further in the next chapter.)

While solid-state synthesis was used in this thesis, a sol-gel approach is also a choice for synthesizing LLZO. [34, 36-38] A variation of the Pechini method is usually chosen, often with the precursors in a nitrate form. It has been reported that the use of the sol-gel method could lower the sintering temperature and improve the density as the homogeneity improves. [37]

3.3 Doping

There are several possible elements used for doping LLZO, substituting the Li-, La-, and Zr-sites with aliovalent dopants. Doping with Al on Li-sites first came from the alumina crucibles being used for the synthesis of the samples, proven by Geiger in 2011. [23] Furthermore, they believe that the Al diffuses into the material through melt phases made from Li_2CO_3which dissolves small amounts of the Al_2O_3. As Li evaporates, the structure has a tendency to collapse into other phases, like $La_2Zr_2O_7$. By the introduction of Al into the vacant Li-sites, the structure is stabilized. What Geiger et al. also saw was that Al stabilizes the more conductive cubic phase of LLZO. Al amounts of around 1.3 wt% were seen in the samples prepared in alumina crucibles. Bernstein et al. later demonstrated, in 2012, that the Li-vacancies are responsible for the stabilization of the cubic structure of LLZO, and that an increased amount of vacancies lead to more cubic phase. [39] This explains why the structure is stabilized by the introduction of Al^{3+} on the Li-sites, producing two Li-vacancies.

Using this, Rangasamy et al. presented in 2011 a study of the effects of the amount of Al-dopant and Li-content on the structure of the LLZO. They found that the minimum amount of Al needed to stabilize the cubic phase is 0.204 moles per mole LLZO. Meanwhile, the maximum amount of Al being soluble in the structure is 0.389 moles per mole LLZO. At Al concentrations higher than this $LaAlO_3$ is formed as a secondary phase. [30] Additionally, Rangasamy et al. found that the Li concentration also affects the structure of the LLZO. In the case of using a too low Li concentration level ($x<5.63$, in $Li_xLa_3Zr_2O_{12}$) the impure phase of $La_2Zr_2O_7$ is formed along with the cubic phase of LLZO. On the other hand, a high Li concentration (up to $x=6.24$) causes the formation of the tetragonal LLZO phase. This lead to the conclusion that, even though there was a constant Al content of 0.24 moles, there seems to be both an upper and lower Li-concentration limit for the formation of cubic LLZO. Using these data, Rangasamy et al. prepared a sample with an optimal composition of $Li_{6.24}Al_{0.24}La_3Zr_2O_{11.98}$, showing a conductivity of 4×10^{-4} S/cm at room temperature.

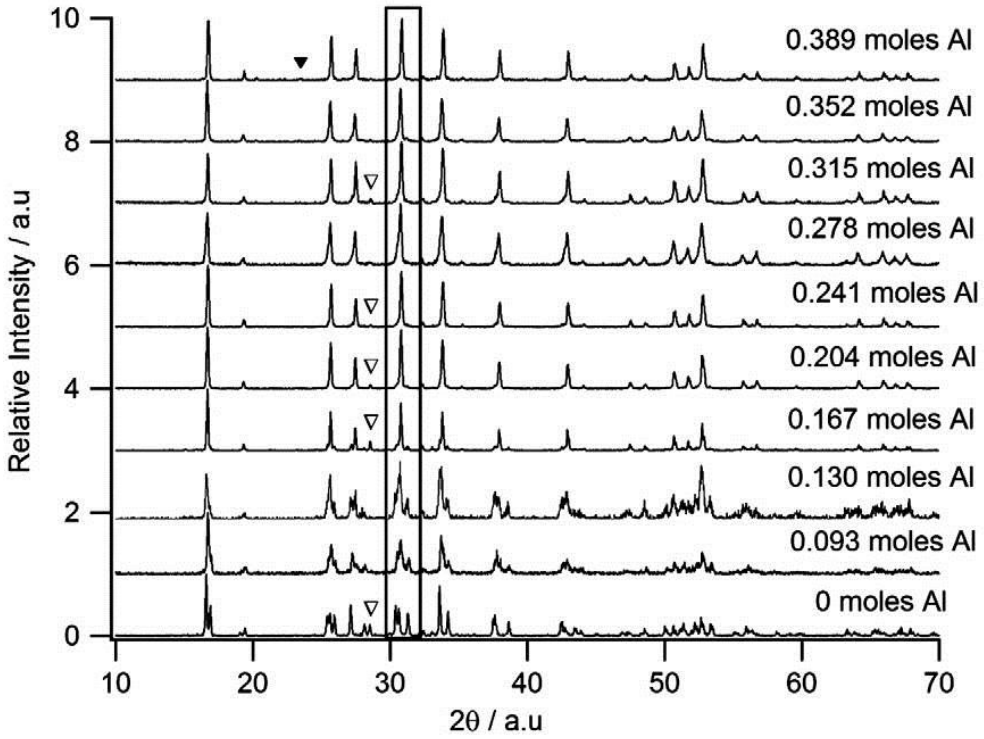

Figure 3.2: XRD pattern from Rangasamy et al. showing how the level of Al doping affects the structure. The white triangles mark peaks for $La_2Zr_2O_7$ and the black triangle, for 0.389 moles Al is $LaAlO_3$. Retrieved from [30].

While doping with Al has been proven effective for stabilizing the cubic LLZO, many other elements have also been used. Wolfenstine et al. studied, in 2012, the effect of Ga-doping on the LLZO. As expected, the Ga behaves much like Al, promoting the cubic structure. It does, however, exhibit a slightly lower conductivity than the Al-doped sample from Rangasamy et al., showing 3.5×10^{-4} S/cm at room temperature. [40] Bernuy-Lopez et al. reported, in 2014, a total conductivity as high as 1.3 mS/cm at room temperature for a Ga-doped LLZO sample, which is one of the highest conductivities ever measured for garnet structured materials. [17]

Doping of the Zr-site is also a possibility for stabilizing the cubic structure. To substitute the tetravalent Zr^{4+}-ion, a pentavalent ion is used, often Ta^{5+}. Thompson et al. proved in 2014 that LLZO doped only by Ta promotes the cubic structure, though dependent on the amount of dopant. [41] To compensate for the higher valent substituent Ta^{5+}, Li-vacancies are formed. While acceptor doping of both the Li- and the Zr-site leads to the formation of Li-vacancies, doping of the Zr-site might be advantageous for the conductivity of the sample. As Al^{3+}, with its larger radius, substitutes the Li-site, it could have a blocking effect on the Li-ions diffusing through the lattice (illustration in figure 3.3), as shown by Li et al. [42] By acceptor doping the Zr-site, charge compensating Li-vacancies still form, but the Li-ion diffusion pathways

remain unaffected. [43] On the other hand, the effective charge of the Ta-dopant is +1, creating one Li-vacancy. Instead, for Al/Ga-doping it is +2, creating two Li-vacancies.

Shin et al. also studied how multidoping of LLZO would affect the conductivity. In 2015, they found that doping of the structure with both Al and Ta causes the Al^{3+} substituents to occupy the 96h site instead of the 24d site, due to the Ta^{5+} in the Zr-site. This leads to more open diffusion pathways for the Li-ions and thus a higher conductivity. [43]

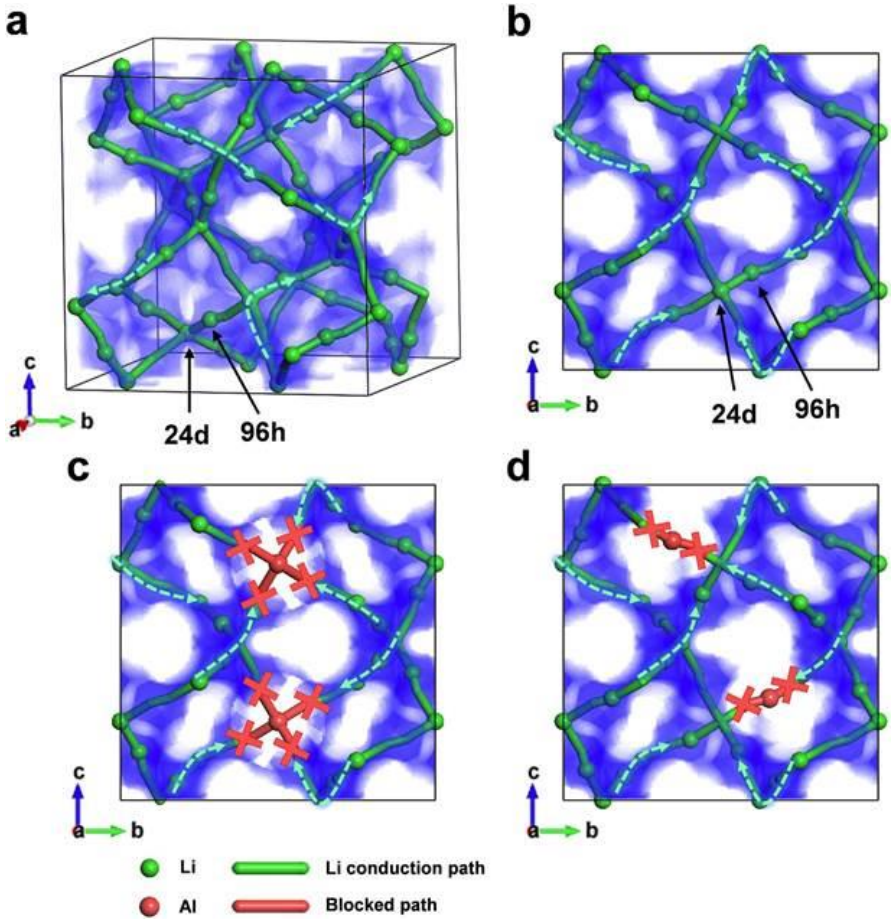

Figure 3.3: Illustration of the blocking effect of Al in LLZO. Green arrows show Li^{+}-ion diffusion while red crosses marks the paths blocked by Al. a) and b) show the undoped cubic structure. In c), Al^{3+} has occupied the 24d site, and in d) Al^{3+} occupies the 96 h site. Clear that doping of the 24d site is more blocking for diffusion of Li^{+}-ions. Retrieved from [43].

While only Al, Ta and Ga doping and combinations of these has been discussed in this section, the effect of other materials has also been studied. W^{6+} doping of the Zr-site has been proven as a viable alternative to Ta^{5+} doping as it has a higher valence than the Ta ions, showing promising results. [44, 45] Other dopants investigated for substituting Zr are Y^{3+} [46] and Nb^{5+}, [47, 48] where the former reduced the sintering time for c-LLZO. An alternative for Al^{3+} and Ga^{3+} doping of the Li-site is using Fe^{3+}, shown by Wagner et al. to be a promising

candidate for further research. [49] Hanc et al. studied the effect of Ca^{2+} and Nd^{3+} doping of LLZO, where they substitute La. However, the conductivity values were below most other doped variants. [47] In 2011, Kumazaki et al. studied an LLZO variant doped with Al^{3+} and Si^{4+}. The highest conductivity reached with this doping was ~6×10^{-4} S/cm. [50] Lastly, the work of Pershina et al., from 2017, involved doping samples with the glass ceramic $LiPO_3$, resulting in a maximum conductivity of 1.1×10^{-4} S/cm. [51]

3.4 Conductivity Measurements

Since Murugan et al. reported the high conductivity in LLZO in 2007, 3.0×10^{-4} S/cm at room temperature, [19] many have tried to improve on these numbers. Different synthesis routes and dopants have been attempted to improve these results. The conductivities and activation energies reported from articles referred to in this thesis are presented in table 3.1, below. All the values are measured at room temperature.

Table 3.1: Reported values for the conductivity of LLZO at RT, with various doping levels, from articles mentioned in this thesis. (* - Not reported)

Conductivity (S/cm)	**Phase**	**Activation Energy (eV)**	**Dopant**	**Synthesis method**	**Article**
3.0×10^{-4}	Cubic	~ 0.3	-	Solid-state	[19]
5.67×10^{-5}	Tetragonal	0.35	-	Solid-state	[52]
2.3×10^{-5}	Tetragonal	0.41	-	HNO_3 + microwave	[53]
2.0×10^{-4}	Cubic	*	Al	Sol-gel	[34]
1.4×10^{-4}	Cubic	0.35	Al	Solid-state	[35]
1.3×10^{-3}	Cubic	~ 0.3	Ga	Sol-gel	[17]
8.7×10^{-4}	Cubic	0.22	Ta	Co-precipitation	[29]
3.7×10^{-4}	Cubic	0.30	Ta, Al	Co-precipitation	[29]

3.5 Defect Chemistry of LLZO

Limited work has been done on the defect chemistry of the LLZO and its doped variants. It is widely accepted that the conductivity and stability of the c-LLZO is caused by the formation of Li-vacancies. [30, 39, 41, 43, 54, 55] As aforementioned, the use of higher valent dopants on the Li site creates more Li-vacancies. The use of 3-valent elements, like Al or Ga, as dopants creates 2 Li-vacancies and thus increases the stability of the material as well as making the synthesis of c-LLZO easier. This, in turn, increases the conductivity of the material.

The work of Kubicek et al., from 2017, focused on the defect chemistry of oxygen in the structure. [54] They first determined that oxygen vacancies are the only defects expected at the O-site, as an interstitial will, like the Li-vacancy, have an effective negative charge. The O-vacancy, on the other hand, is thought to function as a charge compensating defect for the vacant Li sites. This way, an increase in concentration of oxygen vacancies will also lead to a higher concentration of Li-vacancies, causing the conductivity to increase. In the same article it is reported that Ta-doping on the Zr site seems to form a higher concentration of O-vacancies than Al/Ga-doping of the Li-site, but the Li-concentration remains the same. In the samples with doping on the Li-site, they also reported an increase in the concentration of O-vacancies as the conductivity increased.

Zhan et al., 2018, investigated the effect of how defects in LLZO affect the conductivity and how the oxygen partial pressure affects the concentration of these defects. [55] What they found was that the concentration of oxygen vacancies affects the conductivity, which is in accordance with the result of Kubicek. When pO_2 is increased, the conductivity goes down, as the concentration of vacancies decreases. The same effect is seen for lithium vacancies, which further confirms the findings of Kubicek et al. Furthermore, Zhan et al. constructed a Brouwer diagram for the defects of LLZO (figure 3.4).

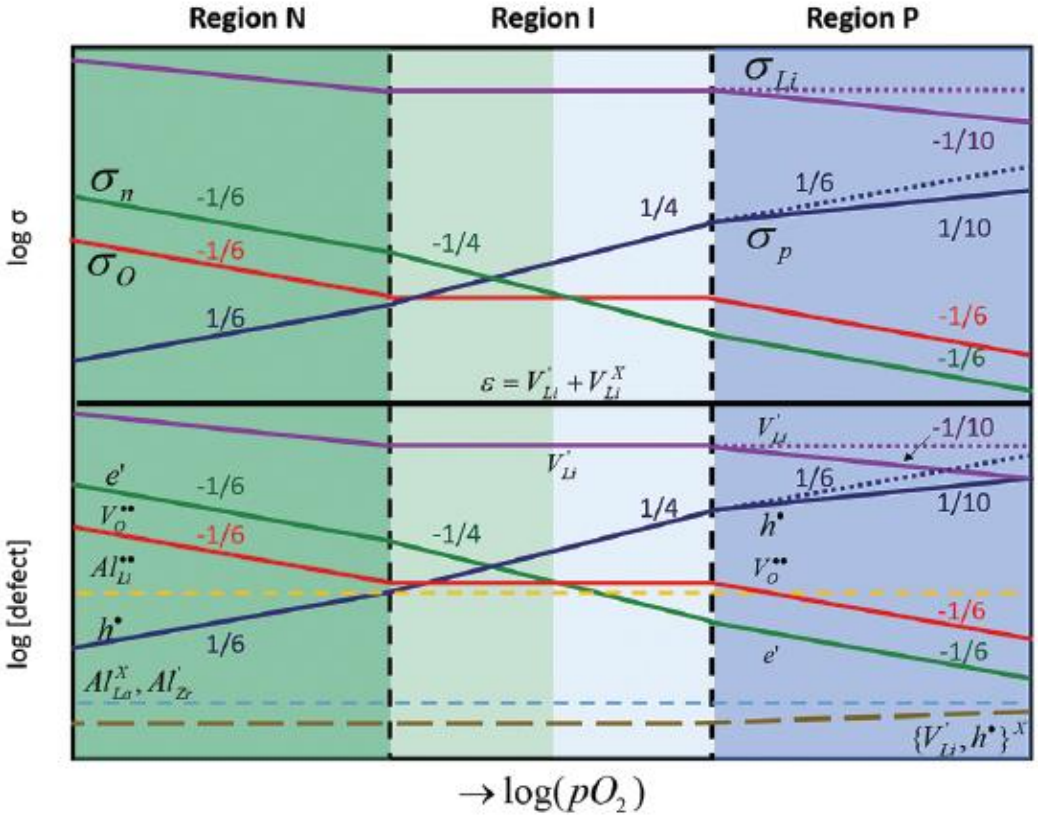

Figure 3.4: The Brouwer diagram made by Zhao et al. Here it is clear that the ionic conductivity decreases with increasing pO_2, with a decreasing concentration of Li- and O-vacancies. Retrieved from [55].

This diagram is in good agreement with other literature. Following the concentration of oxygen vacancies and lithium vacancies they both fall as pO_2 is rising. Additionally, this causes the Li-ion conductivity to decrease, which is according to reported results. [54, 55] One notable feature is the rapid increase in concentration, and thus conductivity, of electron holes as the pO_2 rises.

3.6 Effects of Moisture

How LLZO responds to changes in pH_2O has been studied by some. Jin et al. investigated, in 2013, a one year old LLZO sample which had been stored in ambient air. XRD confirmed decomposition of the surface into $La(OH)_3$ and Li_2CO_3, and they believe that the decomposition begins at the grain boundaries. Additionally, the sample was found to be mechanically weak. [56] Jin et al. also subjected fresh powders of LLZO to water for 1 week. Facile Li^+/H^+-exchange was then proven through pH measurements of the water, as $Li_{7-x}H_xLa_3Zr_2O_{12}$ formed.

This exchange has also been seen by other studies. Galven et al. studied the effect of moisture from air on other Li-garnets, e.g. $Li_7La_3Sn_2O_{12}$ and $Li_5La_3Nb_2O_{12}$. In the former, a spontaneous Li^+/H^+-exchange in air was seen. [57] In a later study, they revealed that not all Li-garnets exhibit this Li^+/H^+-exchange. Only the Li-garnets containing a Li-concentration exceeding that permitted by the general garnet formula ($A_3B_2C_3O_{12}$) displays the exchange. [58] However, these samples were not subjected to moist air, but the powders were subjected to a solution of ethanol and benzoic acid. Nyman et al. also showed this exchange with LLZO in water. [59]

Shimonishi et al. studied the effects of an aqueous solution on $Li_6La_3Zr_2O_{11.5}$ in 2011. Sintered pellets of the material were submerged in an aqueous solution of saturated LiCl for a week. Samples still showed quite high conductivity, 6.5×10^{-4} S/cm, after they were dried in vacuum. It was suggested that the material could be used as a protective layer for electrodes in future Li-air batteries. [38]

4 Experimental

4.1 Preparation

Samples were prepared in different ways, with various amounts of Al added to them. In table 4.1 below, compositions, grinding technique and sintering temperatures are presented for the different samples.

Table 4.1: List of the amount of Al dopant (in moles), the grinding technique and sintering times and temperature for the samples.
*There were problems regarding the oven and temperature controller during sintering of LAL25. Details on page 35.
**The program of the temperature controller did not work as intended, causing the sample to sinter longer than the planned 12 hours.

Sample name	Al-amount	Structure formula	Grinding	Sintering temp. (°C)	Sintering time (h)
LLZU	0	$Li_7La_3Zr_2O_{12}$	Agate mortar	1150	13.5**
LAL25	0.25	$Li_{6.25}Al_{0.25}La_3Zr_2O_{12}$	Agate mortar	1060-1090*	*
LAL20	0.20	$Li_{6.4}Al_{0.20}La_3Zr_2O_{12}$	Agate mortar	1150	12
BAL20	0.20	$Li_{6.4}Al_{0.20}La_3Zr_2O_{12}$	Agate ball milling	1150	12
BAL20-12	0.20	$Li_{6.4}Al_{0.20}La_3Zr_2O_{12}$	Agate ball milling	1200	12

To prepare the samples for this thesis, solid-state synthesis was used. Some samples were prepared using a mortar, doing the grinding by hand, while for others, ball milling was used. All samples were intended to sinter for 12 hours. To compensate for loss of Li at high temperatures, 10% excess Li_2CO_3, relative to the intended stoichiometry, was added to all samples.

Precursors: The materials used for the doped and undoped samples are the same, with the exception of the added Al_2O_3 for the doped sample.

Table 4.2: Information about the precursors used for the synthesis of the samples. The grain size of the powder was only provided for the ZrO_2, at 5 µm.

Chemical formula	Manufacturer	Purity	Lot nr.
Li_2CO_3	Sigma Aldrich	≥ 99.0%	BCBD9386V
La_2O_3	Aldrich	≥ 99.9%	SLBR6484V
ZrO_2	Aldrich	99%	BCBT9962
Al_2O_3	Merck	-	TA163195

The precursors were weighed in to reach the intended stoichiometric amounts. Since La_2O_3 is highly hydroscopic and forms $La(OH)_3$, the powder was dried at 900°C for 12 hours to make sure it was in the form of La_2O_3. The dry La_2O_3 was then kept in a desiccator.

Grinding: For the first samples; LLZU, LAL25 and LAL20, the powders were mixed by grinding them by hand in an agate mortar for 10-15 minutes. As the results of these samples were below expectations when it came to porosity and mechanical strength, a different grinding approach was made. A PM100 planetary ball mill, from Retsch, was used. The powders were mixed with agate balls and vial in isopropanol at different conditions (see table 4.3). After the milling, the mixture was put in a glass beaker and dried in a heating cabinet at 120°C until the isopropanol had evaporated.

Table 4.3: Parameters for the ball milling of BAL20 and BAL20-12.

Sample	RPM	Duration (h)	Intervals (min)	Wait (min)	Ball-to-powder weight ratio
BAL20	400	8	20	4	26
BAL20-12	400	8	20	4	23.3

Pressing and sintering: ~1.5 g of the mixed powder was pressed to a pellet at different pressures (see table 4.4) using an Atlas Manual15T pellet press (Specac). The die size used was 20 mm.

Table 4.4: Pressure used in pellet press when pressing the pellets and the ramp rate used while sintering.

Sample	Pellet press pressure (MPa)	Ramp rate (°C/min)
LLZU	156	6.5
LAL25	125	6.5
LAL20	237	4.0
BAL20	156	4.0
BAL20-12	156	4.0

The green pellet was put in an alumina crucible on a bed of sacrificial powder from the same batch, to prevent unwanted Al-doping from the alumina crucible. More sacrificial powder was put on top of the pellet to limit evaporation of lithium, and then a lid was put on top of the crucible. A ProboStat was used for the sintering to be able to control the atmosphere inside the cell. The crucible was put inside the cell and dry air was run through it to avoid moisture. The sample was heated to the target temperature and sintered for 12 hours, with varying ramping rates (see table 4.4).

During the sintering of LAL25, there were some problems regarding the furnace and temperature controller. The intended sintering temperature was 1150°C, but the maximum temperature reached was 1090°C. The temperature at which the sintering happened was probably between 1060 and 1090°C. Furthermore, the furnace did not start the cool down at the intended time, which caused the sintering time to be longer than the planned 12 hours, but the actual sintering time is unknown. What caused this issue is not known.

Samples after sintering: Some of the samples were weighed and the thickness was measured (diameter is fixed from pressing) before sintering, to compare with the pellet after sintering.

Table 4.5: Physical size of the samples before and after sintering. The diameter and thickness are average values from measuring 2-4 places on the sample.

Sample		Weight (g)	Thickness (mm)	Diameter (mm)	Density (g/cm^3)
LAL20	Before	1.51	1.67	20	2.88
	After	1.26	1.75	20.16	1.97
BAL20	Before	1.51	1.78	20	2.29
	After	1.20	2.1	16.9	3.01
BAL20-12	Before	1.50	1.98	20	2.41
	After	1.28	1.68	16.97	3.36
LLZU	Before	1.50	-	20	-
	After	1.23	1.85	19.56	2.22

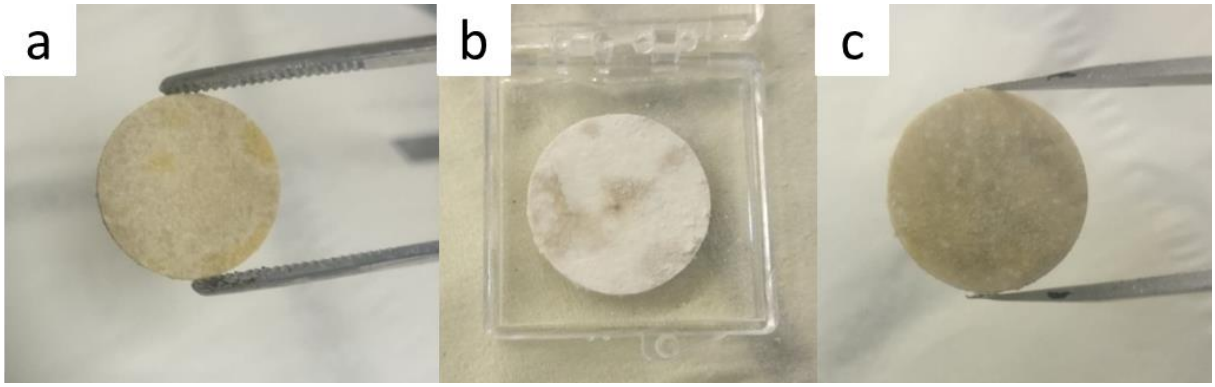

Figure 4.1: The samples BAL20 a), LLZU b) and BAL20-12 c) after sintering.

BAL20-12 storage: BAL20-12 was prepared shortly after BAL20. As the impedance spectroscopy of BAL20 took longer than expected, BAL20-12 was left in the cell it was sintered, in a dry air atmosphere at ~175°C, for 50 days. It was then characterized and prepared for impedance measurements as described above.

4.2 Characterization

4.2.1 XRD

To characterize the phase composition of the samples produced and confirm that we had the desired composition, X-ray diffraction was used. For characterization of the pellets themselves, they were put in a deep holder. In the holder, the surface of the pellet was adjusted to be leveled with the edge of the holder. Glass holders were used for diffraction of powder-samples. In this case, a small amount of powder was mixed with a few drops of isopropanol and mixed in an agar mortar. A uniform layer of this mix was put on a glass plate. When the isopropanol had evaporated, there was a thin and uniform layer of powder.

Two different XRD-instruments were used in this work:

A MiniFlex 600 Benchtop XRD from Rigaku. This XRD uses both $Cu_{\alpha 1}$ (1.5406 Å) and $Cu_{\alpha 2}$ (1.5444 Å) as there is no monochromator. The XRD was done using a scan range of $10°<\theta<90°$ with a step size of 0.020° and a total scan time of 60-70 minutes.

A D8 Discover by Bruker AXS with a Cu $K_{\alpha 1}$ radiation (λ=1.5406 Å) and a Ge (111) Johanssen monochromator. Unlike the MiniFlex 600, it uses Bragg-Brentano geometry. The XRD scans were done using a scan range of $10°<\theta<70°$, with a step size of 0.020° and 0.1 s/step and a total scan duration of about 10 minutes.

The diffractograms were analyzed using the program DIFFRAC.EVA, by Bruker. The peaks were identified and indexed by comparing them to the Powder Diffraction File (PDF) database by the International Centre for Diffraction Data (ICDD).

Samples LLZU, LAL20 and LAL25 were characterized by the Miniflex 600 XRD. Samples BAL20 and BAL20-12 were characterized by the D8 Discover. BAL20 was, additionally analyzed after the impedance measurements, to check for any changes due to the pH_2O-dependency measurements.

4.2.2 SEM

A SEM was used to investigate the surface of the samples and to provide high resolution pictures. The SEM used for this work was a Quanta FEG 200 F by FEI Company. The instrument is coupled with an EDAX Pegasus 200 EDS detector. Scattered electrons were detected by a detector for backscattered electrons and an Everhart-Thornley detector for secondary electrons. The SEM operates at high vacuum mode, using a FEG electron gun with an acceleration voltage of 20 kV.

4.3 Impedance Measurements

After the sintering was completed and the sample was cooled down to room temperature, Li-blocking Ag electrodes were painted to both sides of the sample and the size of the painting noted. It was then left to dry in a heating cabinet at 120°C for 30 minutes.

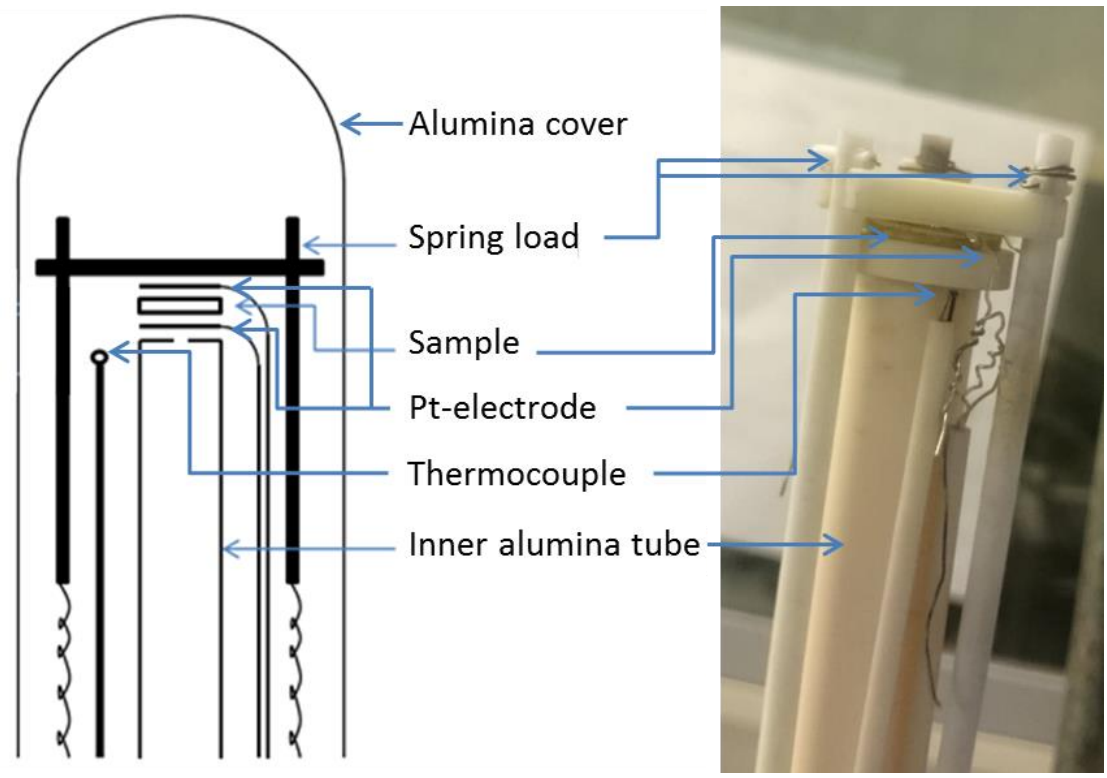

Figure 4.2: Illustration of the setup inside the ProboStat cell (left) and how the setup actually looks (right). The sample is held in place by an alumina spring load, preventing it from falling down, with Pt electrodes on both sides. There are gas in- and outlets both in the inner alumina tube and between the inner tube and the cover.

The sample was placed in between two Pt wires, being in contact with the Ag electrodes. This, again, was held in place by a spring load alumina assembly. This sat on top of a hollow alumina tube. Finally, a closed alumina tube was put around the entire setup. To control the atmosphere, a gas inlet and outlet was placed in the inner tube, and another set for the outer tube, in principle allowing for different atmospheres at different sides of the sample. The temperature was measured by an S-type thermocouple being placed leveled with the sample. This allowed the temperature controller to regulate the furnace to keep the desired temperature.

The ProboStat cell was then put vertically into the tubular furnace, where it was adjusted to make the sample in the middle of the furnace. Next, the cell was connected to the gas mixer through copper tubing. This was used to control the atmosphere inside the cell.

Figure 4.3: Left: The cell; without the alumina cover (in front) and with the alumina cover (back).
Right: The cell sitting inside the tubular furnace, connected to the Solartron 1260 (black wires), temperature controller (orange wire) and to the gas mixer (cobber tubes).

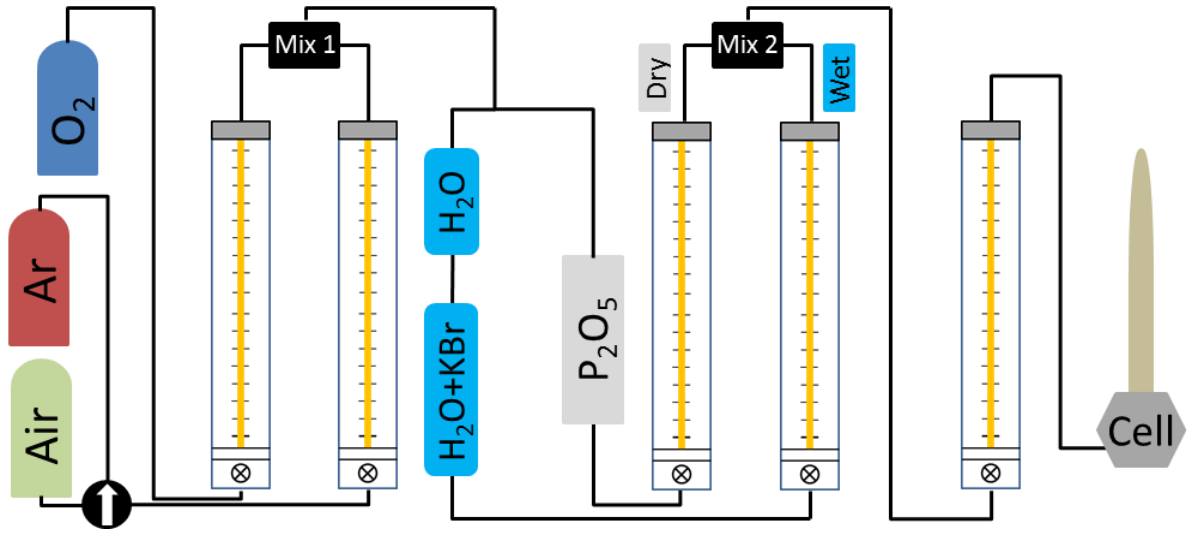

Figure 4.4: Schematic representation of the gas mixer. The second flowmeter uses either Ar or synthetic air, which can be altered by turning the arrow. The pure gases mix in mix 1. Nest, the mixed gas goes through the wetting stage or the drying stage.

The impedance spectroscopy was done using a ProboStat™ cell made by NorECs AS, connected to a Solartron Instruments 1260. The Solartron 1260 analyzer was connected to the sample with a 2-point, 4-wire setup, connecting high current and voltage to one side of the pellet and low current and voltage to the other side. Sweeps were done with different frequency ranges, at different temperatures and with an AC voltage of 50 mV. The temperature ramping rate between sweeps was 2.5°C/min. A more detailed description of the sweeps is provided in the next sections, about the measurement series' at different atmospheres.

4.3.1 Dry Air Measurements

The synthetic air is dried by a drying stage in the gas mixer before entering the cell. The drying stage contains solid P_2O_5, as a dehydrating agent, to absorb moisture in the gas.

Measurement series 1

The first series was done on samples LLZU and LAL25. The samples were heated to 125°C before sweeps were done from 125°C and every 25°C down to room temperature, like pictured in figure 4.5. The frequency range for this series was 2 MHz to 0.1Hz.

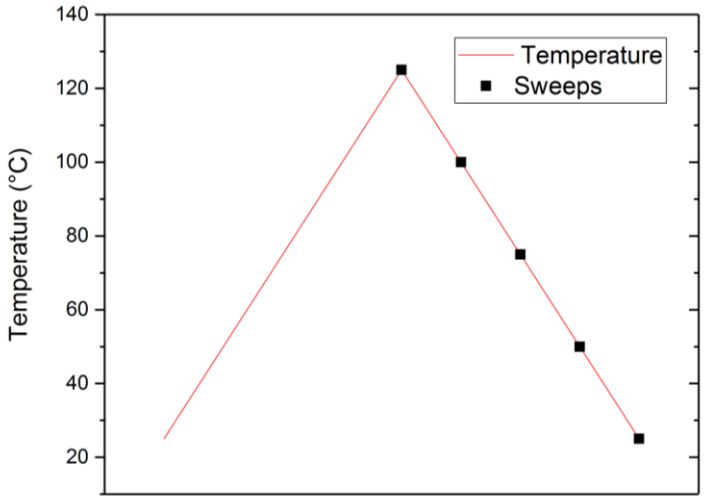

Figure 4.5: Temperature curve with measured sweeps for measurement series 1

Measurement series 2

The second measurement series was done on sample LAL20. First measurement start at 55°C, then 125°C, 150°C and then at every 50°C up to, and including 500°C. Then the same was done, cooling the sample, measuring at every 50°C. This is pictured in figure 4.6, below. The frequency range for the sweeps in this series was 2 MHz to 0.1 Hz.

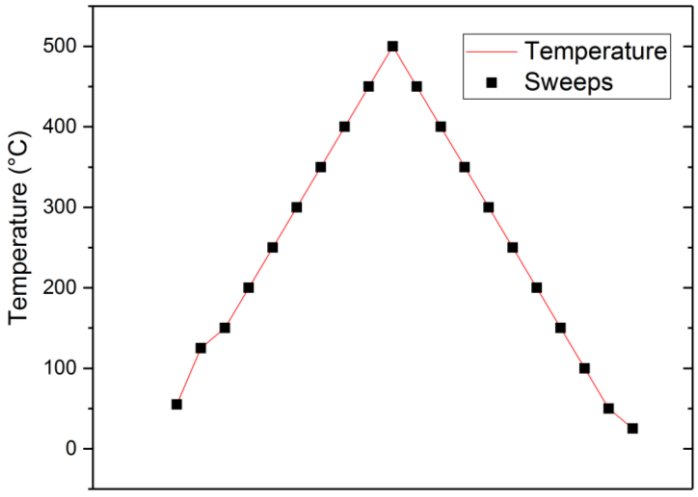

Figure 4.6: Temperature curve with measured sweeps for measurement series 2

Measurement series 3

The third series was conducted on BAL20. Measurements start at room temperature, and then sweeps were done every 25°C (50°, 75° etc.) up to 300°C. The same is done from 300°C back down to room temperature. To check the reproducibility of the results, the sample was again

heated, and sweeps were done at every 25°C up to 300°C. Figure 4.7 pictures the sweeps as the temperature was changed. The frequency range for the sweeps was 10 MHz to 10 mHz.

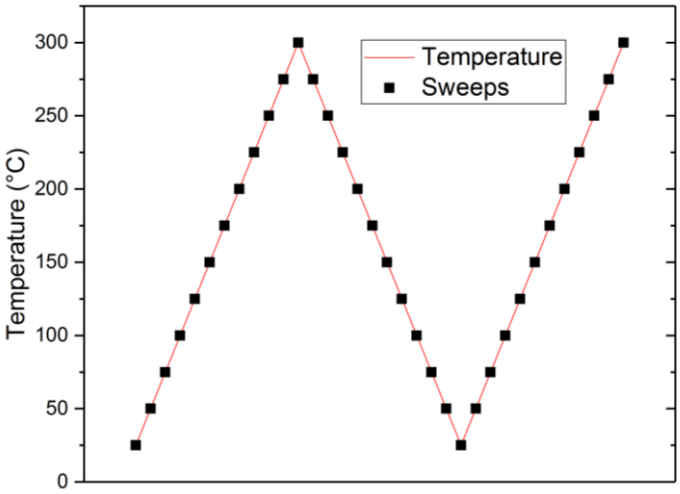

Figure 4.7: Temperature curve with measured sweeps for measurement series 3.

Measurement series 4

The fourth series was conducted on BAL20-12. While the 3 previous series' were done manually, this was programmed to perform the measurements by itself. A program, made by L. Henriksen, conducted sweeps once the temperature was within ±0.5°C of the target temperature. Once the sweeps was complete, the temperature was changed. This allowed for more efficient measurements, as this program ran over night, saving days of work. The downside of this is that the sample does not have the time to properly reach equilibrium.

Measurements started at 30°C then at 50°C, followed by sweeps at every 50°C up to 350°C. Then to check to for reproducibility of the results, the sample was cooled to room temperature and reheated to 350°C, with sweeps being done at every 25°C (illustrated in figure 4.8). The frequency range was 10 MHz to 1 Hz. This series was performed on a setup not containing a potentiostat, so to reduce noise in these plots; an AC voltage of 500 mV was applied.

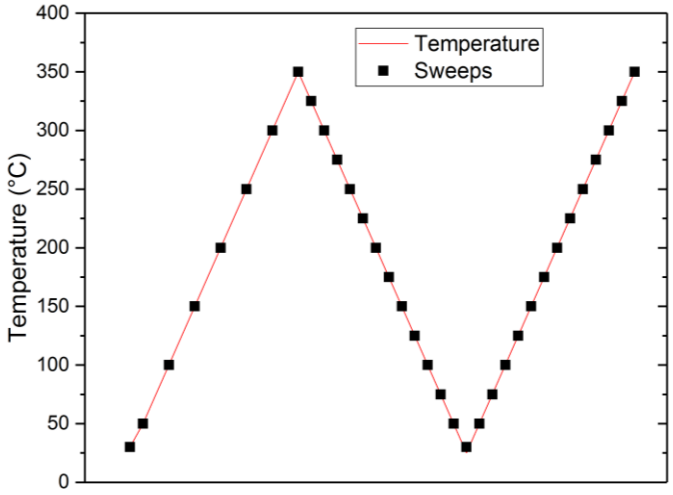

Figure 4.8: Temperature curve with measured sweeps for measurement series 4.

4.3.2 pO_2 Dependency Measurements

To investigate how the conductivity of the sample is affected by oxygen, the O_2 partial pressure was changed and the impedance measured over time. These measurements were conducted on BAL20 and BAL20-12. The gas mixer was used to control the flow of gas. The program ProGasMix, by NorECs, was used to calculate the amount of the different gases in the cell during equilibrium. [60]

The Solartron 1260 was used to measure Z' vs. time, as the sample adjusted towards equilibrium to keep track of the change in resistance as the atmosphere is changed. Next the gas mixer was adjusted to the intended flow of gases. This measurement was done at a constant frequency of 10 kHz. When equilibrium was reached, a sweep was done. This process was repeated at different partial pressures of O_2, where the O_2 was diluted with Ar to adjust the pO_2 in the cell.

BAL20: The sweep range for BAL20 was 10 MHz to 10 mHz. Sweeps were performed at various pO_2. First sweep was conducted in a pure O_2 atmosphere (pO_2=1 atm). Next, the atmosphere was approximately 50/50 of O_2 and Ar, at pO_2=0.57 atm. Sweep 3 and 4 were done at pO_2=0.1 and 0.03 atm, respectively. Finally a sweep was performed in a pure Ar atmosphere. All measurements were done at 300°C.

BAL20-12: The sweep range for BAL20-12 was 10 MHz to 1 Hz. Like for BAL20, there were done sweeps at 5 pO_2 values. First at pure O_2, then at three diluted atmospheres, with

pO_2=0.5, 0.1 and 0.03 atm. The next sweep was conducted in pure Ar, before the sweeps were repeated, but now with rising pO_2 levels. The temperature was then adjusted to 300°C, and the sweeps were repeated.

4.3.3 pH$_2$O Dependency Measurements

Few, if any articles, discuss the effect of water vapor for the conductivity of LLZO. Moisture in the air is known to cause degradation of LLZO (see section 3.6). Here the effect of an applied pH$_2$O at high temperature was investigated. This was done by running a gas through a wetting stage in the gas mixer. This wetting stage contained two stages where the gas first passed through a flask of distilled water. Next, it flows through a saturated solution of water and KBr salt. The salt is added to keep the relative humidity of the gas at ~80%, to prevent it from condensing in the tubes. This causes the pH$_2$O of the gas to be 0.0250 atm at 25°C. The cell was kept at T $\geq$ 250°C to keep the water as vapor, and to avoid water forming on the surface of the sample. As a moist atmosphere could lead to degradation of the sample, pH$_2$O dependency measurements was the last thing the sample was exposed to.

The impedance was measured much like it was for the pO_2 measurements. The pH$_2$O was set by adjusting the gas mixer, and then impedance (Z') was plotted vs time, measuring at a frequency of 10 kHz. When the sample came to equilibrium, a sweep was done. Then the pH$_2$O was again adjusted to the next value. 5 values of the pH$_2$O was used in the atmosphere in cell; 0.025 (which is the maximum partial pressure of water possible using KBr as a drying agent at RT), 0.013, 0.005, 0.001 and 0 atm.

To check for different responses to the moist atmosphere from the samples, the pH$_2$O dependency was tested at different temperatures and atmospheres. The conditions for the measurements for BAL20 and BAL20-12 are presented in table 4.6 and 4.7, respectively.

BAL20: The frequency range of the sweeps was 10 MHz to 10 mHz.

Table 4.6: Temperature and atmosphere for the pH_2O dependency measurements for BAL20.

Measurement nr.	Temperature (°C)	Atmosphere
1	300	Synthetic air
2	250	Synthetic air
3	250	Synthetic air
4	300	Argon
5	350	Argon

BAL20-12: The frequency range was 10 MHz to 1Hz.

Table 4.7: Temperature and atmosphere for the pH_2O dependency measurements for BAL20-12.

Measurement nr.	Temperature (°C)	Atmosphere
1	250	Ar
2	250	Synthetic air
3	300	Synthetic air
4	300	Ar
5	350	Ar
6	350	Synthetic air

4.3.4 Impedance Data

The results from the impedance spectroscopy were fitted using Zview (version 3.5a, Scribner Associates, Inc.). To calculate the total conductivity, the following formula was used:

$$\sigma_{tot} = \frac{d}{A} \cdot \frac{1}{R_{int}} \tag{31}$$

Where *d* and *A* are the thickness of the sample and the area of the electrode, respectively, and R_{int} is the resistance at the interception with the x-axis.

4.4 Sources of Error

Throughout the work done and all the methods and instruments used, there are many sources of error to the results, from known errors in instruments like the SEM and XRD to unknown errors such as contamination from uncleaned mortars and vials. While not all can be accounted for, the most notable will be discussed and considered when finding the results. The errors from the XRD and the SEM instruments are well known and documented and will therefore not be further discussed here

Errors stemming from the preparation of the pellets could be unforeseeable. Contamination from the equipment being used, e.g. the pellet press, mortar or vial, is always a possibility. To prevent such issues, the equipment can be washed before use, in case of dirty equipment. Another possible source of uncertainty is the issue of grinding powders by hand. This is not a very effective way of mixing powders, compared to using the ball mill. By not grinding the powders thoroughly, secondary phases could form during sintering. The precursor powders themselves could also be prone to causing errors. As the La_2O_3 is hygroscopic, it could form $La(OH)_3$ during storage. By using a "wet" La_2O_3 powder, the stoichiometry of the pellet would not be correct, as the two materials have different weight, density and La per formula unit. However, as mentioned earlier, this issue is prevented by heat treating the powder before it is used, and then store it in a dry place after. While these are errors that could arise, but are hard to predict, other issues are more quantitative, like the weighing balance exhibiting an error of ±0.1 mg.

The ProboStat cell and the connected gas mixer could be prone to leakage. It is expected, reading from the manual, that even though a gas passes through the drying stage of the mixer,

a certain pH_2O is present. The partial pressure of H_2O is calculated to be 3×10^{-5} atm by Norby. Additionally, a $pO2$ of 1×10^{-5} atm is expected. [61] As the gas mixer controls the flow of gas into the ProboStat cell, and thus the atmosphere around the cell, it is important to be able to control the partial pressures of different gases. However, the flowmeters on the mixer are not very accurate, exhibiting an inaccuracy of ±5%, per flowmeter in use, causing the error to increase with the number of flowmeters used.

To measure the impedance, a Pt electrode was used. This was put into contact with the Ag electrode that was painted onto the pellets. It turns out the Pt is prone to corrosion at higher temperatures, possibly inhibiting a proper measurement of the impedance of the sample, as the corrosion layer is a poor conductor. This is discussed in more detail in section 6.4.

Another potential issue regarding the impedance spectroscopy is the instrumentation used for measurement series 4. Here a program was used to automate the measurements to save time. However, as the program starts the sweeps when the temperature is within ±0.5°C the sample does not have the time to properly reach equilibrium. This could cause slight errors in the impedance values.

4.4.1 Solartron 1260

The instrument used for measuring the impedance of the samples, the Solartron 1260, has an accuracy of impedance values of ±0.1%.

The Solartron 1260 that was used to measure the impedance of the first samples (LLZU, LAL25 and LAL20) turned out to have a serious fault in the voltage input (V1) used for measuring the impedance, recording a much lower voltage than what is applied, the relation between the applied voltage and the measured voltage changes as the applied voltage increase. This made a recalculation of the results from LLZU, LAL25 and LAL20 impossible, measured in measurement series' 1 and 2, forcing the impedance data from these samples to be discarded.

Measurements on later samples were performed using V2 as voltage input, or with another spectrometer.

5 Results

Due to the issues with the Solartron 1260, described in section 4.4.1, no impedance data is available for LLZU, LAL20 and LAL25. Therefore, only structural effects of the synthesis routes are considered for these samples. Furthermore, the two samples there is impedance data from are made through basically the same synthesis route. This makes it difficult to say anything about how the conductivity is affected by the density and structure of the pellets.

5.1 Phase Analysis

XRD analysis was performed on all samples, to analyze the phase composition. The XRD patterns of all the samples are plotted in figure 5.1.

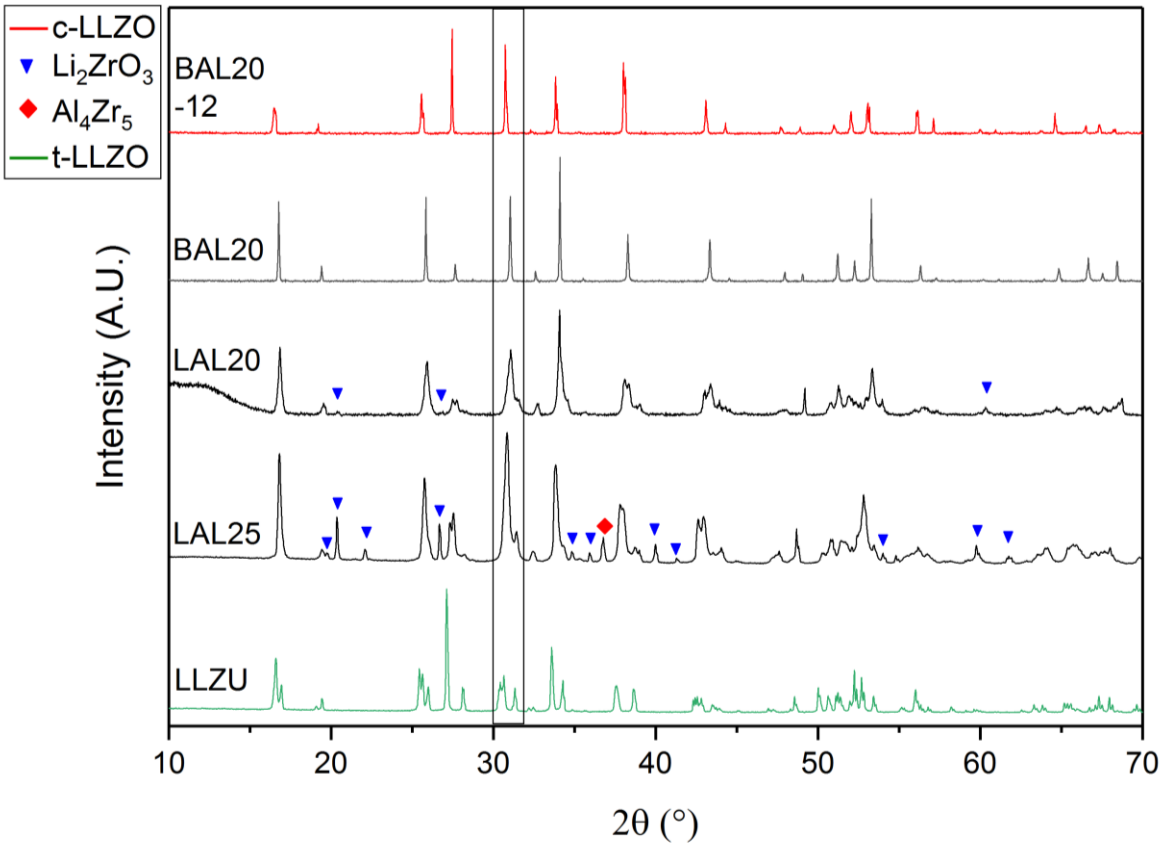

Figure 5.1: The XRD patterns from the 5 samples. BAL20-12 and BAL20 are purely c-LLZO, while LLZU is purely t-LLZO. Two secondary phases were found in LAL20 and LAL25, Li_2ZrO_3 and Al_4Zr_5, which are marked in the diffractograms of the samples. The framed peaks are an indication of which phase is present, c-LLZO or t-LLZO. If this is a single peak, it is c-LLZO. If there are two peaks, it is tetragonal. For a split peak, the sample consists of both phases.

From this it is clear that samples BAL20 and BAL20-12 consist only of the cubic phase of LLZO. The undoped sample, LLZU, is pure tetragonal phase. The other doped samples, LAL20 and LAL25, consist of both the cubic and tetragonal phase of LLZO. The peak at $2\theta \approx 31°$, which is framed in figure 5.1, is an indication of which phase is present. For the cubic phase, this is a single peak, as seen in BAL20-12 and BAL20. In the diffractogram of the tetragonal phase, on the other hand, it is split into two peaks, as seen for LLZU. In the case of the other two samples, this peak is widened for LAL20, and partly split for LAL25, indicating that both phases are present in these samples.

The diffractograms of BAL20 and BAL20-12 have narrow peaks. The peaks for the other three are wider. While a wider peak could be a sign of smaller particles, the difference probably stems from the XRD instruments used. LLZU, LAL20 and LAL25 were all characterized by the Miniflex 600. This is a smaller and simpler machine than the D8 Discover used for BAL20 and BAL20-12. Considering BAL20 and BAL20-12 were both ball milled for 8 hours, it does not seem probable that the samples grinded by hand would have a smaller grain size. Due to this, estimating the real grain size is difficult.

5.1.1 BAL20 after Measurements

BAL20 was characterized both before and after the impedance spectroscopy, including the $p\mathrm{H_2O}$ dependency measurements.

There are no signs of phase changes in the sample. No new phases can be seen, neither is there a phase transition towards the tetragonal phase, as the peak at ~30° is still a singlet. The only difference is the intensity of the peaks. The silver electrode was polished away before the XRD was performed, and no Ag is seen in the diffractogram. BAL20 is considered to have been unaffected by the water vapor from the $p\mathrm{H_2O}$ dependency measurements.

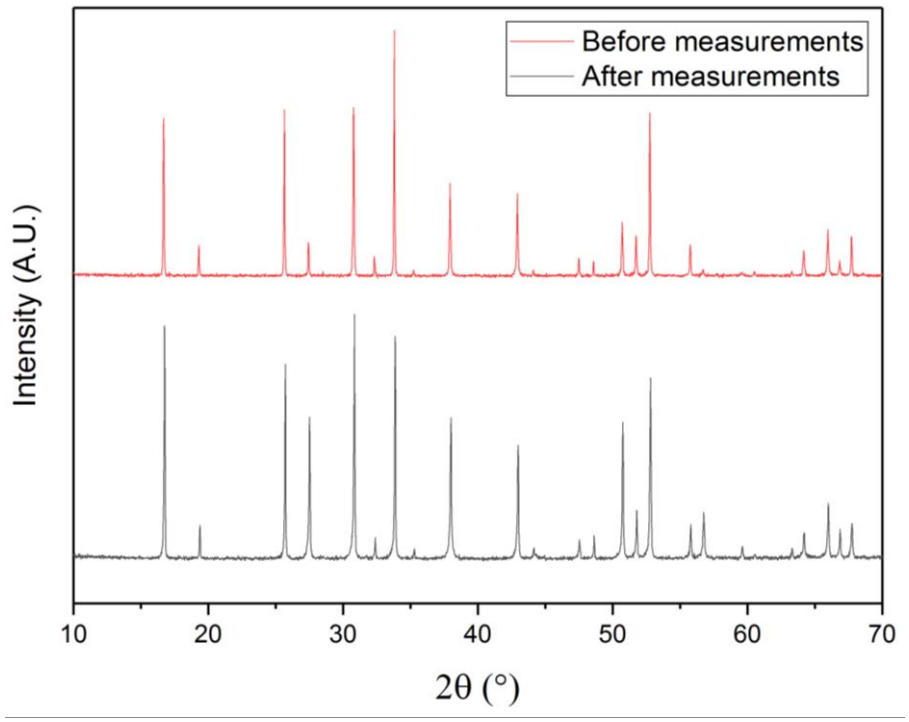

Figure 5.2: The XRD pattern of BAL20 before and after impedance spectroscopy was conducted. No new peaks are seen, only difference is in peak intensity.

5.2 Microstructure and Morphology

5.2.1 Density

After sintering was finished, samples were weighed and their thickness and diameter measured, to calculate their relative densities. The measured and calculated values are presented in table 5.1.

Table 5.1: Volume, weight and relative density of the samples (no data for LAL25).

Sample	Volume (cm^3)	Weight (g)	Relative density
LLZU	0.556	1.235	43.5%
LAL20	0.641	1.260	38.6%
BAL20	0.399	1.200	58.9%
BAL20-12	0.380	1.277	65.8%

From table 5.1 it is clear that ball milling the powders increases the density of the samples. The difference in density for the samples grinded by hand comes from a more random difference in how well and for how long they were grinded. As all samples had approximately the same amount of powder used for the pellets, 1.5 g, it is also clear that the balls milled samples sinter better, which is due to smaller grain size and thus more contact area between the grains.

5.2.2 Surfaces

To further investigate the surface morphology and internal microstructure of the samples, they were looked at with an SEM, before the impedance spectroscopy.

The undoped LLZU is the least dense sample out of the ones studied in the SEM. This is also clear from the SEM pictures of its surface. In figure 5.3 a), the pores are visible, even at 40x magnification. BAL20 and BAL20-12 have less porous surfaces than LLZU, and have a more similar surface morphology to each other. The structures of the surfaces are still comparable between the three samples, looking like a network of sintered grains. BAL20-12 however, looks slightly better sintered and thus more dense (figure 5.3 e) and f)). There are no visible grains in any of the surfaces, suggesting the surfaces sinter well, or might even create a melt.

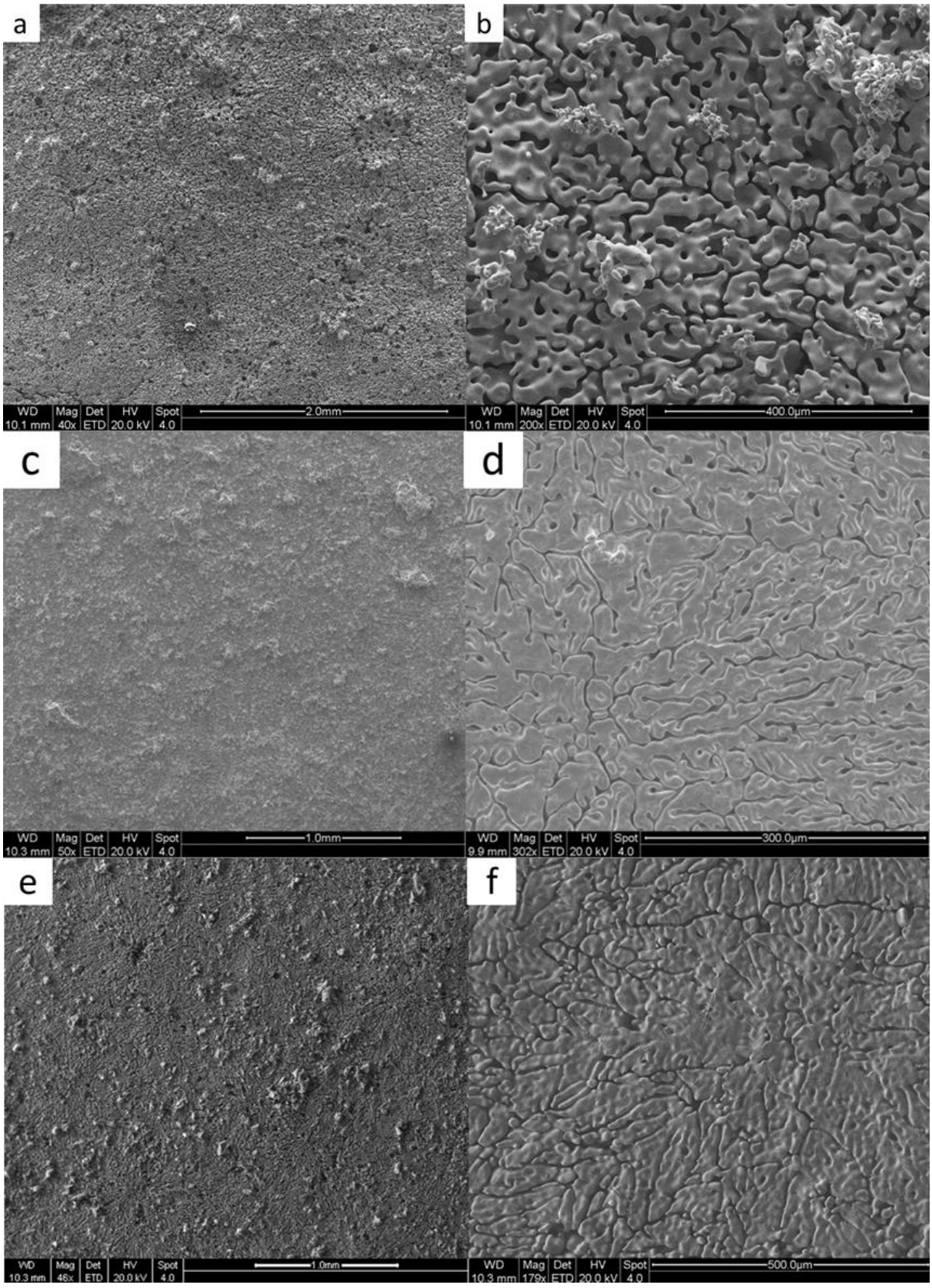

Figure 5.3: SEM pictures showing the surfaces of LLZU, a) and b), BAL20, c) and d) and BAL20-12, e) and f). Pictures a), c) and e) are overviews, with a low magnification. b), d) and f) are higher magnifications of the same surface.

5.2.3 Internal Microstructure

A piece of LLZU broke off shortly after sintering. This offered a possibility to study the interior of the sample, and how the grains had evolved on the inside.

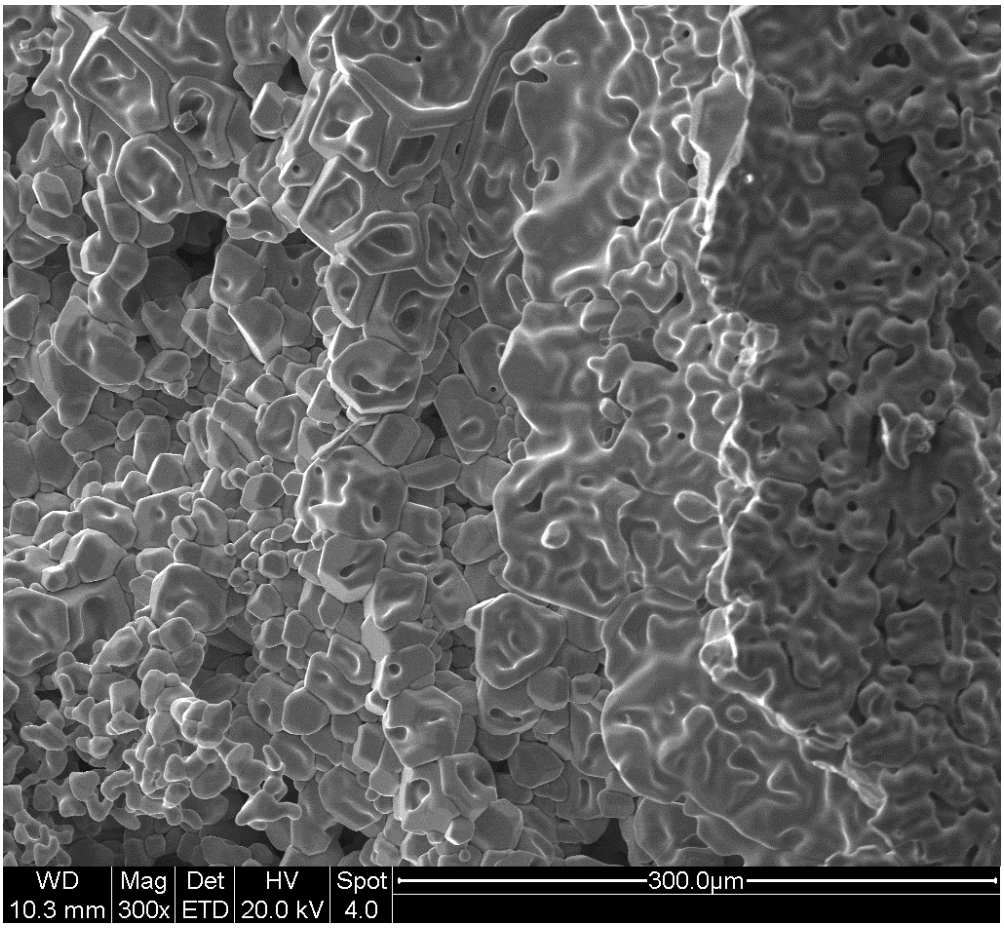

Figure 5.4: SEM picture from the break point of LLZU. Here the surface of the pellet is seen to the right, and the further left the further into the sample we see.

Figure 5.4 shows the break point in the sample. Here it is possible to see both the surface and the interior of LLZU and how the structure changes further into the sample. The surface has no clear grains. Instead, the structure is sintered together, almost looking like it has melted at some point. Further into the sample, individual and more grain-like structures start to form. Even deeper in the sample, to the left in the picture, individual grains are clearly visible, suggesting the interior of LLZU has not sintered as well as the surface.

In figure 5.5 details seen in LLZU are presented. These are from the left-most area in figure 5.4. Here we see more crystal-like structures and fewer pores. The grain size varies a lot, from grains < 5 µm (figure 5.5 b)) to larger grains, such as the one towards the lower left of figure 5.5 a), at >50 µm. This difference in grain size is probably a result of the grinding.

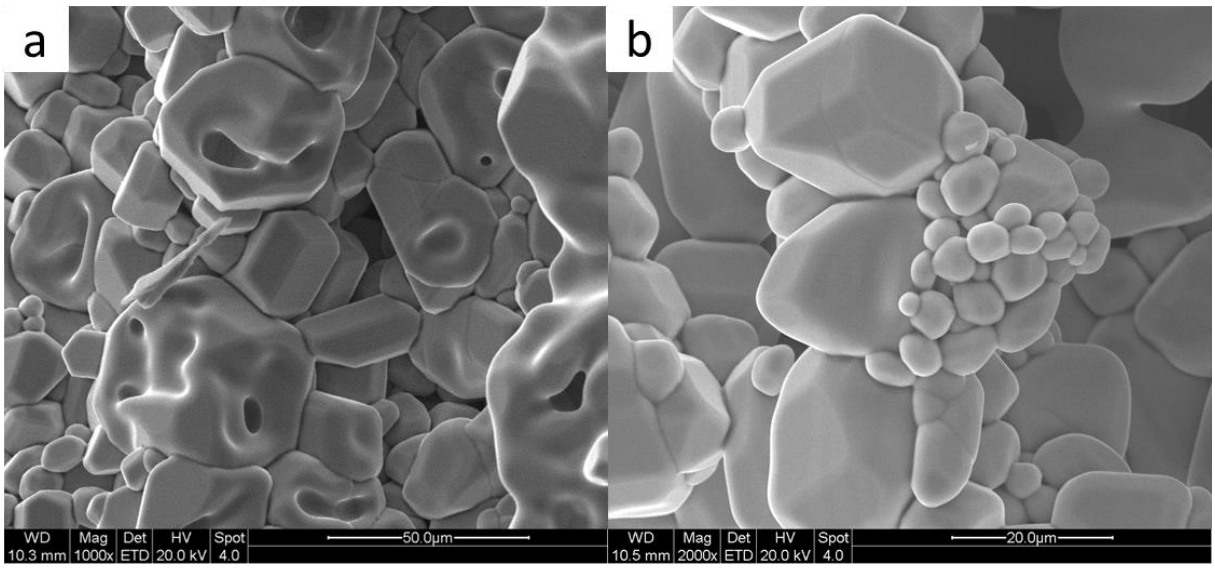

Figure 5.5: SEM pictures of details in the interior of LLZU. Inside, the sample looks rather dense, forming crystal-like grains.

After the impedance spectroscopy was completed for LAL20, it was intentionally broken in half, to investigate if the Ag electrode had reacted with the pellet in the interface between them. The result of this is presented in section A.2 in the appendix. However, breaking the pellet allowed for studying the inside of the sample (figure 5.6).

There are no clear crystal structures in LAL20, neither are there any clear grains at all, making it challenging to determine any grain size. The morphology is similar to that of the surface of both this sample and BAL20 and BAL20-12 where the grains have seemingly melted together. Due to this, it is hard to determine the size of the grains. However, some larger pieces are visible, as the grain in the center of the picture, with a size of about 30 µm at its widest. The other structures are smaller.

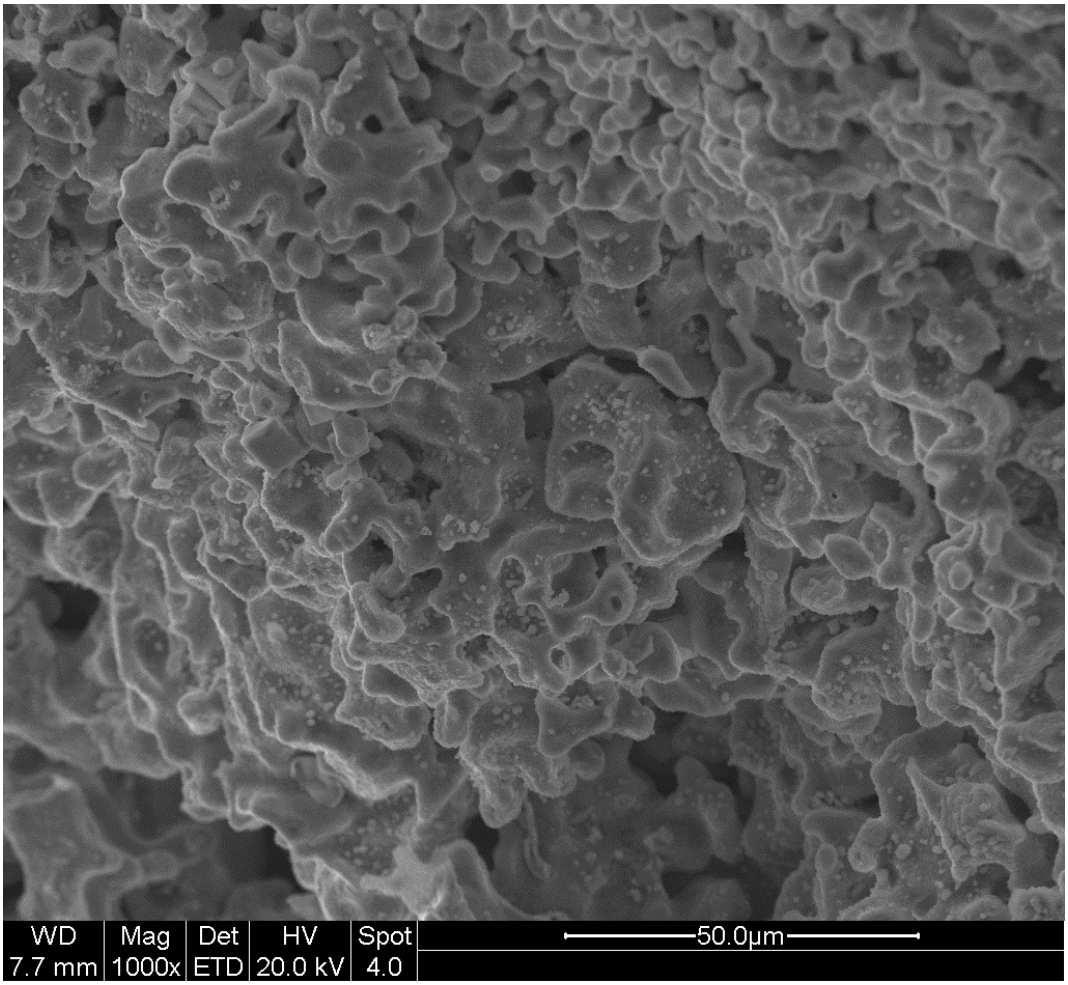

Figure 5.6: SEM picture showing the inside of LAL20. The small particles are Ag from the electrode from when the sample was broken.

5.3 Conductivity

By measuring the impedance of the samples, the conductivity was calculated and is presented in figure 5.7.

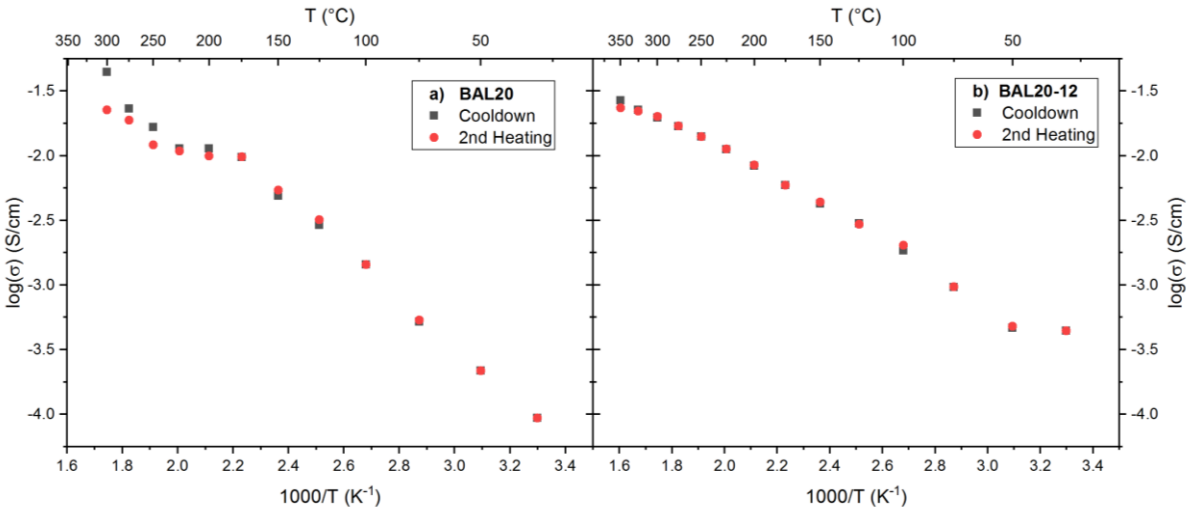

Figure 5.7: Conductivity plot for a) BAL20 and b) BAL20-12. A higher conductivity at the lowest temperatures for BAL20-12 is seen. Both samples show reproducible values at cooldown and reheating of the pellet. In both plots, the data point at RT is a single data point.

This shows conductivity at RT of about 9×10^{-5} S/cm for BAL20, which is as expected and is comparable to literature. For BAL20-12, "room temperature" conductivity was measured at 30°C, and was found to be 4.4×10^{-4} S/cm, which is comparable to the better values seen for the conductivity in literature. However, this data point does not follow the trend shown by the rest of the plot, and with an impedance spectrum which was hard to interpret, this value is probably too high. For both samples, the conductivity is not certain, as the impedance plots were hard to interpret at high frequencies.

At elevated temperatures, the conductivity of BAL20 increases linearly up to 175°C. Here the increase flattens out, before increasing linearly again from 225°C. As for the conductivity of BAL20-12, it shows a linear evolution at all temperatures, with a slight decrease in the slope at the highest temperatures. These effects are further investigated in section 5.3.2, when looking at the activation energy.

5.3.1 Impedance Spectroscopy and Capacitances

The impedance of BAL20 and BAL20-12 has been measured, at different temperatures and atmospheres. Two impedance spectra and the fitting of these are presented below. For the interested reader, additional plots are presented in section A.1 in the appendix.

Data points at frequencies that are multiples of 50 Hz (mainly 50 and 100 Hz) were sometimes removed from the data range as they are subject to interference from the power grid, which operates at 50 Hz.

At high temperatures, part of a semicircle is apparent, at high frequency, but considering the capacitance of this semicircle, it is probably a contribution from the electrode (~10 µF). The electrode semicircle continues into "a tail" seen at low frequencies. Such a tail is an indication of a blocking electrode, suggesting that the material predominantly is an ionic conductor. The electrode, however, is not of interest in this thesis, but the *Warburg*-element is still added here to make a proper fit for the entire plot. The R_{bulk} element is the intercept with the x-axis and reflects the bulk resistance of the sample. The following RC-element is then the "semicircle" formed by the electrode.

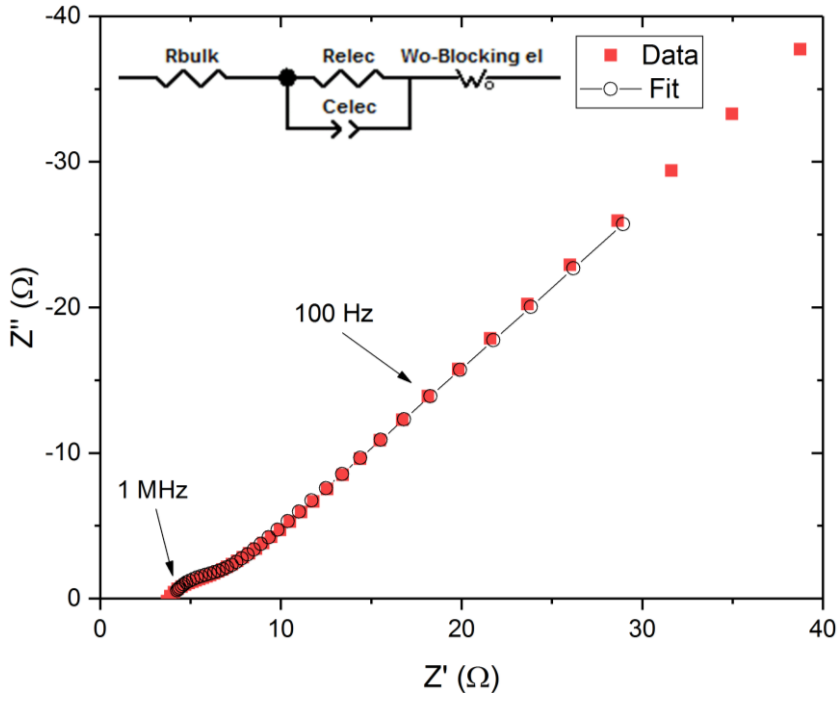

Figure 5.8: Deconvolution of impedance data from BAL20-12, measured at 300°C. At higher temperatures, a semicircle is visible, and is probably the electrode. At lower frequencies, the blocking electrode is seen. The equivalent circuit used is added at the top.

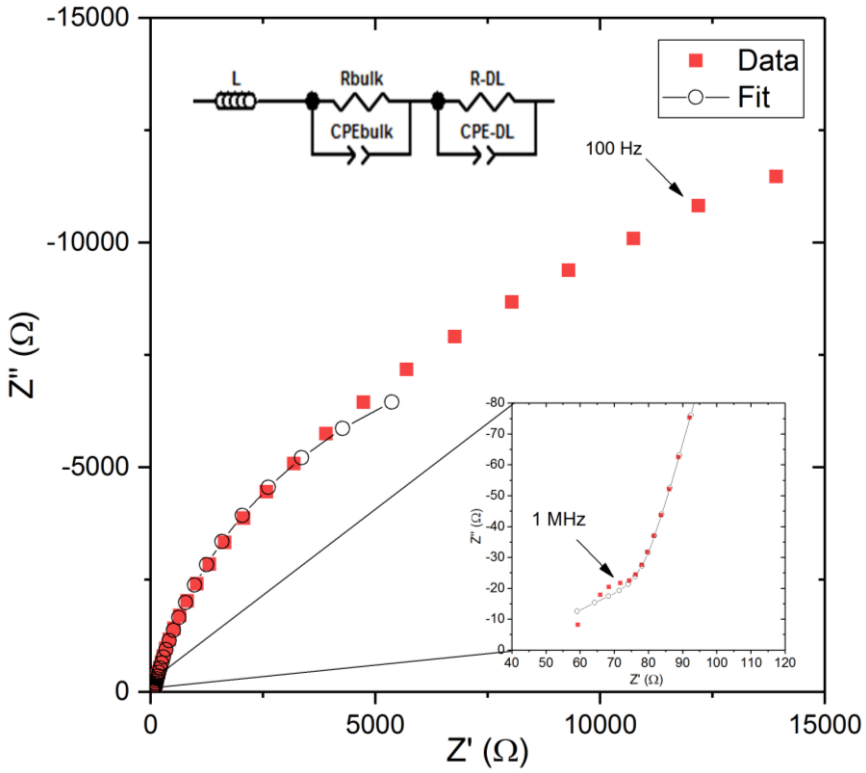

Figure 5.9: Deconvolution of impedance data from BAL20, measured at 100°C. At lower frequency, an electrode blocking effect is seen, but not fitted, as the electrode is not of interest. The equivalent circuit used for the fitting is added, at the top.

At lower temperatures this semicircle is more visible, but still not a complete semicircle. Considering the capacitance values which are lower than what is expected from the electrode, this could be from the grain boundary or it is caused by a double layer, formed at the electrode interface. However, the capacitances could be artificially low due to influences from the electrode "tail". Furthermore, the lack of a clear semicircle at high frequencies could mean that the grain boundary resistance is negligible. These results are in accordance with literature. [30, 35, 40, 43]

At temperatures of 100°C and lower, a second effect is seen. For most plots, the semicircle is too affected by inductance and the larger semicircle to be fitted to an equivalent circuit. As for the plots of 100°C for BAL20 and 30°C for BAL20-12, this small semicircle at high frequency is so distinct that it is possible to fit. In figure 5.9, the impedance plot from BAL20 at 100°C is shown. Here two semicircles are seen, which have been deconvoluted using the equivalent circuit added in the figure. Considering the capacitance values from this fitting, the smaller semicircle is probably the bulk (~60 pF) and the larger semicircle is the electrode (~11 µF). However, due to few data points for the small semicircle, the capacitance value is

rather uncertain. An inductor, with a value of ~2 µH, is used as inductance is seen for the smaller semicircle. The values from the two other plots are about the same.

As the capacity of the larger semicircle is in the region of µF for all the plots at higher temperatures, and the plots at lower temperatures are very affected by noise, it is hard to make a proper plot of the capacitance of the samples. In figure 5.10, the capacitance of the largest of the semicircles in the plots from the measurements done at lower temperatures is taken into consideration when calculating the capacitance. Then, at higher temperature, the capacitance value is taken from the one semicircle visible.

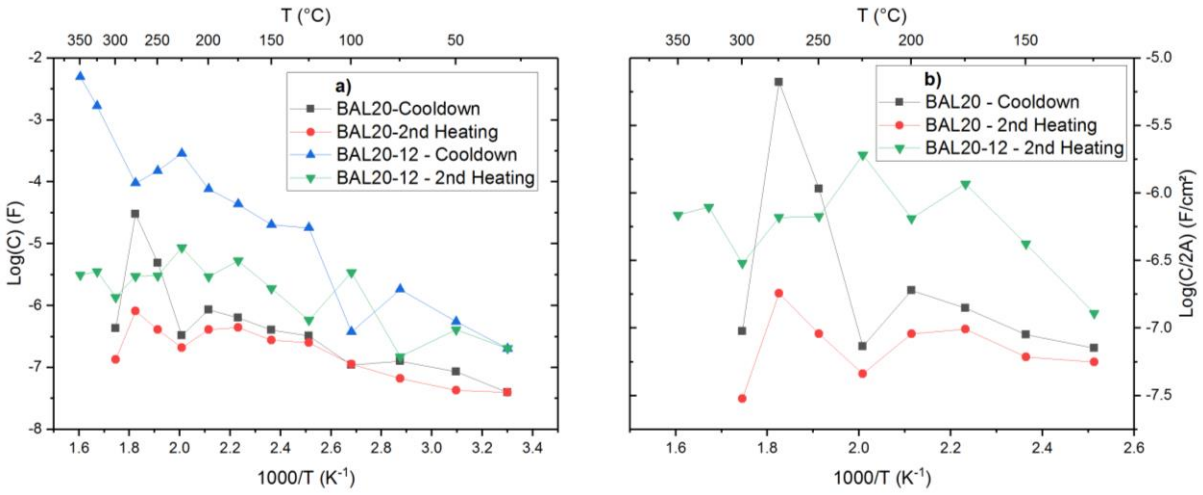

Figure 5.10: a) Plot of capacitance as a function of 1000/T. The values are varying a lot due to challenges regarding fitting of impedance spectra. They do, however, seem to level out at temperatures over 100°C, except for BAL20-12 (cooldown). The plot point at RT is from the same sweep in the two series' from the samples. b) Plot of the parts from a) showing electrode values. Plotted as F/cm².

Figure 5.10 a) shows the capacitances of all the four measurement series' for the two samples. There are significant variations within the plots. Despite this, some conclusions can be drawn. One notable result is the capacitance values at 100°C, which deviates from the rest of the plot for all measurements. This could be from protons as the water might condense and evaporate on the surface of the sample. All graphs seemingly have a temperature dependency below 100°C. Above this temperature, the values stabilize at around 10^{-6} F. This is considered to be the electrode. The parts in 5.10 a) showing electrode values are plotted in figure 5.10 b), normalized for the area of the electrode of the pellet (*C/2A*). At lower temperatures, the capacitance value might be artificially low due to the electrode "tail" affecting the semicircle and thus the fitting. However, for the cooldown of BAL20-12 the capacitance values increase

with temperature throughout the temperature range. As this is not seen for the other plots, the best explanation is that the plots are too affected by the electrode tail (as can be seen in the plots in figure A.1 in the appendix). Major deviations in single plot points are due to challenges during fitting.

5.3.2 Activation Energy

By using the Arrhenius plot of log(σT) vs. 1000/T for the samples, the activation energy and pre-exponential factor for the conductivity was calculated and is presented in the figure 5.11 and table 5.2.

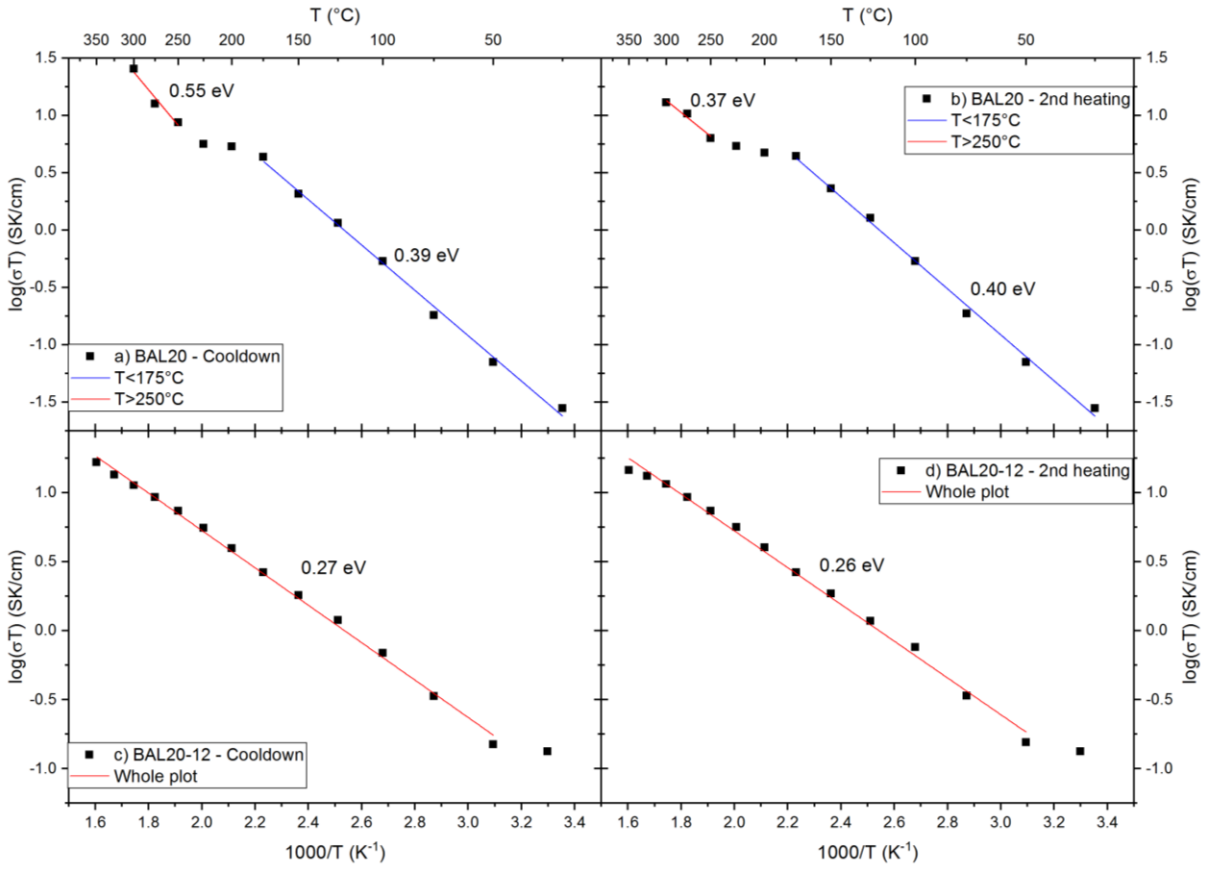

Figure 5.11: a) and b) are Arrhenius plots for BAL20, from measurements done while; a) cooling down the sample and b) heating it up again. The linear fit used to calculate the activation energy of the plots is shown. c) and d) are Arrhenius plots for BAL20-12 while c) cooling down and d) heating the sample back up again. The plot at RT for BAL20-12 is not considered due to its uncertainty.

For BAL20, there is a change in the slope at high and lower temperature. In figure 5.11 a) and b), a change in the slope of the activation energy for BAL20 is clearly visible at ~175°C. Due to this, high and low temperatures were calculated separately, giving different slopes and

activation energies for this sample. For BAL20-12, a slight decrease in the slope is seen at high temperature, but the abrupt change seen in BAL20 is not there. Other than that, the plots are seemingly linear. Because of this, BAL20-12 has been fitted with one linear fit, and thus a single activation energy is calculated for the entire plot.

The activation energy for the samples is quite different. The low temperature region for BAL20 exhibits an activation energy of ~0.4 eV, which is comparable with literature, while for BAL20-12 it is ~0.27 eV, which is low compared to literature (see table 3.1).

In the higher temperature region of BAL20, there is a difference in activation energy compared to what is seen at lower temperature. The high temperature range is >250°C. Here it shows an activation energy at high temperature of 0.55 eV during the cool down, which is 0.16 eV higher than the low-temperature area. A difference this large could mean there is a change in transport mechanism, from the bulk to the grain boundary at higher temperature. However, no semicircle for the grain boundary is seen in the impedance plots. While heating the sample back up, the activation energy becomes 0.37 eV, which is 0.03 eV lower than the low-temperature region for the reheating. The lack of an increase in activation energy in this area suggests that the suggested change in transport mechanism, seen during the cooldown, is either gone or hidden. A reduction in the grain boundary resistance would cause its contribution to the activation energy to decrease. This could be caused by grains sintering together or a change to the composition in the grain boundaries during the reheating of the sample. Another explanation to why the effect is not seen during the reheat is that higher temperatures are needed to see it, due to the slope being affected by the transition area.

For BAL20-12, the activation energy shows a constant decrease with increasing temperature. This tendency is most visible during the 2nd heating of the sample, where the slope dips down at ~300°C. This could be due to a preference in atomic sites for Li. At higher temperatures, Li diffuse randomly through the structure, and sits in all sites. When the temperature decreases, the Li moves to sites that are more energetically favorable, causing them to remain in these sites.

The pre-exponential factor at high temperature for BAL20 is significantly higher for the cooldown than for the reheating of the pellet. This means there are more active sites in the sample before it cools down. Meanwhile, the values at low temperatures are similar for the cooldown and the reheating. BAL20-12, on the other hand, exhibits a notably lower value for the pre-exponential factor compared to what is seen for BAL20.

Table 5.2: Activation energies and pre-exponential factors for BAL20 and BAL20-12.

Sample + temp. range	Activation energy (eV)	Pre-exponential factor (σ_0) (S/cm)
BAL20-Cooldown (low)	0.39	1.6×10^{5}
BAL20-Cooldown (high)	0.55	1.7×10^{6}
BAL20-Reheat (low)	0.40	1.9×10^{5}
BAL20-Reheat (high)	0.37	2.5×10^{4}
BAL20-12 – Cooldown	0.27	3.2×10^{3}
BAL20-12 – Reheat	0.26	3.1×10^{3}

5.3.3 pO_2 Dependency

By measuring the impedance of the samples at different partial pressures of O_2, the dependency of oxygen for the conductivity was found. The results are plotted in figure 5.12, below.

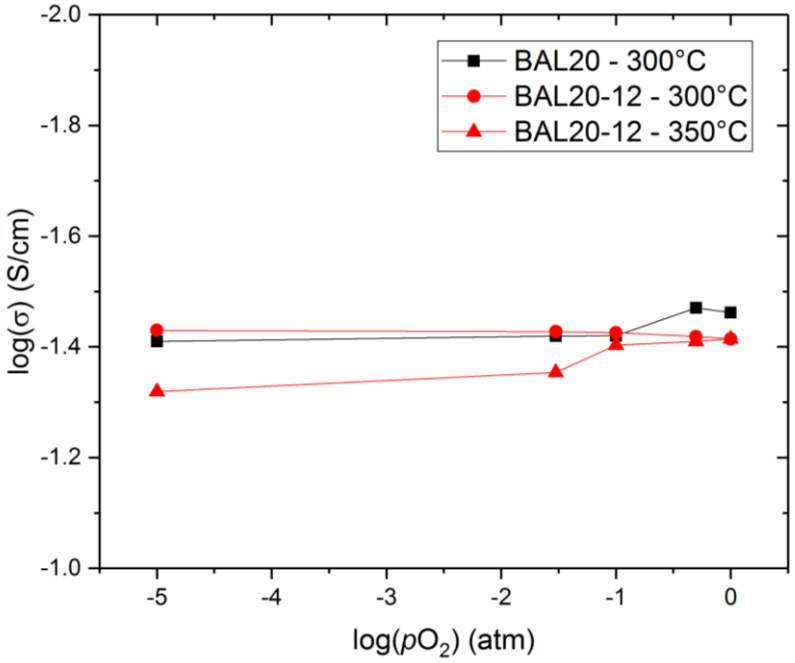

Figure 5.12: Total conductivity as a function of pO_2 for BAL20 (in black) and BAL20-12 (in red, and at two different temperatures). The plot point at $\log(pO_2) = 0$ is the same for the graphs for 300°C and 350°C for BAL20-12.

While the graph for BAL20-12 (at 350°C) shows decreased conductivity with increasing pO_2, the result is the opposite for BAL20-12 at 300°C and BAL20. Furthermore, the changes in conductivity are too small to be considered as an effect. From this, it is clear that the conductivity has no dependency on the pO_2. It can thus be concluded that electronic defects, electrons and electron holes, are minority defects in the material.

5.3.4 pH_2O Dependency

The dependency of pH_2O for the conductivity in the samples was also investigated. The results of these measurements are plotted below.

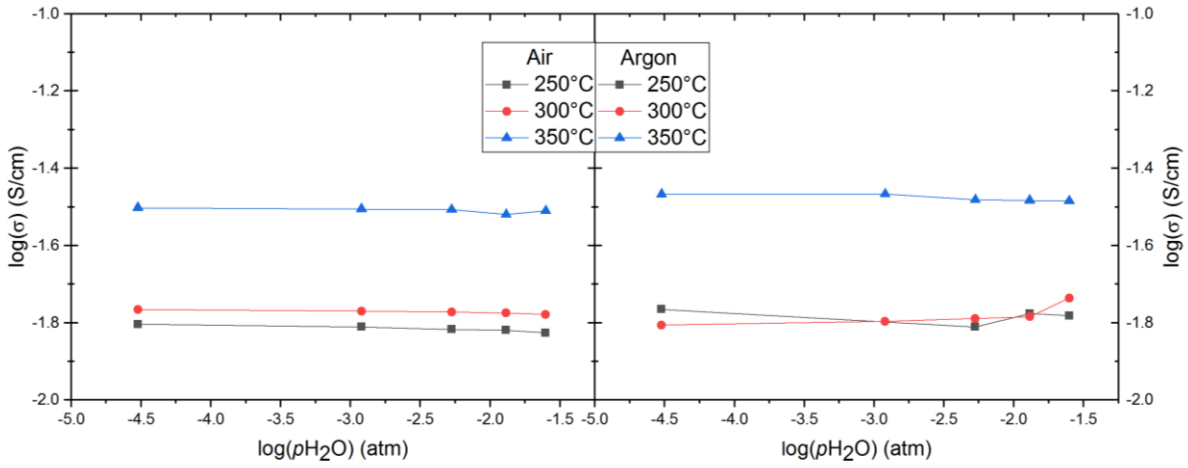

Figure 5.13: pH_2O dependency for BAL20-12, in air (left) and Ar-atmosphere (right).

There is a slight trend in the conductivity of BAL20-12 in air. At all temperatures, the conductivity decreases at increasing pH_2O. However, the difference in conductivity is very small. The variation in conductivity between maximum and minimum pH_2O level is between 1.5% and 5.0%.

This dependency is not apparent in Ar-atmosphere. At 300°C, the conductivity increases with increasing pH_2O, while the opposite trend is seen at 350°C. The dependency is more unclear at 250°C, as the plot point at $\log(pH_2O) = -2.9$ atm is unavailable. Additionally, the other points are seemingly unrelated by each other.

Furthermore, the changes in conductivity are very small, with a change in less than one tenth of an order of magnitude over a change in pH_2O of 4 orders of magnitude. All these factors

considered, it is determined that there is no pH_2O dependency for the conductivity. Which means that H^+ and $OH_O^\bullet$ are minority defects, and thus do not contribute to the total conductivity in a significant way.

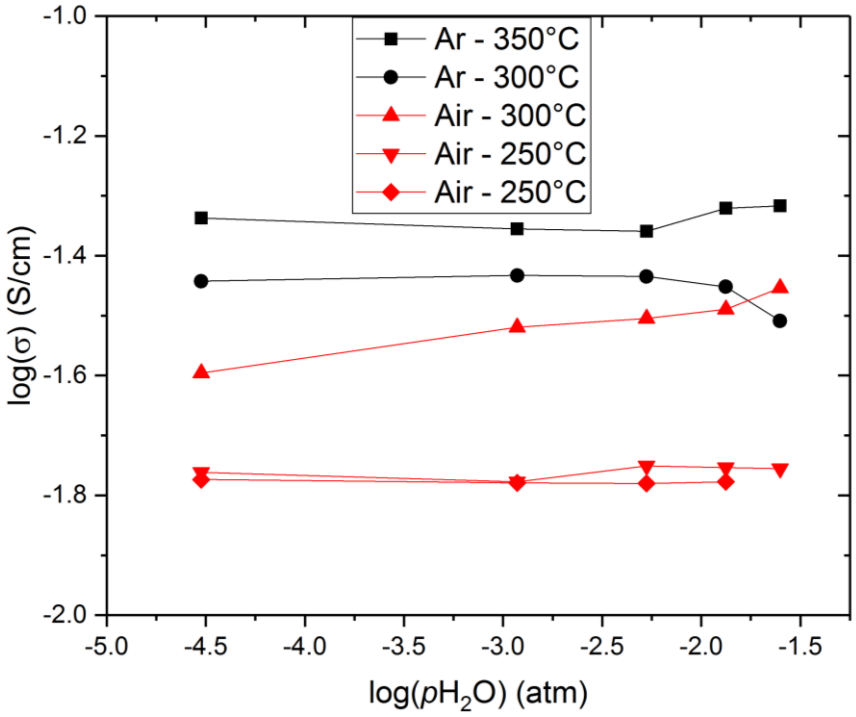

Figure 5.14: pH_2O dependency for BAL20. Measurements in Ar-atmosphere are black, while those conducted in air are red. The conductivity was measured at 250°C in air twice.

No pH_2O dependency is seen for BAL20 either. In Ar-atmosphere, the two measurements give an opposite trend of each other. In air, the conductivity is relatively unaffected by the pH_2O level at 250°C, showing the same relative differences as the plots for BAL20-12. Meanwhile it increases with the pH_2O at 300°C. This, however, is the opposite of the trend seen in BAL20-12.

6 Discussion

6.1 Comparison of Synthesis Routes

As the parameters of the synthesis changed throughout the work, so did the samples. From the first samples that were mixed and grinded by hand to the last ones, who were ball-milled for hours, there were notable differences in attributes.

6.1.1 Phase Composition

An important aspect of the sample preparation was to form the cubic phase of LLZO. LLZU, which is the undoped sample, is a purely tetragonal phase. As the Al-doping is used to stabilize the c-LLZO, it can be expected for the LLZU to not have any cubic phase present.

The addition of Al to the mix during synthesis does seem to promote the formation of c-LLZO. For LAL20 and LAL25, the peak at ~31° appears to merge into one (figure 5.1). However, both samples contain both phases. Even though LAL25 consists of the higher level of Al-doping, it is still the least pure sample. This is expected to be a result of the problems regarding the temperature during the sintering of the pellet. The other samples was sintered at $T \geq 1150°C$, indicating that this could be a minimum temperature needed to achieve c-LLZO during synthesis. Temperature and sintering times are not the only important parameters for the resulting pellet. A homogenous green pellet would be important, to ensure the Al is spread evenly throughout the sample, promoting the cubic phase. By having a heterogeneous green pellet, unwanted phases could form as a result of uneven concentration distribution of the precursors. This would be challenging to achieve by grinding the powders by hand in a mortar as it would require long periods of grinding while the powders are also exposed to ambient air. This could lead to the formation of $La(OH)_3$ from the highly hygroscopic La_2O_3, which in turn could cause alterations to the stoichiometry. This problem is avoided due to the use of isopropanol during grinding and drying in a heating cabinet after milling.

Looking at the impurities seen in the patterns of LAL20 and LAL25, Li_2ZrO_3 is an expected secondary phases, seen in literature. The Al_4Zr_5 phase is more surprising and could be the result of poor mixing of the powders through grinding by hand. It is worth mentioning that

$La_2Zr_2O_7$, which has been reported by several other works, was not seen in any of the samples.

From figure 5.1 we can see that the samples BAL20-12 and BAL20 consist purely of the cubic phase, without any secondary phases. This could mean that a homogenous dispersion of Al is one of the most important parameters to achieve during synthesis of the samples, especially when comparing these diffractograms to those of the other three samples, which were grinded by hand. The split peak indicating tetragonal phase can be seen in both LAL20 and LAL25, despite both being doped by Al. The long ball milling of the aforementioned samples also leads to much smaller grain size than what is achievable by hand. The smaller grain size, in combination with better dispersion of the powders is probably the cause of the higher amount of cubic phase seen in these samples, and the lack of secondary phases.

6.1.2 Microstructure

Just like the phase composition of the samples changed, so did the morphology and other physical characteristics. The most notable difference between the samples grinded by hand and the two ball milled is the difference in density. Not only is this difference seen when weighing and measuring them, like the relative density values in table 5.1 indicates, but it is also visible by looking at them in an SEM. The three samples investigated have a clear difference in surface morphology, with LLZU being the more porous of them. Both the pores and the microstructures on the surface are larger compared to BAL20 and BAL20-12.

Despite the synthesis routes for BAL20 and BAL20-12 being almost the same, there are differences to the samples. While they look similar, with surfaces appearing dense, with little pores, there are some microstructural variations. Looking at figure 6.1 a) and b), BAL20-12 appears denser on one side compared to the other. In _6.1 a), the boundaries between the structures are clearly visible, while they are not in 6.1 b). Which of these was up and down during sintering is not known.

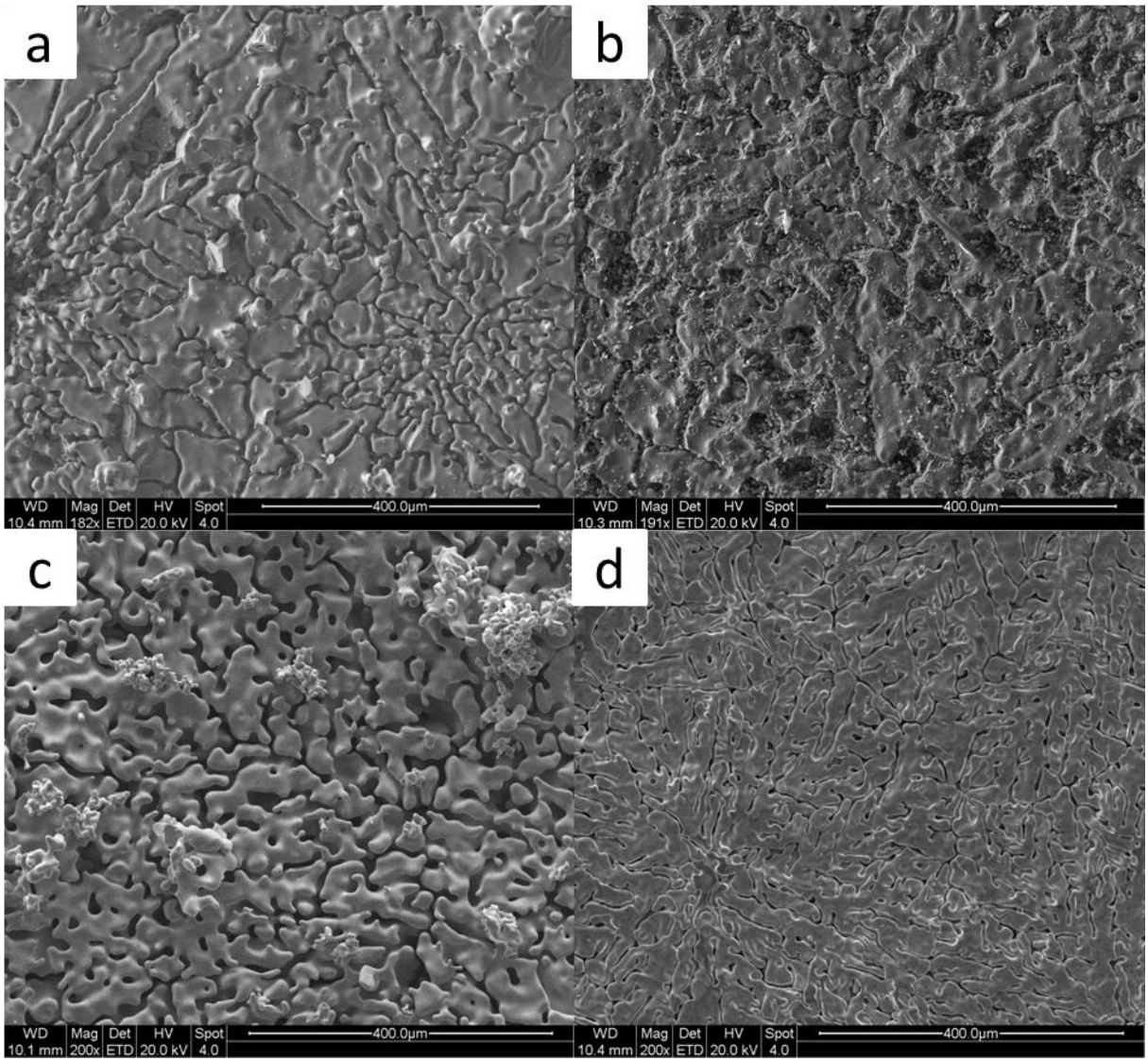

Figure 6.1: SEM pictures of both sides of BAL20-12, a) and b), the surface of LLZU c) and BAL20 d) all with a scale bar of 400 µm. The ball-milled and samples are visibly denser and less porous than LLZU, which is grinded by hand and undoped.

Comparing figure 5.5 and 5.6 we see the difference of the internal structures of LAL20 and LLZU. In LLZU, the structure consists of grains of various sizes. The internal structure of LAL20 on the other hand is more similar to its surface, with no clear grains.

A problem of porous samples is that they have a tendency to break easily as they are rather brittle. All samples did at some point break, except BAL20-12. This happened either through simple actions such as preparing them for XRD, like LAL20, or through accidents, like BAL20, which was dropped when being mounted to the ProboStat cell. It should be mentioned that BAL20 took surprisingly little damage from falling, considering the brittleness of the previous samples. This proves how much the solidity of the samples improved by ball-milling of the powders.

6.1.3 Activation Energy

From literature, the reported activation energy for the c-LLZO is 0.3-0.4 eV, like seen in table 3.1. This is a good fit for BAL20 with an activation energy at lower temperatures of ~0.4 eV. BAL20-12 on the other hand shows a notably lower activation energy of ~0.27 eV.

The change of the slope at ~250°C for BAL20 could be a transition from bulk to a combined grain boundary and bulk conductivity. This would explain the high activation energy at high temperature during the cooldown. Meanwhile, the activation energy of the high temperature area during the second heating is lower than the low temperature area. An explanation for this effect could be that there is less grain boundary resistance contribution, due to higher conductivity in this area. This, again, could be caused by different effects, such as further sintering during the heating or growth of the grains.

Another possible explanation to why the activation energy at high temperature is so low during the second heating is that the slope is influenced by the transition area, between 175°C and 250°C, and is therefore lower than it should be. By increasing the temperature, it would have been possible to investigate this further, and higher activation energy could maybe have been seen. So, for BAL20-12, the temperature was thus increased to 350°C, to look for the same transition. However, the transition in the Arrhenius plot for BAL20 (figure 5.11 a) and b)) is not observed for BAL20-12 (5.11 c) and d)). Seeing that the slope decreases at the highest temperatures during the 2nd heating, a transition could also be present in this sample, though less influential than it is in BAL20.

An increase in activation energy at lower temperatures is the opposite of what is expected, but is observed for all measurements except for the cooldown of BAL20. This could be due to microstructural changes, or (for BAL20) less contribution from the grain boundary as the sample is reheated.

Comparing the activation energy of the two samples, BAL20-12 shows significantly lower activation energy than BAL20 (low temperature). As they have similar densities and XRD patterns no obvious explanations lies here. Looking at figure 5.3 and 6.1, the surfaces are the almost same and from the impedance plots, the grain boundary contribution is probably negligible. From table 5.2, it is clear that the pre-exponential factor is considerably lower for BAL20-12 than for BAL20. From this, the conclusion can be drawn that there are fewer

active sites in BAL20-12 than BAL20. Both these things can correlate with the higher sintering temperature of BAL20-12. Li is a volatile element at higher temperatures, and from equation 14, it is seen that it evaporates during sintering. A lower concentration of Li-ions in the structure could explain the lower value of the pre-exponential factor. At the same time it would create more Li-vacancies, making it easier for Li-ions to diffuse through the structure, as will be explained in section 6.2.

6.2 Defects of LLZO

By using the alternative Kröger-Vink notation suggested by Norby, the defective chemistry of LLZO can be better described. Using the normal Kröger-Vink notation does not give a proper picture of how the intrinsic defects cause the conductivity of the material. An LLZO unit cell consists of 8 formula units (of $Li_7La_3Zr_2O_{12}$). As there are both tetrahedral and octahedral Li-sites, there are a total 72 possible sites for Li in a unit cell (8 formula units). To simplify it, the 56 Li-atoms randomly distributes over these sites, thus occupying 7/9 of the available sites. Using Norbys notation $\frac{7}{9}\mathrm{Li}$ is introduced as the perfect site. A Li in this site will now be considered a defect, as a $\frac{7}{9}$Li-ion does not exist. Li on this $\frac{7}{9}\mathrm{Li}$ site thus get an effective positive charge: $\mathrm{Li}^{\frac{2}{9}\bullet}_{\frac{7}{9}\mathrm{Li}}$. As for vacancies, they still have an effective charge, but now with a different value: $\mathrm{v}^{\frac{7}{9}/}_{\frac{7}{9}\mathrm{Li}}$. From this, it is clear that there are 2 Li-vacancies per formula unit, giving an electroneutrality of $\frac{2}{9}\left[\mathrm{Li}^{\frac{2}{9}\bullet}_{\frac{7}{9}\mathrm{Li}}\right] = \frac{7}{9}\left[\mathrm{v}^{\frac{7}{9}/}_{\frac{7}{9}\mathrm{Li}}\right]$, meaning $\mathrm{Li}^{\frac{2}{9}\bullet}_{\frac{7}{9}\mathrm{Li}}$ work as the charge compensating defect for vacancies. Considering this, the suggestion from Kubicek et al, about oxygen vacancies being the charge compensating defect, is wrong. Also meaning that the concentration of oxygen vacancies in the structure is lower than what is suggested in figure 3.4.

Using the Norby notation, an Al^{3+} substituting Li form $\mathrm{Al}^{\frac{20}{9}\bullet}_{\frac{7}{9}\mathrm{Li}}$ defects. Using the Norby notation on equation14, the following defect reaction happens:

$$6\mathrm{Li}_{\frac{7}{9}\mathrm{Li}}^{\frac{2}{9}\bullet} + \mathrm{Al}_2\mathrm{O}_3(\mathrm{s}) = 2\,\mathrm{Al}_{\frac{7}{9}\mathrm{Li}}^{\frac{20}{9}\bullet} + 4\mathrm{v}_{\frac{7}{9}\mathrm{Li}}^{\frac{7}{9}/} + 3\mathrm{Li}_2\mathrm{O}(\mathrm{g}) \quad (32)$$

Giving an electroneutrality condition of $\frac{2}{9}\left[\mathrm{Li}_{\frac{7}{9}\mathrm{Li}}^{\frac{2}{9}\bullet}\right] + \frac{20}{9}\left[\mathrm{Al}_{\frac{7}{9}\mathrm{Li}}^{\frac{20}{9}\bullet}\right] = \frac{7}{9}\left[\mathrm{v}_{\frac{7}{9}\mathrm{Li}}^{\frac{7}{9}/}\right]$. The introduction of Al^{3+} increases the concentration of vacant Li-sites. Where there were 2 vacancies per formula unit in the undoped material, a concentration of 1 Al^{3+} per formula unit gives 4 Li-vacancies. The number of Li^+ is thus reduced from 7 to 4 per formula unit. An increased concentration of Li-vacancies causes an increase in the conductivity of the Li-ions in the structure.

Looking at equation 6, the conductivity of Li^+-ions depends on the concentration and the mobility of the ion. Through doping by Al^{3+} the concentration of Li^+ decreases, but as the concentration of Li-vacancies increases, the mobility of the ions increases, causing an overall increase in the ionic conductivity.

6.2.1 *p*O_2 and *p*H_2O Dependencies

From the *p*O_2 measurements, the conductivity showed no dependency towards *p*O_2. This, however, is not in accordance with literature. Kubicek et al. reported a *p*O_2 dependency [54] and the Brouwer diagram made by Zhan et al. (figure 3.4) suggests the same. [55] As oxygen vacancies are a minority defect, it would not be expected to make any notable impact on the total conductivity. Furthermore, as there is no dependency on *p*O_2 conductivity, electrons and electron holes have a *p*O_2 dependency of -¼ and ¼, respectively, as expected from section 2.2.2. This is a small dependency, and considering they are minority defects in the material, they do not alter the *p*O_2 dependency of the conductivity of the material.

The conductivity of LLZO was also found to be independent from *p*H_2O. From this, the conclusion can be drawn that H^+ is a minority defect, with a *p*H_2O dependency of ½. Considering that the concentration of oxygen vacancies is low, the same goes for the concentration of $\mathrm{OH}_{\mathrm{O}}^{\bullet}$.

While the problems of moisture at RT are known, there was more uncertainty regarding the effects of water in the atmosphere on the samples, at 300°C. A worst case scenario would be that the moisture would damage or even destroy the sample, even at elevated temperatures. It does, however, seem like that there were no major negative impacts to the sample.

Measurements of the impedance done both before and after the pH_2O dependency were fairly similar, suggesting the sample was left undamaged by the added water vapor in the atmosphere. As discussed in section 3.6, there are reports of a Li^+/H^+-ion-exchange between H_2O and LLZO. This, however, is mainly in liquid water. It is also seen in ambient air, but considering the temperatures in which the pH_2O dependency measurements were conducted, this exchange is not expected to happen.

6.3 Impedance

The calculation of different values using the impedance plots depend on the fitting of the equivalent circuit. However, fitting these plots has been challenging. At 100°C, a small semicircle is seen in BAL20 at high frequencies (figure 5.9). This is probably the contribution from the bulk, but it is difficult to fit and thus get reliable values from, due to the inductance. This contribution is most clear for the two plots at 100°C, however, it is also seen in the other plots from BAL20 <100°C, as well as the plot at 30°C for BAL20-12. Fitting this small part also became impossible due to the irregular shape of the plots at very high frequencies. The inductance is probably also the reason to why no semicircles are seen at the highest frequencies at higher temperatures, and why none of the plots start at 0 Ω. While the capacitance values are uncertain, this confirms the bulk contribution. This also shows that the grain boundary contribution is negligible, at least at low temperatures.

6.4 Corrosion of Pt-wire

After measurement series 2 was completed, the cell was opened. The Pt-wire used was then found to have corroded (see figure 6.2). The corroded parts were removed, and there was run a XRD on a piece of this. The corrosion was found to be Li_2PtO_3.

The Li_2PtO_3 is a semiconducting material that forms at ca. 600°C. This is probably the reason for the high resistance measured at low temperatures for measurement series 2. In hindsight, an Au-wire would have been a better choice, as it is more inert.

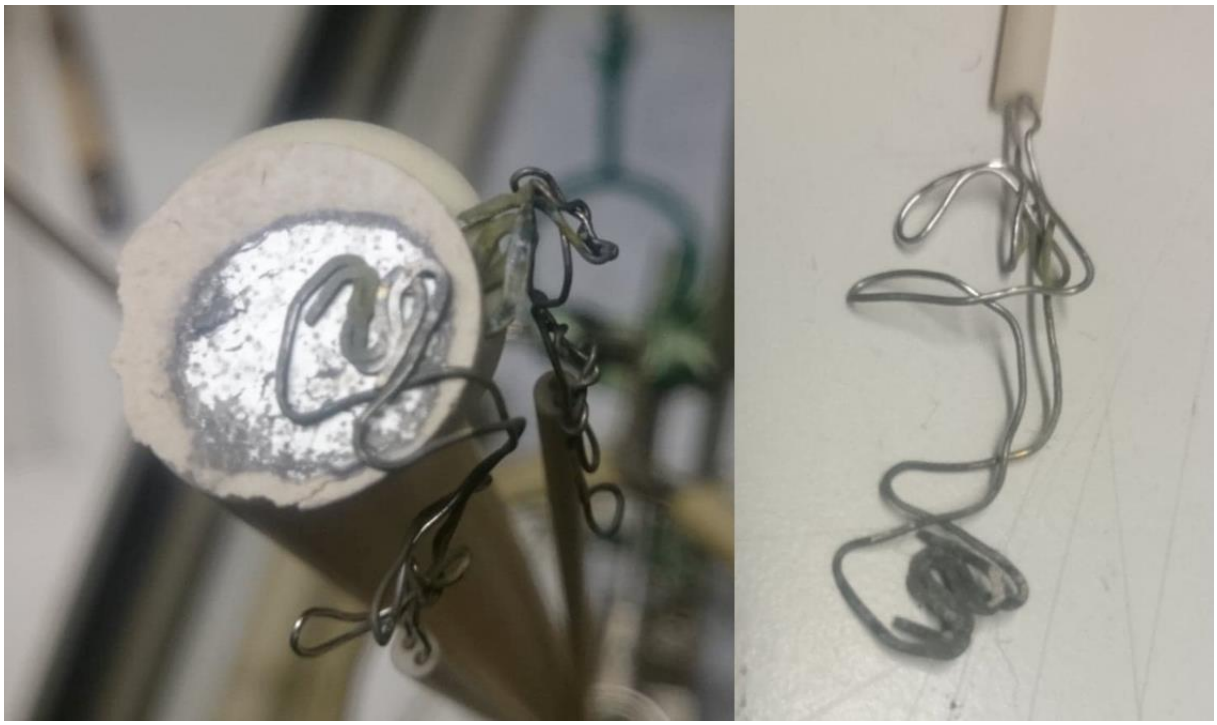

Figure 6.2: The corroded Pt-wire from measurement series 2. In the picture to the right the darker area at the folded part of the wire is the corrosion. This area is Li_2PtO_3, which is a poor conductor.

This problem was avoided in later measurements by measuring at lower temperatures. As measurement series 2 brought the sample up to 500°C, which is not too far from the reported formation temperature of 600°C for Li_2PtO_3, the temperature for the rest of the measurements never exceeded 350°C. After this, the wire was properly polished and its conductivity checked by a multimeter. As it conducted as expected, the wire was used for the rest of the experiments.

6.5 Further Work

In this work, pO_2 and pH_2O dependencies have been investigated, but only at Al-doped samples. In the future it would be interesting to see if different dopants will be affected differently by this. Kubicek reported a difference in how the oxygen vacancy concentration changed as the concentration of different dopants was altered. This could mean that which dopant and their concentrations could also alter the dependencies. Additionally, while the pO_2 and pH_2O dependencies have been investigated in this work, the pH_2 dependency was not. Seeing how the material reacts to a reducing atmosphere would be of interest, though this could damage the sample over time.

As this material is a promising candidate for substituting today's liquid electrolyte in LIBs, future research should focus on doing experiments in the target temperature range of a normal battery. Furthermore, making coin cell batteries and testing their conductivity would be a logical investigation. As LLZO is known to be stable towards Li-metal, making batteries using this as an electrode, in an SSB, would be a major step in the right direction, should it work.

The use of other characterization techniques to the investigation of LLZO would be interesting. Solid-state NMR would allow for investigations of how the Li atoms and Al dopants are binding to the other elements in the structure. XPS (X-ray photoelectron spectroscopy) is another technique that would allow for examining how the Li-ions are behaving, by looking at its surroundings inside the structure.

Should this material become an electrolyte in future SSB, CO_2 capture is an aspect of the synthesis that must be taken into account. Looking at the formula for the reaction it is clear that a lot of CO_2 is produced:

$$7Li_2CO_3(s) + 3La_2O_3(s) + 4ZrO_2(s) \rightarrow 2Li_7La_3Zr_2O_{12}(s) + 7CO_2(g) \qquad (33)$$

An industrial scale production of this material should therefore have a good plan for how to capture the CO_2 released during production of this material.

7 Conclusion

In this work, the material LLZO, which is one of the most promising candidates for a solid-state electrolyte, has been studied. The main interest has been to investigate the conductivity of the material, both as a function of temperatures and atmospheric composition. Furthermore, the effect of the synthesis route on the structure and conductivity of the samples was studied.

Conductivity

The investigations of the conductivity of the different samples were hindered by the fault in the spectrometer. Because of this there are conductivity measurements only from 2 out of 5 samples. These two samples had almost the same synthesis route, making it hard to draw any conclusion of the effects of the synthesis routes on the conductivity.

For the two samples measured, the total conductivity was shown to be 9×10^{-5} S/cm and 4.4×10^{-4} S/cm for BAL20 and BAL20-12 (measured at 30°C), respectively. These are relatively promising values, compared to literature (3×10^{-4} S/cm), though uncertain.

Effect of synthesis routes

The implementation of Al-doping to the synthesis made influenced the phase composition of the samples, promoting the cubic phase of LLZO. The amount of Al-doping, however, seems less important as LAL20 and LAL25 have rather similar diffraction patterns.

What made the biggest difference in phase composition was shown to be the preparation method of the precursors and how they are mixed. The ball milled samples, BAL20 and BAL20-12, are close to pure c-LLZO, without secondary phases, such as Li_2ZrO_3, which is seen in both LAL20 and LAL25.

The effect of the sintering temperature was not an objective, but some information about its effect was still achieved. BAL20-12 was sintered at 1200°C, unlike the other samples, including BAL20, sintered at 1150°C. The XRD patterns of BAL20 and BAL20-12 show no notable difference between the two samples, indicating 1150°C is a sufficiently high temperature for the formation of c-LLZO. However, BAL20-12 does seem to have a higher density and conductivity than BAL20, suggesting that a higher sintering temperature leads to denser samples, which in turn increases the conductivity. LAL25, on the other hand, showed a

bigger deviation from the expected pattern. There is probably a correlation between the amount of secondary phases and the sintering temperature of this sample, as the highest temperature achieved was 1090°C. This is a clear indication that T<1100°C might not be sufficient to form c-LLZO.

Gas Dependencies

Only sporadic and ambiguous dependencies were seen, suggesting that the conductivity of LLZO is not significantly affected by the pO_2 and pH_2O of the atmosphere in the cell, at least for temperatures above 250°C.

Effect of Water

While there are many reports of moisture damaging samples of LLZO, investigations of BAL20 show that the sample is rather unaffected by the water from the pH_2O dependency measurements. No visible changes have appeared, and the XRD patterns are basically identical to what they looked like before the measurements were performed, with no secondary phases found.

Investigations of BAL20-12 by SEM conclude that there are no visible structural changes to the internal microstructure of the sample.

List of References

[1] U.S. Energy Information Administration, "International Energy Outlook 2018", in "Analysis & Projections," July 2018.

[2] BP (2017). "Statistical Review of World Energy" [Online]. Available: https://www.bp.com/en/global/corporate/energy-economics/statistical-review-of-world-energy.html [Accessed: 08.05.19]

[3] Earth System Research Laboratory. (2018). "Trends in Atmospheric Carbon Dioxide" [Online]. Available: https://www.esrl.noaa.gov/gmd/ccgg/trends/data.html [Accessed: 08.05.19]

[4] D. K. Samferdselsdepartement, "Nasjonal transportplan 2018-2019", Det Kongelige Samferdselsdepertement, Oslo, April 5th 2017.

[5] "The Future is Electric" [Online]. Available: https://group.volvocars.com/company/innovation/electrificatioN [Accessed: 31.01.19]

[6] A. Skredderberget. (2018). "The first ever zero emission, autonomous ship" [Online]. Available: https://www.yara.com/knowledge-grows/game-changer-for-the-environment/ [Accessed: 15.05.19]

[7] J. Hodges. (2018). "Electric buses are hurting the oil industry" [Online]. Available: https://www.bloomberg.com/news/articles/2018-04-23/electric-buses-are-hurting-the-oil-industry [Accessed: 25.04.18]

[8] "Elfly i Norge" [Online]. Available: https://avinor.no/konsern/miljo-og-samfunn/elfly/elektriske-fly [Accessed: 31.01.19]

[9] G. E. Blomgren, "The Development and Future of Lithium Ion Batteries," *Journal of The Electrochemical Society*, vol. 164, no. 1, pp. A5019-A5025, 2016.

[10] Battery University. (2016). "Specific energy and specific power of rechargeable batteries". Available: https://batteryuniversity.com/learn/article/global_battery_markets [Accessed: 25.05.19]

[11] A. Brennhagen, "Synthesis and electrochemical characterization of thin film iron phosphates as cathode material for Li-ion batteries.," Master, Chemistry, University of Oslo, Oslo, 2019.

[12] A. Callaway. (2018). "Powering Down Corruption" [Online Report]. Available: https://enoughproject.org/wp-content/uploads/PoweringDownCorruption_Enough_Oct2018-web.pdf

[13] F. Zheng, M. Kotobuki, S. Song, M. O. Lai, and L. Lu, "Review on solid electrolytes for all-solid-state lithium-ion batteries," *Journal of Power Sources*, vol. 389, pp. 198-213, 2018.

[14] R. Wenige, M. Niemann, U. Heider, M. Jungnitz and V. Hilarius, "Liquid Electrolyte Systems for Advanced Lithium Batteries", Chemical Engineering Research Information Center, 1998.

[15] N. Kamaya *et al.*, "A lithium superionic conductor," *Nat Mater*, vol. 10, no. 9, pp. 682-6, Jul 31 2011.

[16] Y. Sun *et al.*, "Oxygen substitution effects in $Li_{10}GeP_2S_{12}$ solid electrolyte," *Journal of Power Sources*, vol. 324, pp. 798-803, 2016.

[17] C. Bernuy-Lopez, W. Manalastas, J. M. Lopez del Amo, A. Aguadero, F. Aguesse, and J. A. Kilner, "Atmosphere Controlled Processing of Ga-Substituted Garnets for High Li-Ion Conductivity Ceramics," *Chemistry of Materials*, vol. 26, no. 12, pp. 3610-3617, 2014.

[18] R. Murugan, V. Thangadurai, and W. Weppner, "Fast lithium ion conduction in garnet-type $Li_7La_3Zr_2O_{12}$," *Angew Chem Int Ed Engl*, vol. 46, no. 41, pp. 7778-81, 2007.
[19] J. Smyth. "Garnet″ [Online]. Available: http://ruby.colorado.edu/~smyth/min/garnet.html [Accessed: 15.05.19]
[20] T. Norby, "Defects and Transport in Crystalline Materials", 2018.
[21] F. A. Kröger and H. J. Vink, "Relations between the Concentrations of Imperfections in Crystalline Solids", in *Solid State Physics*, vol. 3, F. Seitz and D. Turnbull, Eds.: Academic Press, 1956, pp. 307-435.
[22] T. Norby, "A Kröger-Vink Compatible Notation for Defects in Inherently Defective Sublattices", *Journal of the Korean Ceramic Society*, vol. 47, no. 1, pp. 19-25, 2010.
[23] C. A. Geiger *et al.*, "Crystal chemistry and stability of "$Li_7La_3Zr_2O_{12}$" garnet: a fast lithium-ion conductor", *Inorg Chem*, vol. 50, no. 3, pp. 1089-97, Feb 7 2011.
[24] T. Norby, "Electrical Measurements", 2016.
[25] B. Tribollet and M. E. Orazem, "Electrochemical Impedance Spectroscopy″. New Jersey: John Wiley & Sons, Inc, 2008.
[26] M. N. Kakaei, J. Neshati, and A. R. Rezaierod, "On the Extraction of the Effective Capacitance from Constant Phase Element Parameters," *Protection of Metals and Physical Chemistry of Surfaces*, vol. 54, no. 3, pp. 548-556, 2018.
[27] J. Awaka, A. Takashima, K. Kataoka, N. Kijima, Y. Idemoto, and J. Akimoto, "Crystal Structure of Fast Lithium-ion-conducting Cubic $Li_7La_3Zr_2O_{12}$," *Chemistry Letters*, vol. 40, no. 1, pp. 60-62, 2011.
[28] G. Larraz, A. Orera, and M. L. Sanjuán, "Cubic phases of garnet-type $Li_7La_3Zr_2O_{12}$: the role of hydration," *Journal of Materials Chemistry A*, vol. 1, no. 37, 2013.
[29] J. L. Allen, J. Wolfenstine, E. Rangasamy, and J. Sakamoto, "Effect of substitution (Ta, Al, Ga) on the conductivity of $Li_7La_3Zr_2O_{12}$," *Journal of Power Sources*, vol. 206, pp. 315-319, 2012.
[30] E. Rangasamy, J. Wolfenstine, and J. Sakamoto, "The role of Al and Li concentration on the formation of cubic garnet solid electrolyte of nominal composition $Li_7La_3Zr_2O_{12}$," *Solid State Ionics*, vol. 206, pp. 28-32, 2012.
[31] P. Knauth, "Inorganic solid Li ion conductors: An overview," *Solid State Ionics*, vol. 180, no. 14-16, pp. 911-916, 2009.
[32] V. Thangadurai, S. Narayanan, and D. Pinzaru, "Garnet-type solid-state fast Li ion conductors for Li batteries: critical review," *Chem Soc Rev*, vol. 43, no. 13, pp. 4714-27, Jul 7 2014.
[33] J. F. Wu, W. K. Pang, V. K. Peterson, L. Wei, and X. Guo, "Garnet-Type Fast Li-Ion Conductors with High Ionic Conductivities for All-Solid-State Batteries," *ACS Appl Mater Interfaces*, vol. 9, no. 14, pp. 12461-12468, Apr 12 2017.
[34] Y. Jin and P. J. McGinn, "Al-doped $Li_7La_3Zr_2O_{12}$ synthesized by a polymerized complex method," *Journal of Power Sources*, vol. 196, no. 20, pp. 8683-8687, 2011.
[35] M. Kotobuki, K. Kanamura, Y. Sato, and T. Yoshida, "Fabrication of all-solid-state lithium battery with lithium metal anode using Al2O3-added $Li_7La_3Zr_2O_{12}$ solid electrolyte," *Journal of Power Sources*, vol. 196, no. 18, pp. 7750-7754, 2011.
[36] S. Afyon, F. Krumeich, and J. L. M. Rupp, "A shortcut to garnet-type fast Li-ion conductors for all-solid state batteries," *Journal of Materials Chemistry A*, vol. 3, no. 36, pp. 18636-18648, 2015.
[37] I. Kokal, M. Somer, P. H. L. Notten, and H. T. Hintzen, "Sol–gel synthesis and lithium ion conductivity of $Li_7La_3Zr_2O_{12}$ with garnet-related type structure," *Solid State Ionics*, vol. 185, no. 1, pp. 42-46, 2011.

[38] Y. Shimonishi *et al.*, "Synthesis of garnet-type $Li_{7-x}La_3Zr_2O_{12-1/2x}$ and its stability in aqueous solutions," *Solid State Ionics,* vol. 183, no. 1, pp. 48-53, 2011.
[39] N. Bernstein, M. D. Johannes, and K. Hoang, "Origin of the structural phase transition in $Li_7La_3Zr_2O_{12}$," *Phys Rev Lett,* vol. 109, no. 20, p. 205702, Nov 16 2012.
[40] J. Wolfenstine, J. Ratchford, E. Rangasamy, J. Sakamoto, and J. L. Allen, "Synthesis and high Li-ion conductivity of Ga-stabilized cubic $Li_7La_3Zr_2O_{12}$," *Materials Chemistry and Physics,* vol. 134, no. 2-3, pp. 571-575, 2012.
[41] T. Thompson *et al.*, "Tetragonal vs. cubic phase stability in Al – free Ta doped $Li_7La_3Zr_2O_{12}$ (LLZO)," *J. Mater. Chem. A,* vol. 2, no. 33, pp. 13431-13436, 2014.
[42] Y. Li *et al.*, "Ionic distribution and conductivity in lithium garnet $Li_7La_3Zr_2O_{12}$," *Journal of Power Sources,* vol. 209, pp. 278-281, 2012.
[43] D. O. Shin *et al.*, "Synergistic multi-doping effects on the $Li_7La_3Zr_2O_{12}$ solid electrolyte for fast lithium ion conduction," *Sci Rep,* vol. 5, p. 18053, Dec 15 2015.
[44] Y. Li *et al.*, "W-Doped $Li_7La_3Zr_2O_{12}$ Ceramic Electrolytes for Solid State Li-ion Batteries," *Electrochimica Acta,* vol. 180, pp. 37-42, 2015.
[45] L. Dhivya, N. Janani, B. Palanivel, and R. Murugan, "Li+ transport properties of W substituted $Li_7La_3Zr_2O_{12}$ cubic lithium garnets," *AIP Advances,* vol. 3, no. 8, p. 082115, 2013.
[46] R. Murugan, S. Ramakumar, and N. Janani, "High conductive yttrium doped $Li_7La_3Zr_2O_{12}$ cubic lithium garnet," *Electrochemistry Communications,* vol. 13, no. 12, pp. 1373-1375, 2011.
[47] E. Hanc, W. Zając, and J. Molenda, "Synthesis procedure and effect of Nd, Ca and Nb doping on structure and electrical conductivity of $Li_7La_3Zr_2O_{12}$ garnets," *Solid State Ionics,* vol. 262, pp. 617-621, 2014.
[48] Y. Zhu *et al.*, "Dopant-Dependent Stability of Garnet Solid Electrolyte Interfaces with Lithium Metal," *Advanced Energy Materials,* vol. 9, no. 12, p. 1803440, 2019.
[49] R. Wagner *et al.*, "Fast Li-Ion-Conducting Garnet-Related Li_{7-3x} Fe $_x$ $La_3Zr_2O_{12}$ with Uncommon *I43d* Structure," *Chem Mater,* vol. 28, no. 16, pp. 5943-5951, Aug 23 2016.
[50] S. Kumazaki *et al.*, "High lithium ion conductive $Li_7La_3Zr_2O_{12}$ by inclusion of both Al and Si," *Electrochemistry Communications,* vol. 13, no. 5, pp. 509-512, 2011.
[51] S. V. Pershina, E. A. Il'ina, and O. G. Reznitskikh, "Phase Composition, Density, and Ionic Conductivity of the $Li_7La_3Zr_2O_{12}$-Based Composites with LiPO3 Glass Addition," *Inorg Chem,* vol. 56, no. 16, pp. 9880-9891, Aug 21 2017.
[52] P. Zhao *et al.*, "A novel method for preparation of high dense tetragonal $Li_7La_3Zr_2O_{12}$," *Journal of Power Sources,* vol. 344, pp. 56-61, 2017.
[53] J. Wolfenstine, E. Rangasamy, J. L. Allen, and J. Sakamoto, "High conductivity of dense tetragonal $Li_7La_3Zr_2O_{12}$," *Journal of Power Sources,* vol. 208, pp. 193-196, 2012.
[54] M. Kubicek *et al.*, "Oxygen Vacancies in Fast Lithium-Ion Conducting Garnets," *Chemistry of Materials,* vol. 29, no. 17, pp. 7189-7196, 2017.
[55] X. Zhan, S. Lai, M. P. Gobet, S. G. Greenbaum, and M. Shirpour, "Defect chemistry and electrical properties of garnet-type $Li_7La_3Zr_2O_{12}$," *Phys Chem Chem Phys,* vol. 20, no. 3, pp. 1447-1459, Jan 17 2018.
[56] Y. Jin and P. J. McGinn, "$Li_7La_3Zr_2O_{12}$ electrolyte stability in air and fabrication of a Li/Li7La3Zr2O12/Cu0.1V2O5 solid-state battery," *Journal of Power Sources,* vol. 239, pp. 326-331, 2013.
[57] C. Galven, J.-L. Fourquet, M.-P. Crosnier-Lopez, and F. o. Le Berre, "Instability of the Lithium Garnet $Li_7La_3Sn_2O_{12}$: Li^+/H^+Exchange and Structural Study," *Chemistry of Materials,* vol. 23, no. 7, pp. 1892-1900, 2011.

[58] C. Galven, J. Dittmer, E. Suard, F. Le Berre, and M.-P. Crosnier-Lopez, "Instability of Lithium Garnets against Moisture. Structural Characterization and Dynamics of $Li_{7-x}H_xLa_3Sn_2O_{12}$ and $Li_{5-x}H_xLa_3Nb_2O_{12}$," *Chemistry of Materials,* vol. 24, no. 17, pp. 3335-3345, 2012.
[59] M. Nyman, T. M. Alam, S. K. McIntyre, G. C. Bleier, and D. Ingersoll, "Alternative Approach to Increasing Li Mobility in Li-La-Nb/Ta Garnet Electrolytes," *Chemistry of Materials,* vol. 22, no. 19, pp. 5401-5410, 2010.
[60] T. Norby, "ProGasMix Software User Manual", 2011.
[61] NORECS, "ProboStat™ Manual", NORECS AS, 2018.

Appendix

A.1 Impedance Plots

In section 5.3.1 the data and fittings from two plots are presented (figure 5.8 and 5.9). In the figures below, full impedance spectra are presented, to show how they vary with temperature and instrumentation.

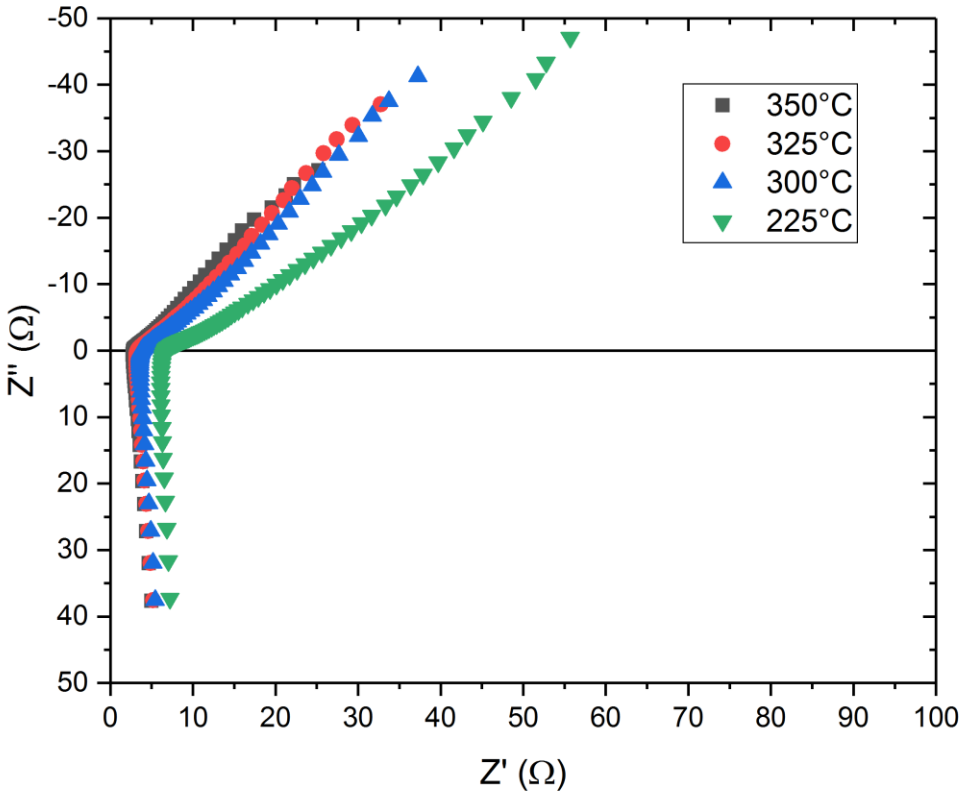

Figure A.1: Impedance spectra from high temperature measurements of BAL20-12, performed at Lars' setup. Spectra show inductance. Electrode “tail” is shorter than what is seen in the spectra for BAL 20. This is probably due to the high AC voltage applied (500 mV).

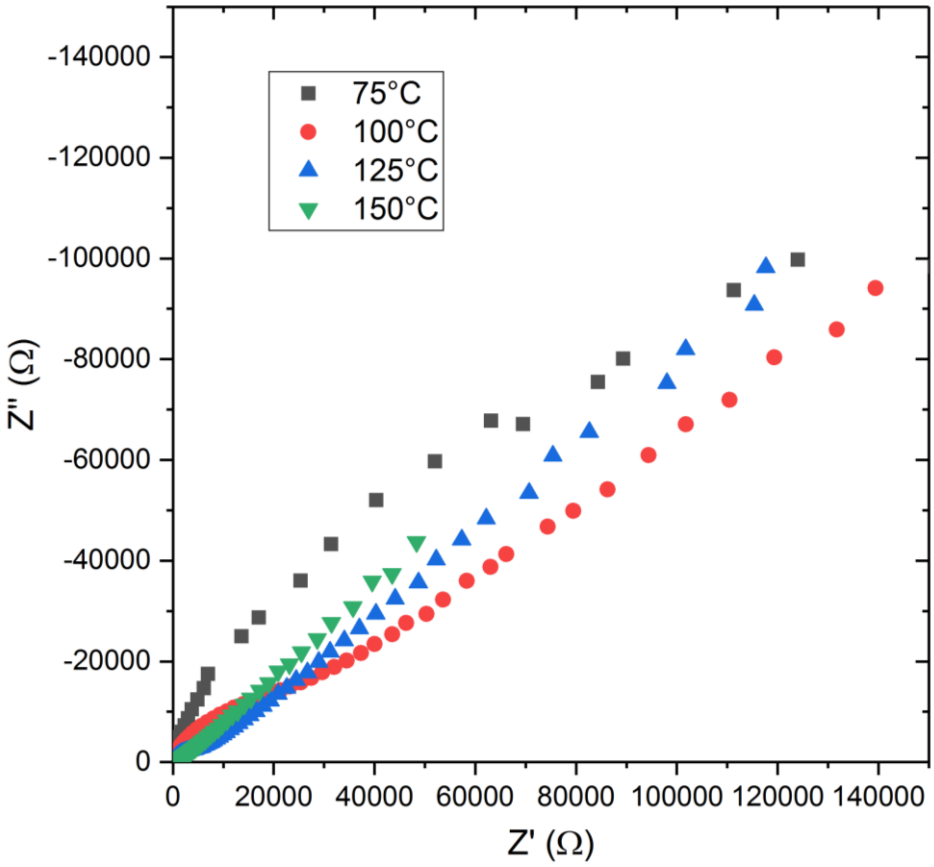

Figure A.2: Impedance spectra from low temperature measurements of BAL20, which was conducted at the "usual setup".

A.2 Electrode/Pellet Interface

To investigate how the Ag electrode affects the samples, LAL20 was broken in half after impedance spectroscopy was finished. By using SEM the interface between the electrode and the sample was investigated. Furthermore, EDS was used to look for changes in the phase composition in the same area.

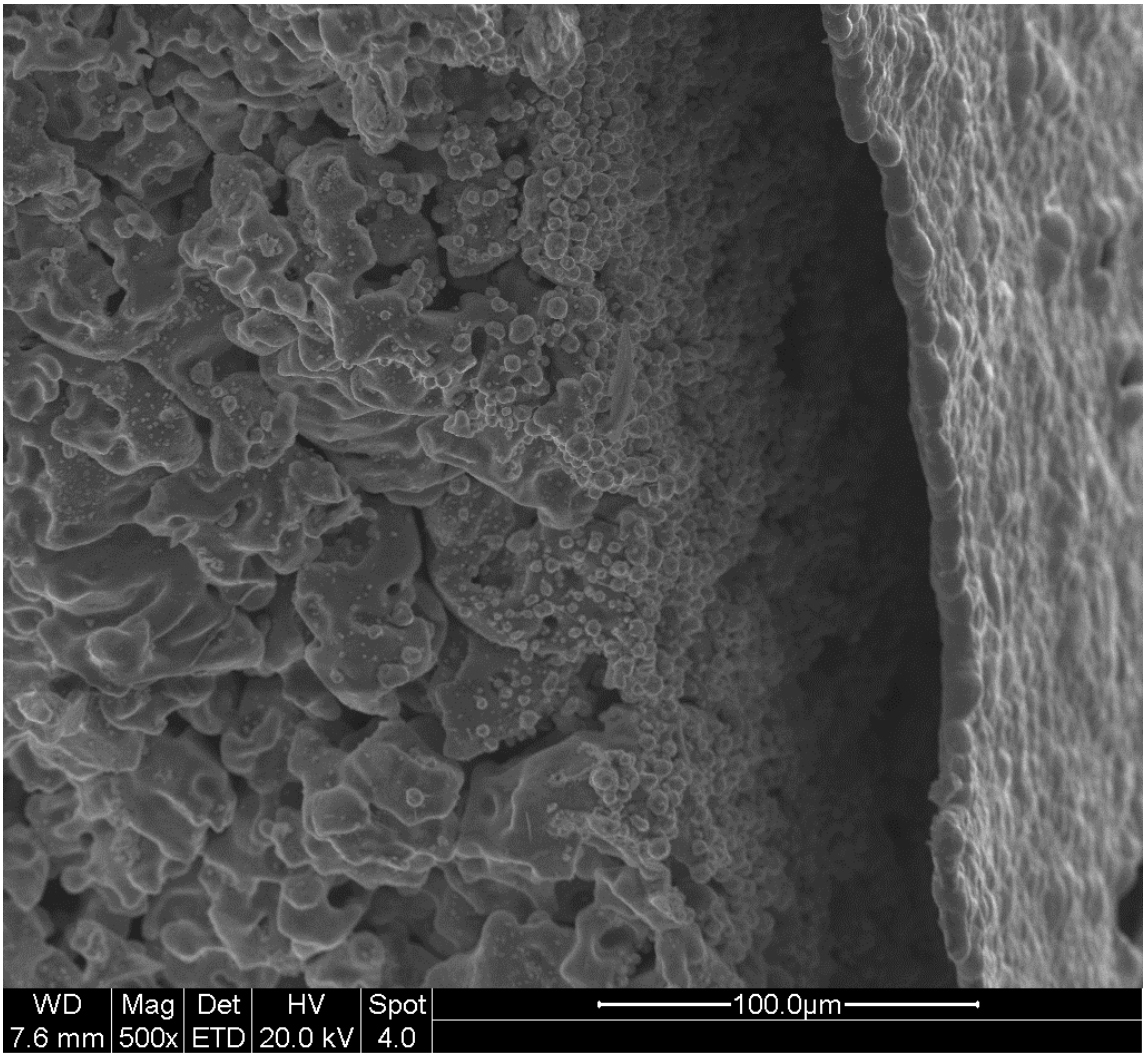

Figure A.3: SEM picture of the interface between the pellet (left) and the Ag-electrode (right). Ag particles can be seen in the interface.

Particles of Ag were seen in the interface between the pellet surface and the electrode. Using EDS, no new phases were seen. The Ag remains on the surface, and does not diffuse into the sample.

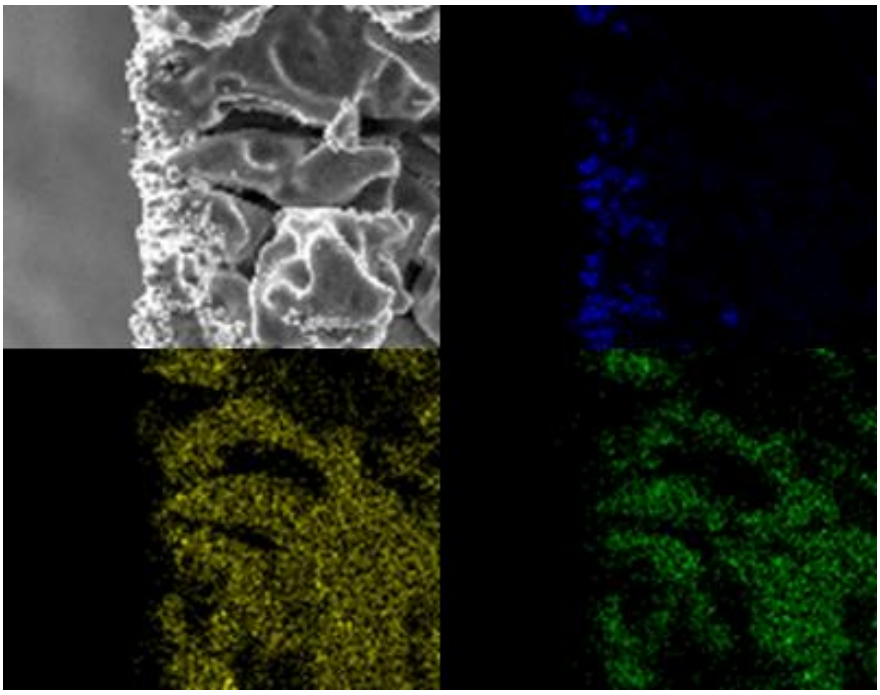

Figure A.4: EDS of the electrode-pellet interface. Top left is the SEM picture, of the area investigated. Blue is Ag, yellow is La and green is Zr. The low resolution is due to hardware problems with the PC used for the EDS.

A.3 EDS of BAL20

While studying BAL20 in the SEM after the impedance spectroscopy, odd features were seen on the surface. There were grains apparently containing two phases as well as crystalline formation between grains. To investigate what these features were, the sample was studied using EDS.

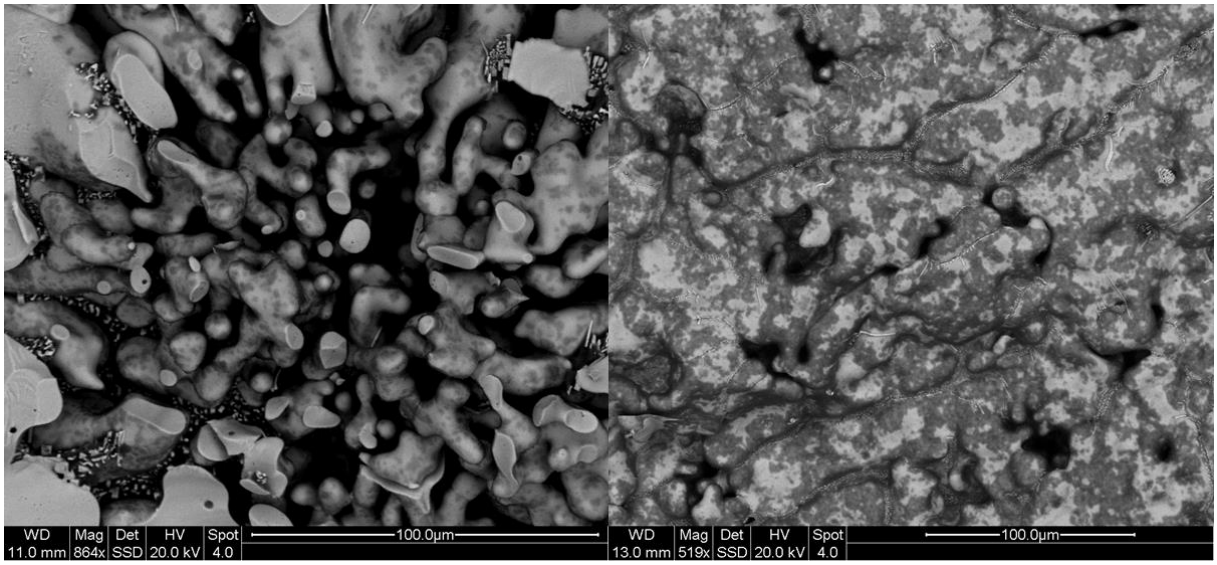

Figure A.5: SEM pictures of areas of interest, showing phase separation.

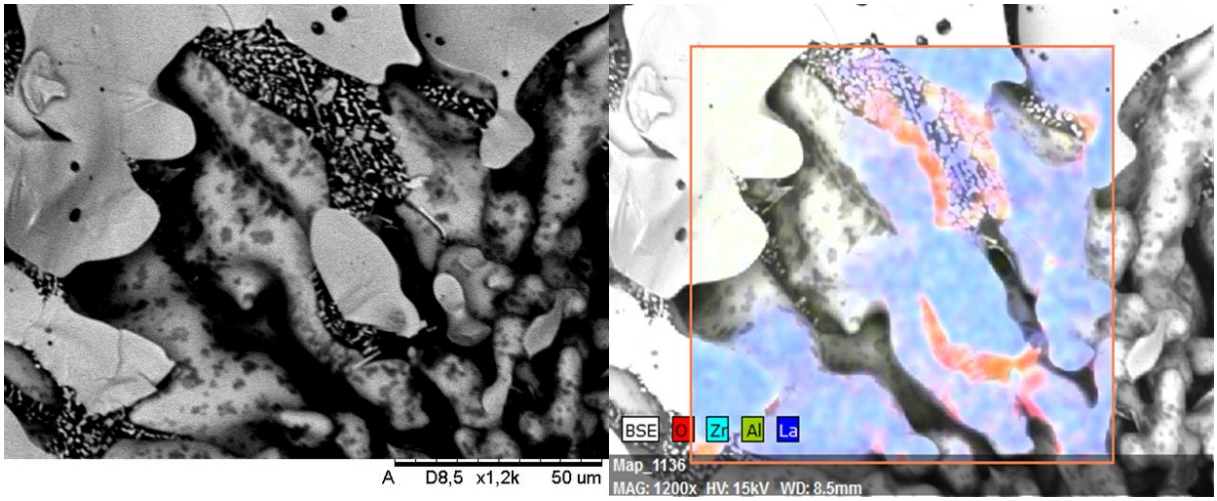

Figure A.6: Left: SEM picture of the area to which the EDS was conducted. Right: Elemental mapping of the picture to the left. Some areas are not scanned, as the reflecting x-rays are scattered away from the detector, or they are screened from the x-rays in the first place.

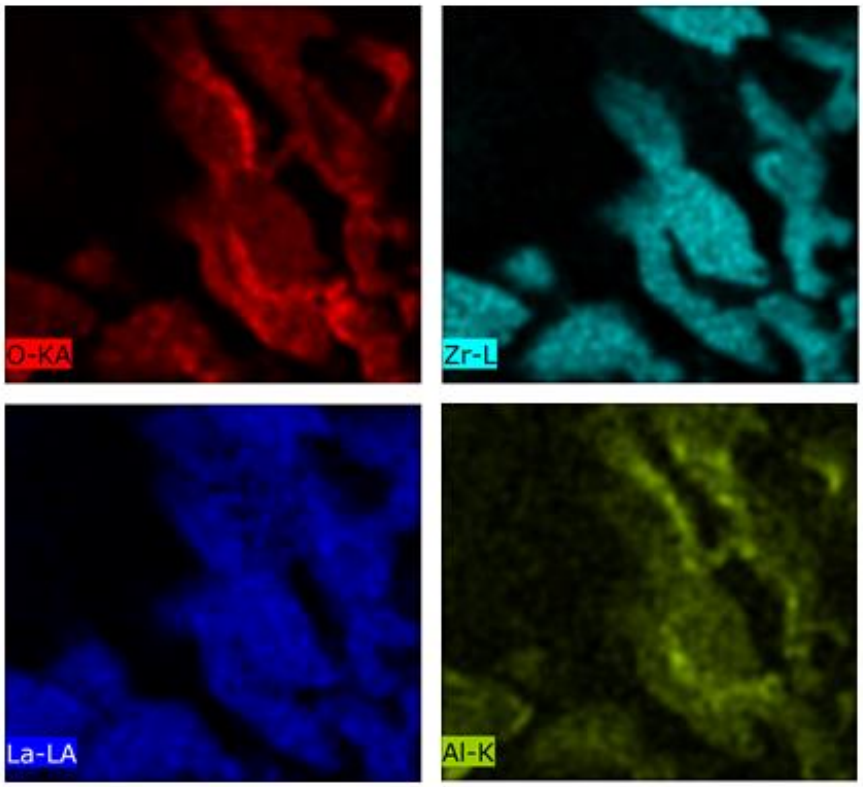

Figure A.7: Separate elemental maps of for the elements.

From figures A.6, A.7 and A.9, it is seen that the crystalline structures are low in Zr, and have a higher amount of Al and O than surrounding areas. La, on the other hand, is evenly distributed. This leads to the conclusion that these probably are Al_2O_3 crystals.

In an attempt to determine more decisively what these areas are, spot scans were performed. One was done on one of the particles showing two phases (figure A.8) and one on the crystal-like structures (figure A.9). What is seen is that the level of Al and Zr varies between the two areas. The EDS shows low amounts of Al in the "spotted" grain, and normal amounts of Zr. Meanwhile, the crystal-like area show high amounts of Al, but low amounts of Zr, strengthening the evidence that these crystals are Al_2O_3. The level of La and O present are about the same in both places. In the spectrum in figure A.9, there is an unlabeled peak. The program suggests that this peak is Si. This, however, seems unlikely, as there are no known sources of Si used during sintering. Furthermore, the EDS is taken of areas from the inside of the pellet, which reduces the chance of it being contamination after sintering. It is also odd that Si is not seen in the spectra in figure A.8, if it is a contamination of the surface of the piece, after it broke off.

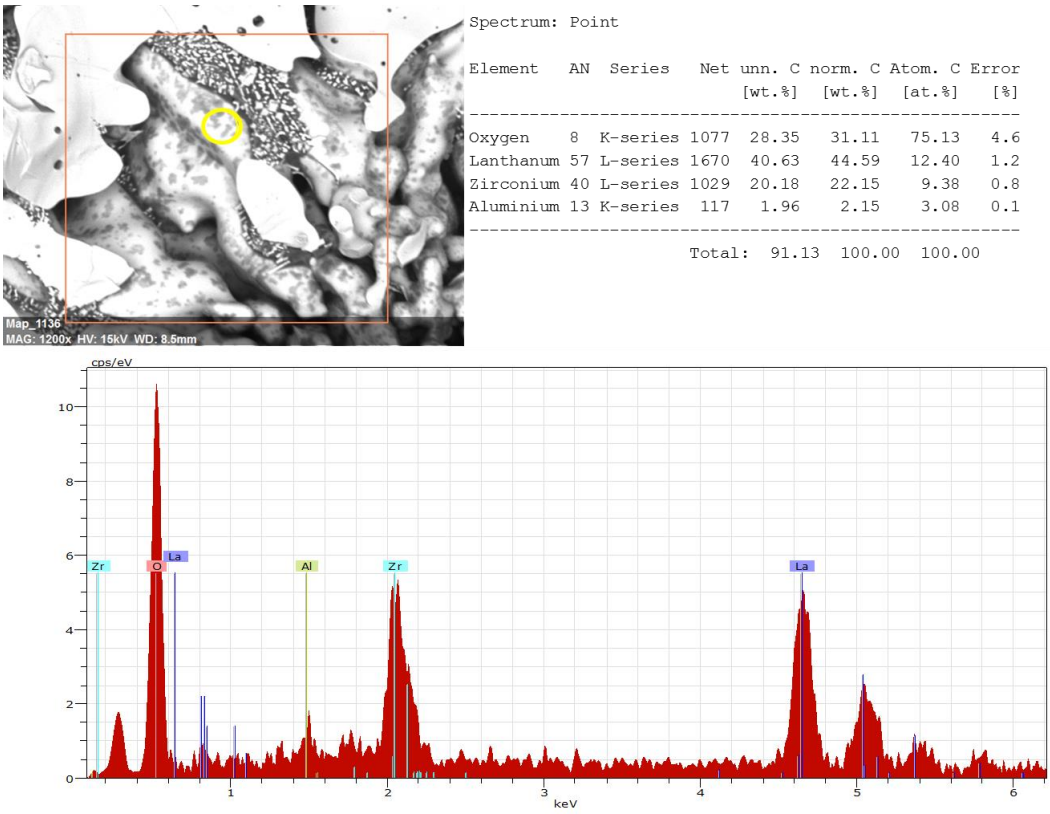

Figure A.8: Spot scan of the grain with separate phases, showing low amounts of Al.

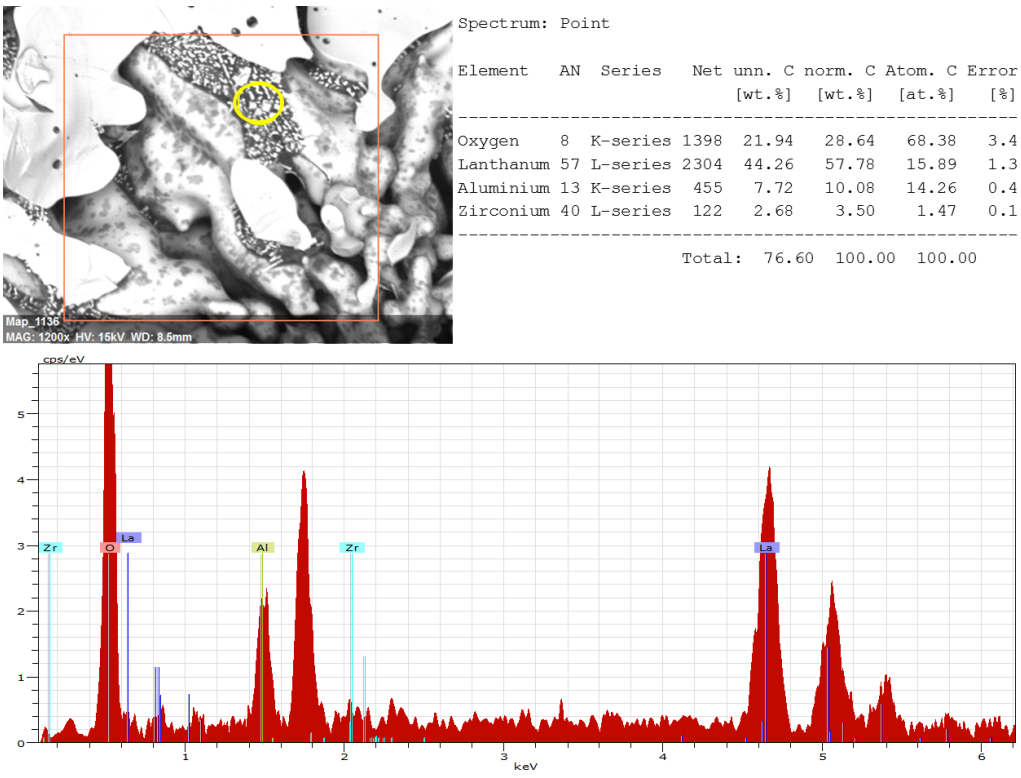

Figure A.9: Spot scan of the crystal-like structures showing high amounts of Al and almost no Zr. There is an unlabeled spike, which is suggested by the program to be Si.

A.4 Early Samples

Other than the samples discussed in this thesis, many more were made while figuring out what the best synthesis route was. The last sample not used for this thesis was studied in the SEM. Below are some of the pictures from that sample.

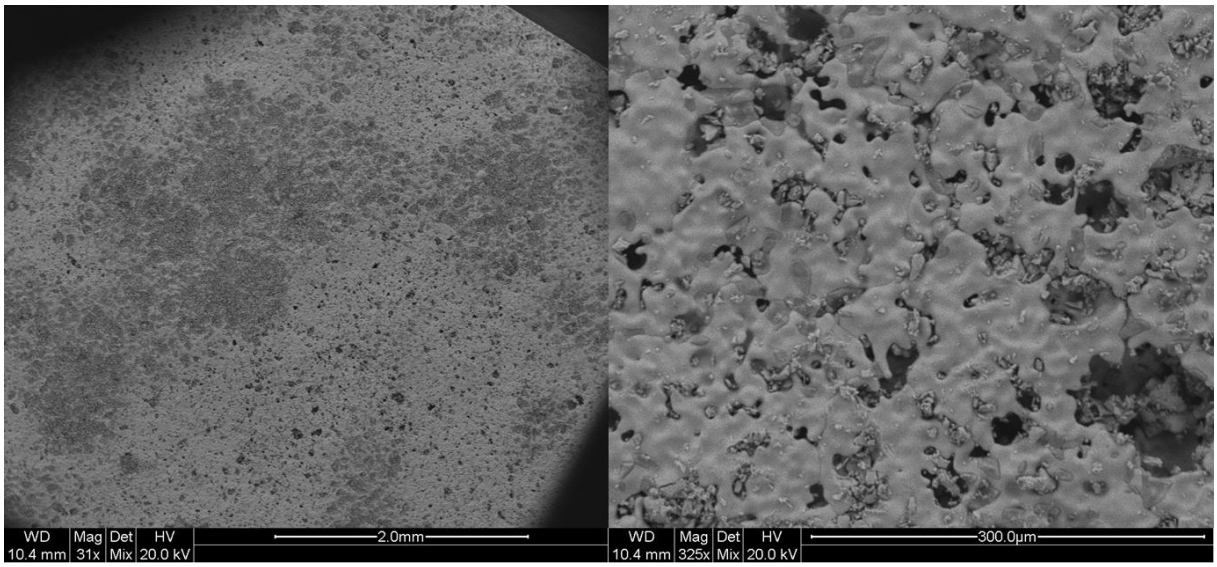

Figure A.10: SEM pictures of an early sample, this is the prototype of LLZU. Left: An overview of the sample surface. Right: A higher magnification picture of the same surface.

The sample is porous, and fairly similar to LLZU, which is expected, as this sample is undoped and grinded by hand as well.